Title

Improving our Understanding of High-latitude Tropospheric Marine Aerosols using NASA Earth-Observing satellites and the Biogeochemical Southern Ocean State Estimate (B-SOSE)

Author

Dasarathy, Srishti

Publication Date

2023

Peer reviewed|Thesis/dissertation

UNIVERSITY OF CALIFORNIA SAN DIEGO

Improving our Understanding of High-latitude Tropospheric Marine Aerosols using NASA Earth-Observing satellites and the Biogeochemical Southern Ocean State Estimate (B-SOSE)

A Dissertation submitted in partial satisfaction of the requirements
for the degree Doctor of Philosophy

in

Oceanography

by

Srishti Dasarathy

Committee in charge:

Jeff Bowman, Chair
Jennifer Burney
Matthew Mazloff
Lynn Russell
Dariusz Stramski

2023

The Dissertation of Srishti Dasarathy is approved, and it is acceptable in quality and form for publication on microfilm and electronically.

University of California San Diego

2023

TABLE OF CONTENTS

LIST OF FIGURES

LIST OF ABBREVIATIONS

AMSR-E	Advanced microwave scanning radiometer for the Earth observing system
MAOD	Marine aerosol optical depth
AOD	Aerosol optical depth
AOD_C	Coarse-mode aerosol optical depth
AOD_f	Fine-mode aerosol optical depth
AOD_T	Total column aerosol optical depth
B-SOSE	Biogeochemical Southern Ocean State Estimate
CAD	Cloud-aerosol discrimination
CALIOP	Cloud-aerosol lidar with orthogonal polarization
CALIPSO	Cloud-aerosol lidar and infrared pathfinder satellite observation
CCN	Cloud condensation nuclei
Chl-*a*	Chlorophyll-*a* concentration
DMS	Dimethylsulfide
DMSP	Dimethylsulfoniopropionate
LSPB	Large surface phytoplankton biomass
MAD	Mean absolute deviations
MLD	Mixed layer depth
MSA	Methane sulfonic acid
MODIS	Moderate resolution imaging spectroradiometer
NaN	Not a number
NASA	National Aeronautics and Space Administration
NCP	Net Community Production

NSS	Non-sea salt
NPP	Net Primary Production
POC	Particulate organic carbon
QC	Quality control
SeaWiFS	Sea-viewing wide field-of-view sensor
SIE	Sea Ice Extent
SOSE	Southern Ocean State Estimate
SSA	Sea spray aerosol
SSPB	Small surface phytoplankton biomass
SST	Sea surface temperature
WAP	Western Antarctic peninsula

ACKNOWLEDGEMENTS

I would like to acknowledge and give my warmest thanks and deepest appreciation to my advisor and the chair of my committee, Jeff S. Bowman. His support, guidance, and feedback throughout my PhD have been invaluable and have carried me through all struggles and doubts. Thank you for not only helping me develop my acumen as a scientist, but also supporting my career growth in avenues both within and beyond academia.

I would also like to express my deepest gratitude to my committee members Lynn Russell and Matthew Mazloff, who generously volunteered their time, knowledge, and expertise towards the completion of Chapters 2 and 3 of this dissertation. I would also like to give my deepest thanks to my committee members Dariusz Stramski and Jennifer Burney, who generously provided their time and guidance towards the completion of this work.

I am also grateful to my graduate student friends and to the Bowman lab for their continued emotional and moral support. The completion of my graduate school journey and this dissertation wouldn't have been possible without their generous help through homework review sessions, coding help, practice presentation runs, and writing feedback. Thank you!

Finally, I would like to give special thanks to my family, especially my parents, brother, and my fiancé. I couldn't have done this without you.

Chapter 1, in full, is a reprint of the material as it appears in Journal of Geophysical Research: Atmospheres 2021. Dasarathy, Srishti; Kar, Jayanta; Tackett, Jason; Rodier, Sharon D.; Lu, Xiaomei; Vaughan, Mark; Toth, Travis D.; Trepte, Charles; Bowman, Jeff S.; 2021. DOI: 10.1029/2021JD034737. The dissertation author was the primary investigator and author of this paper. Graduate student peers Kelley McBride and Dr. Kara Voss provided insight in accessing and processing of the CALIOP dataset. Dr. Nicole Couto likewise aided

in mapping techniques. This work was supported by NSF-OPP 1846837, NSF-OPP 1821911, and a Simons Foundation Early Career Marine Microbial Investigator Award. This work was further supported by the NASA Internship Program at the Langley Research Center.

Chapter 2, in full, is a reprint of the material as it appears in Geophysical Research Letters 2023. Dasarathy, Srishti; Russell, Lynn M.; Rodier, Sharon D.; Bowman, Jeff S.; 2023. DOI: 10.1029/2022GL099723. The dissertation author was the primary investigator and author. This research was supported by NSF-OPP 1846837 and the Climate and Environmental Sciences Division of the U.S. Department of Energy under Contract DE-SC0021045. Initial phases of this work were supported by the NASA Internship Program at the Langley Research Center.

VITA

2016	Bachelor of Science, The University of North Carolina at Chapel Hill
2019	Summer Intern, NASA Langley Research Center
2021-2022	Scripps Industry Relations & Innovation Fellow, Scripps Institution of Oceanography
2022-2023	AI Machine Learning Engineer Intern, Lockheed Martin
2023	Doctor of Philosophy, University of California San Diego

PUBLICATIONS

Dasarathy, S,* Kar, J, Tackett, J, Rodier, SD, Lu, X, Vaughan, M, Toth, TD, Trepte, C, Bowman, JS, 2021. *Multi-year seasonal trends in sea ice, chlorophyll concentration, and marine aerosol optical depth in the Bellingshausen Sea*. *JGR Atmospheres.* DOI: 10.1029/2021JD034737

Dasarathy, S,* Russell, LM, Rodier, SD, Bowman, JS, 2023. *Wind-driven and Seasonal Effects on marine aerosol production in the Bellingshausen Sea, Antarctica.* Geophysical Research Letters. DOI: 10.1029/2022GL099723

Dowell, F, Cardman, Z, Dasarathy, S,* et al., 2016. *Microbial communities in methane- and short chain alkane-rich hydrothermal sediments of Guaymas Basin*. *Frontiers in Microbiology.* DOI: 10.3389/fmicb.2016.00017

FIELD OF STUDY

Biological Oceanography

ABSTRACT OF THE DISSERTATION

Improving our Understanding of High-latitude Tropospheric Marine Aerosols using NASA Earth-Observing satellites and the Biogeochemical Southern Ocean State Estimate (B-SOSE)

by

Srishti Dasarathy

Doctor of Philosophy in Oceanography

University of California San Diego, 2023

Jeff S. Bowman, Chair

Tropospheric marine aerosol presence in the western Antarctic is coupled to physical and biological processes. These aerosols may be biogenic, formed from the activity of primary producers, and can be associated with seasonal dynamics of sea ice melt and phytoplankton blooms. These aerosols may also influence local environments of polar regions by absorbing and scattering solar radiation and by initiating cloud formation. To study

tropospheric marine aerosol in the remote marine Bellingshausen Sea environment, we used a specialized instrument onboard the NASA Cloud-Aerosol Lidar and Infrared Pathfinder Satellite Observation (CALIPSO) capable of detecting the presence of aerosols at altitudes close to the sea surface. We termed this measurement marine aerosol optical depth (MAOD). To further support these observations, we also examined coarse-mode aerosol optical depth (AOD_C), often used as a proxy for sea spray aerosol (SSA). We used MAOD and AOD_C to examine trends in marine tropospheric aerosol and undertook a multi-year remote sensing analysis in the Bellingshausen Sea from 2006-2018.

Across open ocean to coastal regions, daily fluctuations in nighttime and daytime winds, respectively, drove increasing MAOD and AOD_C. MAOD depicted strong correlations with wind speed across the open ocean and weak correlations in coastal regions, suggesting that daily fluxes in wind speed drive the production of SSA. In the open ocean, we further observed that warmer SST enhanced AOD_C and the associated production of SSA, supporting prior studies. We also observed seasonal increases in MAOD alongside a seasonal increase in chl-*a* and the melt of sea ice; these patterns suggest that biological activity of primary producers likely contributed towards magnitudes of marine tropospheric aerosol. This work is also the first to distinguish a late winter to early spring temporal MAOD signal, likely tied to an aerosol source from either venting of biogenic aerosol from breaks in sea ice or to the production of SSA resulting from pulses in wind speed. Our work extends upon previous findings of marine aerosol in polar environments and more fully characterizes interactions during polar winter.

INTRODUCTION

Aerosols are broadly defined as a suspension of fine solid particles or liquid droplets in air or another gas. These particles can have a high degree of variability in their chemical composition and concentrations throughout the atmosphere thereby diversely impacting Earth's climate. Most notably, the Intergovernmental Panel on Climate Change (IPCC) has emphasized the lack of knowledge of the aerosol impact on the Earth radiation budget and on the climate (Olivier Boucher et al., 2013). For example, aerosols impact climate through direct scattering and absorption of incoming solar radiation, trapping outgoing long-wave radiation, through alteration of cloud optical properties, and affecting the formation of clouds and precipitation (Olivier Boucher et al., 2013). Aerosol sources are either natural or anthropogenic, and the vast majority, 90%, have natural origins (Weng, 2011). Of this proportion, prior studies have estimated that 30 to 75% of natural aerosols are marine, with the oceans producing 1000 to 10000 Tg of marine aerosol per year (Blanchard & Woodcock, 1980; de Leeuw et al., 2011).

The presence and production of marine aerosol is influenced by a vast array of physical and biological dynamics of the surface ocean, from sea surface wind speed, sea surface temperature, phytoplankton blooms, organic matter enrichment, melt of sea ice, among other things (Dasarathy et al., 2021; Dasarathy, Russell, Rodier, & Bowman, 2023; Dror, Lehahn, Altaratz, & Koren, 2018; Gabric et al., 2005, 2018). Most importantly, marine aerosol production and their dependency on these many parameters is not yet uniformly determined (Dasarathy et al., 2021). Particularly in polar environments, studying marine aerosol dynamics has proven notoriously difficult due to adverse weather, difficulty in transporting instruments and sensors, and lack of sunlight in wintertime for passive sensor retrievals of aerosol optical properties

(Dasarathy et al., 2021). Nevertheless, examining these aerosols is critically important to better understand the aerosol impact on climate particularly in fragile polar environments.

My overarching goal throughout my dissertation was to better quantify the sources and production of marine aerosol in remote polar environments removed from anthropogenic sources. As such I undertook a multi-year analysis of the Bellingshausen Sea examining a vast amount of physical and biogeochemical data through use of satellite remote sensing and modeled ocean state estimates. In this remote polar environment, the formation and presence of marine tropospheric aerosol is coupled with physical, chemical, and biological processes. Present in both the Antarctic and Arctic, these sea ice habitats are among the largest ecosystems on our planet (Arrigo, 2014). They are subject to a number of physical processes due to the inherent temporality of high-latitude environments, from the seasonal dynamics of variable light availability, increases and decreases in sea ice extent and thickness, fluctuations in nutrient availability, and fluctuations in the timing and magnitude of primary production and chlorophyll-*a* (chl-*a*) concentration (Ardyna et al., 2014; Tremblay & Gagnon, 2009). This inherent seasonality of high latitude environments has distinct impacts on the formation and presence of marine tropospheric aerosol.

As the Bellingshausen Sea is distant from most continental sources of anthropogenic pollution and mineral dust, variability in the sources of marine aerosol in this polar sea ice environment is largely driven by the ocean itself. The Bellingshausen Sea is thus a relatively pristine environment to study the impact of primary and secondary sources as drivers of marine tropospheric aerosol. Primary sources contribute to the mechanical production of marine aerosol, most notably wind-driven sea spray aerosol (SSA) (O'Dowd & de Leeuw, 2007). Sea surface temperature (SST) also contributes to SSA production across a wide range of wind speeds, and

prior field observations have observed that SST enhances the SSA when wind exceeds 5 m s^{-1} (S. Liu et al., 2021). Secondary sources are also contributed by the oxidation of precursor compounds (Kroll & Seinfeld, 2008; Lewis & Schwartz, 2004). As such, aerosol production is

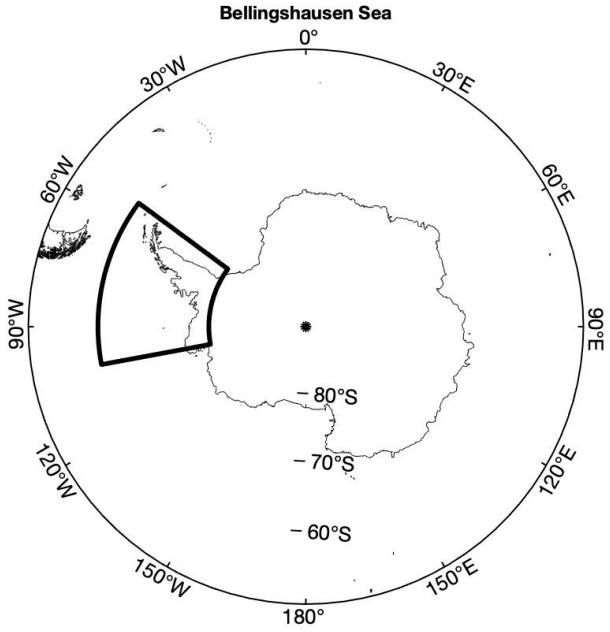

Figure 1. Map of the Bellingshausen Sea spatial grid located between 100 °W to 54 °W and 60 °S to 75 °S.

influenced by physical and biological processes including wind stress, SST, water column stability, sea ice melt, and the timing and magnitude of phytoplankton blooms (Figure 2.1.) (Ardyna et al., 2014; Tremblay & Gagnon, 2009).

To characterize the presence of marine tropospheric aerosol in the Bellingshausen Sea, I took advantage of the capabilities of NASA Earth-observing satellites. Our use of satellite remote sensing provides the unique advantage of sampling across multiple years and extended spatial scales, necessary for understanding the changing dynamics of polar environments. This is significant as polar environments are notoriously difficult to sample for a multitude of reasons including adverse weather, difficulty in transporting instruments and sensors, and lack of

sunlight in wintertime. As a result, *in situ* datasets are often intermittent and sparse in their completion, sometimes missing entire seasons. However, such field data enables ground-truthing of satellite observations enabling more reliable interpretations. Satellite remote sensing therefore complements *in situ* measurements by providing synergistic observations of challenging environments that have transformed the study of the polar Earth-Ocean-Atmosphere System (Comiso & Hall, 2014).

Prior studies have observed variation in the timing and magnitudes of marine aerosol production in relation to environmental drivers, with studies in high-latitude environments supporting a biogenic component of marine aerosol observations due to the coincident timing of seasonal sea ice melt and phytoplankton production. These processes can foster wind-driven SSA, the formation of primary organic aerosol, and the growth of sea spray from volatile organic compounds (Becagli et al., 2016; Brooks & Thornton, 2018; Leck & Bigg, 2005; Liss et al., 2000; Orellana et al., 2011; Stefels, Steinke, Turner, Malin, & Belviso, 2007; Trevena & Jones, 2006). In contrast, other studies emphasize the anticorrelation between biological activity and marine aerosol production with suppression of SSA production in relation to seasonal biological activity through processes affecting the sea surface microlayer (Dror et al., 2018; Fuentes, Coe, Green, de Leeuw, & McFiggans, 2010; Modini, Russell, Deane, & Stokes, 2013; K. Sellegri, O'Dowd, Yoon, Jennings, & de Leeuw, 2006). Disparate findings across these studies underscore the broad uncertainty in the degree of biological and physical influence on marine aerosol production across ocean basins.

To address the challenges associated in quantifying marine aerosol in polar environments, I developed a novel method using the NASA Cloud-Aerosol Lidar with Orthogonal Polarization (CALIOP) onboard the Cloud-Aerosol Lidar and Infrared Pathfinder Satellite Observation

(CALIPSO). I developed layer-integrated Marine aerosol optical depth (MAOD) — retrieved in high-latitude winter despite lack of solar radiation – and used MAOD to characterize these aerosols (Dasarathy et al., 2021). MAOD is devoid of cloud contamination, quality assurance screened, and confidently identified as clean marine aerosol through the CALIOP aerosol classification scheme (Kim et al., 2018). Thus, I address the of lack of nighttime retrievals and cloud contamination from satellite-based passive sensor retrievals of aerosol optical properties from the Moderate Resolution Imaging Spectroradiometer (MODIS) aboard the Aqua satellite and the Sea-viewing Wide Field-of-view Sensor (SeaWiFS).

In Chapter 1 of this dissertation, through use of NASA Earth-observing satellite capabilities and development of MAOD, I present seasonal trends in marine tropospheric aerosol arising from the interplay between physical, chemical, and biological processes in the polar sea ice habitat of the Western Antarctic Peninsula (WAP). I hypothesized that phytoplankton bloom periods, alongside melting of sea-ice, are associated with the release of biogenic sulfur species thereby contributing to aerosol formation, agreeing with earlier observations by Gabric et al. (2005, 2018). As such, I examine the seasonal variability of MAOD alongside fluctuations in chl-*a* and sea ice extent and observed distinct patterns of aerosol presence in the WAP marine tropospheric layer associated with seasonal fluctuations in sea ice extent and phytoplankton bloom dynamics, thus suggesting a biogenic component to aerosol presence (Dasarathy et al., 2021).

In Chapter 2, I examined the scale-dependent effects of oceanic factors on marine aerosol production. I further examined MAOD alongside another variable, coarse-mode Aerosol Optical Depth (AOD_C) retrieved from the Moderate Resolution Imaging Spectroradiometer (MODIS) Aqua. As sea spray aerosol accounts for the vast majority of supermicron aerosol in remote

oceanic regions (de Leeuw et al., 2011; Fitzgerald, 1991), AOD_C is a good proxy for SSA in the remote Bellingshausen Sea atmosphere. Through use of MAOD and AOD_C alongside retrievals of other physical and biological variables, our objective in this chapter was to examine whether MAOD and AOD_C correlated to wind speed across time scales in the Bellingshausen Sea. I also further assessed across open ocean and coastal regions whether MAOD and AOD_C were suppressed during periods of high wind speed and high biological activity in contrast to periods of low biological activity. I found that daily wind speed was significantly correlated with increasing MAOD and AOD_C indicating likely sea spray aerosol. I further found that MAOD and AOD_C increased or remained constant with wind speed during the biologically productive austral summer, which supports biological enhancement rather than suppression of MAOD and AOD_C magnitudes in summer (Dasarathy et al., 2023).

In Chapter 3, I further examined the physical and biogeochemical environment of the Bellingshausen Sea. I examined how changes to the presence, timing, and magnitude of sea ice affect biogeochemical diagnostics by conducting a perturbation experiment with increased and decreased magnitudes of sea ice. To isolate the impact of sea ice, I perturbed sea ice albedo and examined whether differences to an ice-free duration and extent leads to changes in biomass and structure of small and large phytoplankton groups. I also examined the effects on the other biogeochemical and physical diagnostics including mixed layer depth (MLD), phytoplankton growth rate, net primary and community production (NPP and NCP), particulate organic carbon (POC), and nutrient concentrations of iron and nitrate. I thereby answer the following (1) How does perturbing sea ice albedo impact the timing and magnitude of sea ice melt in spring and freezing in late fall? Is the timing of freezing the same, or is there delayed onset of sea-ice return? (2) What is the impact on the MLD? (3) How do these changes affect the distribution of

biogeochemical diagnostics small and large phytoplankton biomass, particulate organic carbon (POC), net primary production (NPP), net community production (NCP), phytoplankton growth rate, and iron and nitrate concentration in the Bellingshausen Sea?

CHAPTER 1: MULTI-YEAR SEASONAL TRENDS IN SEA ICE, CHLOROPHYLL CONCENTRATION, AND MARINE AEROSOL OPTICAL DEPTH IN THE BELLINGSHAUSEN SEA

1. Introduction

In the remote polar sea ice environment of the Bellingshausen Sea, the formation and presence of marine tropospheric aerosol is coupled with physical, chemical, and biological processes. Present in both the Antarctic and Arctic, sea ice habitats are among the largest ecosystems on our planet (Kevin R. Arrigo, 2014). They are subject to a number of physical processes due to the inherent temporality of high-latitude environments, from the seasonal dynamics of variable light availability, increases and decreases in sea ice extent and thickness, fluctuations in nutrient availability, and fluctuations in the timing and magnitude of primary production and chlorophyll-*a* (chl-*a*) concentration (Ardyna et al., 2014; Tremblay & Gagnon, 2009). This inherent seasonality of high latitude environments has distinct impacts on the formation and presence of marine tropospheric aerosol. Numerous field campaigns have found statistically significant increases in aerosols and aerosol precursors, including dimethylsulfide (DMS) and organohalides, associated with the melting of sea ice (Becagli et al., 2016; Liss et al., 2000; Stefels et al., 2007; Trevena & Jones, 2006). Furthermore, seasonal dynamics in these high latitude environments are intrinsically tied to increasing light availability and solar insolation that occurs at the onset of the bi-hemisphere spring and summer (McCoy et al., 2015). This in turn impacts the timing of phytoplankton blooms thereby fostering the formation of primary organic aerosol, growth of sea spray from organic matter enrichment, and presence of aerosol precursors and marine gels with the ability to seed biogenic aerosol (Brooks & Thornton, 2018; Chen et al., 2012; Leck & Bigg, 2005; Orellana et al., 2011). These aerosols may also influence the regional climate of remote environments, either directly through absorption and scattering of solar

radiation, or indirectly by acting as cloud condensation nuclei (CCN), thereby influencing cloud dynamics, including albedo and lifetime (Coakley et al., 1983; Gabric et al., 2018; McCoy et al., 2015).

To characterize the presence of marine tropospheric aerosol in the Bellingshausen Sea, we took advantage of the capabilities of NASA Earth-observing satellites. Our use of satellite remote sensing provides the unique advantage of sampling across multiple years and extended spatial scales, necessary for understanding the changing dynamics of polar environments. This is significant as polar environments are notoriously difficult to sample for a multitude of reasons including adverse weather, difficulty in transporting instruments and sensors, and lack of sunlight in wintertime. As a result, *in situ* datasets are often intermittent and sparse in their completion, sometimes missing entire seasons. However, such field data enables ground-truthing of satellite observations enabling more reliable interpretations. Satellite remote sensing therefore complements *in situ* measurements by providing synergistic observations of challenging environments that have transformed the study of the polar Earth-Ocean-Atmosphere System (Comiso & Hall, 2014).

Remote sensing-based studies that have focused on aerosol formation and distribution and links to chl-*a* concentration and sea ice dynamics have thus far used passive sensor retrievals of aerosol optical properties (Gabric et al., 2005, 2018). In one study, Gabric et al., (2005) observed the seasonality of aerosol optical depth (AOD) across distinct regions of the Southern Ocean. They correlated AOD with other variables including sea ice and chl-*a*, finding strong synchrony. A later study by Gabric et al., (2018) similarly examined AOD in the Arctic and observed that peaks in AOD occur alongside melt of sea ice and increases in annual primary productivity and biomass. Across both studies, the authors attributed seasonal AOD to a biogenic

source of aerosols. These studies have helped resolve many of the challenges of *in situ* measurements; but, passive sattelite-based retrievals such as AOD can be subject to — and biased by — cloud presence not distinguished from aerosol, signal uncertainty, and algorithm biases present within optical depth retrievals (Kaufman et al., 2005; Toth et al., 2013). Further, passive sensor retrievals cannot retrieve nighttime data, and thus cannot quantify AOD in high latitude wintertime (Behrenfeld et al., 2017; Kittaka et al., 2011). Despite considerable effort in these studies, a lack of wintertime reporting of AOD leads to incomplete seasonal observations (Gabric et al., 2005, 2018).

To address challenges of passive sensor retrievals, we have developed a novel method of quantifying low-lying aerosols with the NASA Cloud-Aerosol Lidar with Orthogonal Polarization (CALIOP) onboard the Cloud-Aerosol Lidar and Infrared Pathfinder Satellite Observation (CALIPSO). Marine aerosol optical depth (MAOD) — retrieved in high-latitude winter despite lack of solar radiation – is used to characterize these aerosols. MAOD is devoid of cloud contamination, quality assurance screened, and confidently identified as clean marine aerosol through the CALIOP aerosol classification scheme (Kim et al., 2018). Thus, we address the of lack of nighttime retrievals and cloud contamination from satellite-based passive sensor retrievals of aerosol optical properties from the Moderate Resolution Imaging Spectroradiometer (MODIS) aboard the Aqua satellite and the Sea-viewing Wide Field-of-view Sensor (SeaWiFS). Our study is the first marine-only optical depth analysis of the Bellingshausen Sea region and improves on prior Southern Ocean-scale AOD measurements by reducing the bias from clouds and overlying aerosol contamination as observed in Kaufman et al. (2005) and Toth et al. (2013). MAOD advances on the capability of prior AOD measurements from passive sensors linked with biogenic aerosol presence as in Gabric et al. (2005, 2018).

Gabric et al. (2005, 2018) attribute seasonal AOD to a biogenic source of aerosols. Our objective in this work is to evaluate whether seasonal trends of the active remote sensing data product, MAOD, reflect the seasonality of AOD observed in these prior studies. Herein, we present seasonal trends in marine tropospheric aerosol arising from the interplay between physical, chemical, and biological processes in the polar sea ice habitat of the Western Antarctic Peninsula (WAP). We hypothesized that phytoplankton bloom periods, alongside melting of sea-ice, are associated with the release of biogenic sulfur species thereby contributing to aerosol formation, agreeing with earlier observations by Gabric et al. (2005, 2018). As such, we examine the seasonal variability of MAOD alongside fluctuations in chl-*a* and sea ice extent. We observed distinct patterns of aerosol presence in the WAP marine tropospheric layer associated with seasonal fluctuations in sea ice extent and phytoplankton bloom dynamics, thus suggesting a biogenic component to aerosol presence. This work enhances our knowledge of the interactions between oceanographic parameters, the surface ocean biosphere, and biogenic aerosol formation in polar environments.

2. Data Sources and Methods

2.1. Satellite Data Retrieval & Computation

All satellite data were obtained from June 2006 to December 2018 across the spatial grid between 100 °W to 54 °W and 60 °S to 75 °S. Sea ice detections and MAOD retrievals were obtained from CALIOP onboard CALIPSO (Winker, 2018), chl-*a* retrievals were obtained from MODIS Aqua (NASA Ocean Biology Processing Group, 2017), and surface wind speed retrievals were obtained from the Advanced Microwave Scanning Radiometer for the Earth Observing System (AMSR-E). Southern hemisphere seasons are defined as winter: June 1st to

September 1st, spring: September 1st to December 1st, summer: December 1st to March 1st, fall: March 1st to June 1st.

Methods for retrieving MAOD, chl-*a*, depolarization ratio (ice), and wind speed follow. All coding scripts for calculation and plotting of these data can be downloaded from GitHub at https://github.com/srdasara/Multiyear_SeasonalTrends_BellingshausenSea.

2.1.1. Marine Aerosol Optical Depth (MAOD)

MAOD was calculated from tropospheric clean marine aerosol retrievals from CALIOP onboard CALIPSO. Nighttime and cloud-free MAOD profiles were used in these analyses to avoid noise from solar background light associated with daytime retrievals and scattering from clouds, respectively (Toth et al., 2013). Extinction coefficients at 532 nm were obtained from Level 2 5 km Aerosol Profile Products, version 4.20. This version of CALIPSO data products reduces biases in the aerosol optical properties retrievals by using the significantly improved calibration that was achieved by raising the calibration altitude to a nearly aerosol-free region in the stratosphere (Getzewich et al., 2018; Kar et al., 2018). These extinction coefficients were all derived from layers initially classified as clean marine tropospheric aerosol (Kim et al., 2018), with additional quality assurance screening applied as prescribed by Tackett et al. (2018). Cloud-aerosol discrimination (CAD) scores greater than −20 and less than –100, indicating no confidence in the CAD assessment, were screened out to avoid possible cloud contamination (Liu et al., 2019). Extinction QC flags other than 0 and 1 were rejected to prevent potential biases due to aerosol misclassification in the reported extinction values (Young et al., 2018). Extinction coefficients flagged with estimated uncertainties of 99.99 km^{-1} were rejected to avoid spuriously large, highly uncertain extinction values near the surface (Young et al., 2018).

Situations where data is rejected due to these requirements are most often where there is significant overlying attenuation due to other features, especially optically thick clouds (Tackett et al., 2018). Only cloud-free nighttime profiles are considered for this analysis. Of these, the fraction of clean marine extinction coefficients that pass all quality assurance tests is 44.5 % out of all data evaluated in this spatiotemporal record.

Using these methods, only quality assured clean marine tropospheric aerosol extinction coefficient retrievals were used in calculating MAOD profiles. Clean marine tropospheric aerosol extinction coefficients were integrated using trapezoidal integration across pre-specified altitude range bins from roughly sea level to 2 km to capture the bulk of the marine aerosol signal, further explored in Supporting Information S1.1 and visualized in Figure S1.1. Due to the 60 m vertical sampling interval of CALIOP level 2 products, this corresponds to range bins of 0.0378 km to 2.0137 km. When sea ice presence is suspected, as determined by the lidar depolarization ratio, the lower altitude is moved upward by one range bin to 0.0977 km to avoid potential contamination of the atmospheric signal by ice protruding above the ocean surface. MAOD is therefore computed as:

$$\text{MAOD} = \int_{\mathbf{r_{surface}}}^{\mathbf{r_{top}}} \boldsymbol{\sigma_{cm}}(\boldsymbol{r})\boldsymbol{dr} \quad (1)$$

Where $r_{surface}$ = 0.0378 km OR 0.0977 km, r_{top} = 2.0137 km, and $\sigma_{cm}(r)$ is the vertically resolved clean marine aerosol extinction coefficient. This altitude range was chosen as it most often

captured the clean marine aerosol signal. Beginning the integration at 2.0137 km encompasses the marine boundary layer in all seasons.

Numerous studies have compared AOD from CALIOP to coincident AOD retrievals from spaceborne and ground-based instruments (Kim et al., 2013; Omar et al., 2013; Redemann et al., 2012; Schuster et al., 2012). These studies consistently report that AOD retrievals from CALIPSO are underestimates in comparison to retrievals acquired from these other sensors. Furthermore, past work on the low bias of undetected aerosol layers has shown lower detection limits of total column AOD. Kim et al. (2017) found a 'missing AOD' estimate of 0.025 ± 0.021 for nighttime measurements of total column AOD over both land and water. As such, in comparison to MAOD, this is an overestimate of the undetected AOD between the surface to 2.0137 km used in the calculation of MAOD (equation 1).

Because the information contained in the CALIOP backscatter signal is insufficient for discerning the constituent components of the detected aerosol layers, the MAOD we derive from the CALIOP aerosol data cannot be considered as a direct assessment of biogenic aerosol presence. However, our derivation of MAOD from quality-screened and subtyped extinction coefficient profiles allows us to directly evaluate the vertical variability of aerosol in the marine boundary layer, which is especially relevant over the ocean where the aerosol source is the ocean itself. Our calculation of MAOD also overcomes difficulties encountered in the way layers are detected and reported at multiple resolutions in the standard CALIOP data products. For example, the CALIOP layer products frequently identify multiple, apparently distinct layers with

spatially overlapping boundaries in the same 5 km column. In these cases, determining the true optical depth of specific aerosol types within a column can be challenging (Tackett et al., 2018).

It is also important to note that the CALIOP backscatter measurements (and hence the CALIOP extinction retrievals) are not equally sensitive across all regions of the marine aerosol size distribution. Prior studies indicate that the submicron range dominates total aerosol composition, with bimodal distributions of biogenic aerosol species including non-sea-salt (NSS) sulphate aerosol, nitrate, water-soluble organic carbon, and methane sulfonic acid (MSA) derived from DMS having diameters from 50 nm to 1 micron (Brechtel, Kreidenweis, & Swan, 1998; Cavalli, 2004; Rathke, Notholt, Fischer, & Herber, 2002). Forestieri et al. (2018) found that change in size range of particles < 1 micron in diameter does occur with biological activity. Based on Mie scattering computations using representative size distributions for marine aerosols, aerosols having radii less than 1 micron are seen to contribute a substantial fraction of the CALIOP backscatter measured at 532 nm (Tackett, 2009). However, these contributions decrease sharply for particles with radii below ~100 nm. Studies have also found seasonal cycles of sea spray production associated with the enrichment of primary organic aerosol (O'Dowd et al., 2004; Rinaldi et al., 2013). Our observations of trends in MAOD do not contradict these studies, as these primary organic aerosol particles are typically smaller in diameter than those which CALIOP is most sensitive to, having maximum diameters of about 200 nm (O'Dowd et al., 2004).

2.1.2. Chl-a

Chl-*a* concentrations were obtained from Level 3 (4 x 4 km^2) monthly mapped data products across the spatiotemporal range specified. These mapped values were averaged for

temporal analysis. As MODIS Aqua is a passive sensor that relies on ambient solar radiation from daytime conditions, data is missing from May until September as a result of persistent nighttime only conditions. We thus obtained monthly averages from June 2006 to December 2018, apart from annual missing data. Computation of mean values across this region can be a potential source of error due to missing data caused by ice presence and cloud cover, as well as sun glint contamination which may affect the quality of retrievals (Feng & Hu, 2016). In calculation of the mean, missing values were excluded, thereby indicating the calculated mean values could be different than reality. Nevertheless, chl-*a* retrievals from MODIS Aqua may often underestimate true values in the Southern Ocean by a factor of 2 to 3, particularly when chl-*a* is greater than 0.3 mg m^{-3} (Jena, 2017).

2.1.3. Ice

When the CALIPSO orbit transects surfaces covered by ice, whether land or ocean, digitizer saturation often occurs in both perpendicular and parallel 532 nm channels at the Earth's surface and altitudes immediately below (Lu et al., 2018). When the signals from these channels are ratioed, termed surface integrated depolarization ratio (δ), the resulting values are in the range of 0.65 to 1.1. Conversely, when CALIPSO transects surfaces covered by water, the signal intensity is substantially reduced, most especially in the perpendicular channel, and the resulting depolarization values are between 0.0 to 0.15. Sea ice was thus identified using the CALIOP surface depolarization ratio. These values are consistent with passive microwave-based retrievals of sea ice (Lu et al., 2017). Depolarization ratios were quality screened such that values ≤ -0.2 and > 1.2 were rejected from these analyses. Using thresholds from Lu et al. (2017), values less than 0.15 were taken to indicate open water, 0.15 to 0.65 indicated a mix between

open water and sea ice (i.e. the marginal ice zone), and values greater than 0.65 indicated ice presence.

2.1.4. Winds

Wind speed data were obtained from AMSR-E. Medium-frequency products were used to determine wind speeds at 10 m above the Earth's surface (units: m s^{-1}). Only physically plausible wind retrievals were used in this analysis by filtering out wind speeds $\leq$ 0 m s^{-1} and $>$ 50 m s^{-1}, indicating data outside of valid ranges (Wentz et al., 2003). AMSR-E medium frequency wind speed data products are missing from August 2011 to July 2012 and January 2016 to March 2016. Missing data also occurs as a result of persistent ice presence in the high-latitude region examined in our study. Wind speed analysis is further described in Supporting Information S1.1.

2.2. Time-Series & Statistical Analyses

The construction of time-series, spatial grids, and statistical analyses for all variables – MAOD, chl-*a*, ice, and wind speed – follows. Section 2.2.1 discusses the construction of time-series, and section 2.2.2. examines a monthly-lagged cross correlation study. Section 2.2.3 discusses the construction of seasonal spatial grids of all variables, which are later used in a correlation analysis described in section 2.2.4.

2.2.1. Monthly-averaged Time-Series

Time-series were constructed for MAOD, ice, and wind speed by averaging profile values across monthly time steps throughout the spatial grid. Time-series for chl-*a* were constructed by averaging mapped chl-*a* concentration values across the same spatial grid across

each month. Mean absolute deviations (MAD), the average of absolute deviations around the data's mean (Franklin, 2007), were calculated to determine variability in measured averages.

2.2.2. Spearman's rho, Monthly Lag

Cross correlations with time lags were performed so that we could examine Spearman's rho at various monthly lags (L) between monthly-averaged time-series for MAOD, chl-*a*, ice, and wind speed. Spearman's rho is a nonparametric test for assessing the strength of association between two variables when calculated from the ranks of the data versus their actual values (Akoglu, 2018). Rho was computed for lag periods of $-6 < L < +6$ months, and the time-series of MAOD was lagged with respect to time-series of chl-*a*, ice, and wind speed. For example, a lag of +L meant that we were comparing the time-series of chl-*a* ($t = t_0$) with a lagged effect on MAOD ($t = t_0 + L$). Discontinuities were maintained between time-series, and rho was computed only between points in time when no missing values were present in either of the two datasets.

2.2.3. Spatial Gridding

Spatial grids were constructed for MAOD, ice, and wind speed. Bin sizes were specified as 1 ° latitude x 1 ° longitude. Profiles of MAOD, ice, and wind speed that fell within each spatial bin for each individual season were determined and the seasonal means were calculated. This method was used to construct seasonal 3D arrays with dimensions corresponding to size 1 ° x 1 ° x season for MAOD, ice, and wind speed. In calculating the mean within spatial bins, missing values were excluded, thereby indicating that the calculated mean value could be slightly different than reality.

Arrays of chl-*a* were constructed by first seasonally subdividing the Level 3 (4 x 4 km^2) monthly mapped data products and temporally averaging across each season. The spatial resolution was then adjusted by averaging pixels to match the same spatial resolution of constructed seasonal arrays of MAOD, ice, and wind speed (1 ° x 1 ° latitude-longitude x season). Computation of the chl-*a* array across this region can be a potential source of error due to missing data. Missing values were excluded when calculating the mean across each pixel.

2.2.4. Spatial Correlation Calculation

Pearson's correlation coefficient was used to examine the spatial relationship between grids of MAOD, chl-*a*, sea ice presence (as depolarization ratio, δ), and wind speed. In correlations examining sea ice presence or absence, spatial pixels indicating open ocean were masked as NaN. Following construction of 3D arrays as in section 2.2.3., correlation coefficients were calculated across the time dimension of each array at each 1 ° x 1 ° latitude-longitude pixel. Using this method, a spatial grid of correlation coefficients was constructed. To examine whether correlations of the same positive or negative sign are expected to cluster together, as visualized in between grids of MAOD, chl-*a*, ice, and wind speed, spatial correlations were calculated using the same method described above on a null model of randomly generated numbers from the normal distribution with NaNs indexed in the same positions as data variables. As all variables violated the Anderson-Darling test of normality, the Kruskal-Wallis test was used to test the null hypothesis that the spatial correlations come from the same population as the spatial correlations from the null model. With the exception of the random model against MAOD & chl-*a*, all medians are significantly different from random, with the random model against MAOD & windspeed close to the significance threshold of $p < 0.05$ (Table S1.1).

2.3. Climatology Analyses

Spatial seasonal climatologies for all variables were constructed by seasonally averaging MAOD, ice, wind speed, and chl-*a* using methods similar to those described in section 2.2.3. Spatial bins were specified as 1 ° x 1 ° latitude-longitude for the entire spatial grid. The mean for all MAOD, ice, and wind speed profiles within each bin was calculated for each season throughout the entire temporal range of analysis. This method was used to construct seasonal climatologies at 1 ° x 1 ° latitude-longitude resolution for MAOD, ice, and wind speed. Seasonal climatologies of chl-*a* were constructed by first seasonally subdividing the Level 3 (4 x 4 km^2) monthly mapped data products and temporally averaging across each season. The spatial resolution was then adjusted by averaging pixels to match the same spatial resolution of constructed seasonal climatologies of MAOD, ice, and wind speed.

3 Results

3.1. Temporal Trends: Multi-year time-series and lagged correlation analyses

3.1.1. Interannual trends in MAOD, chl-*a*, and ice

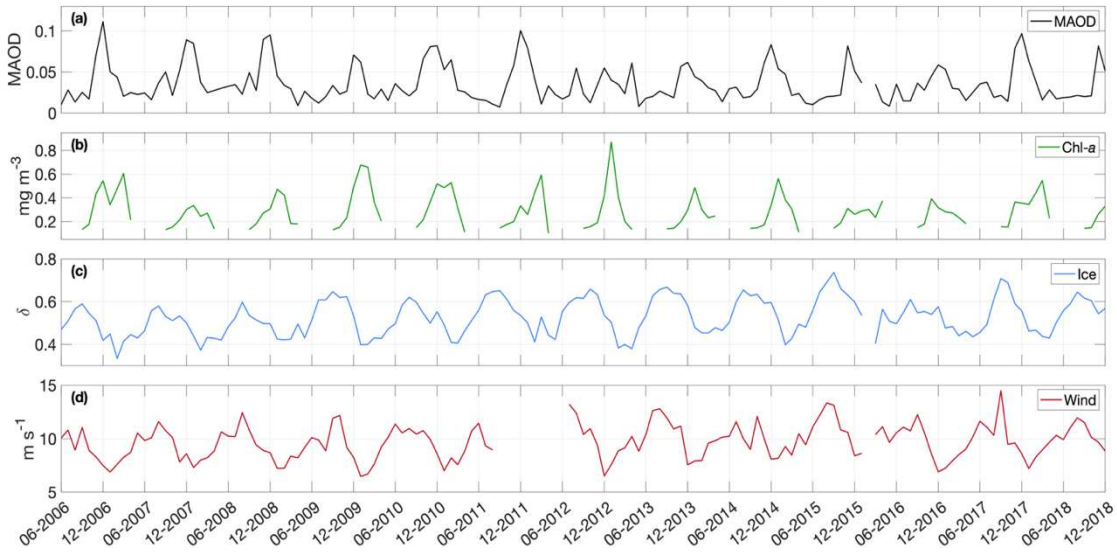

Figure 1.1. Time-series plots (monthly averaged) of (a) marine aerosol optical depth (MAOD) (b) chlorophyll-*a* concentration (chl-*a*), (c) depolarization ratio, and (d) wind speed. Missing data is present in MAOD and depolarization ratio due to a satellite GPS anomaly. Annual gaps in chl-*a* are a result of seasonal nighttime conditions.

Seasonal trends in MAOD occur throughout the time-series (Figure 1.1.a). The maximum typically occurs in summer from December to January and decreases from January to March. Minimum values exhibit variability in time of occurrence and vary in their magnitude from late fall until spring (May to October). Magnitudes of maxima range from 0.06 ± 0.04 to 0.11 ± 0.09, and minima range from 0.01 ± 0.01 to 0.02 ± 0.02. The timing of this seasonality of MAOD occurs consistently throughout this record. MAOD decreases following the December to January maximum, and increases in spring starting in September to October, with the magnitude of summertime maxima exhibiting variability. The greatest summertime maximum occurs in December 2006 at 0.11 ± 0.09, and the lowest in December 2012 of 0.06 ± 0.04. Interestingly,

preceding the typical December to January maximum in MAOD observed throughout this time-series, an initial pulse in MAOD occurs in late winter to early spring (July to September) across multiple years. For example, in September 2008, an initial pulse of 0.05 ± 0.05 in MAOD occurs, followed by a brief decrease to 0.03 ± 0.04 in October, after which MAOD greatly increases until the summertime maximum in December of 0.1 ± 0.06. The high MAD indicates the large spread of these data across the spatiotemporal region of interest; nevertheless, the initial pulse in MAOD that precedes the main peak is a recurring trend in our temporal dataset not found in

prior studies due to the lack of an AOD signature from passive sensor retrievals in winter and early spring months.

Chl-*a* exhibits strong annual seasonality throughout the multi-year record. (Figure 1.1.b).

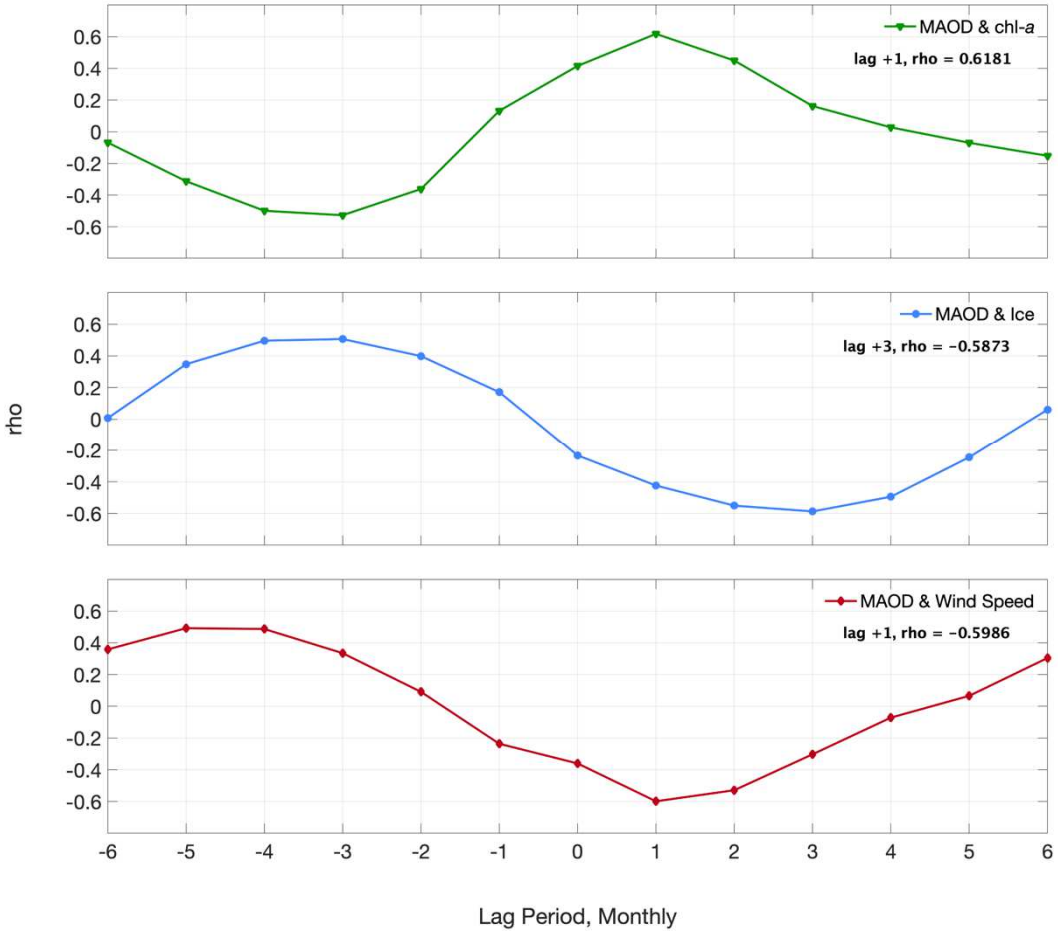

Figure 1.2. Temporal correlation between (a) marine aerosol optical depth (MAOD) and chlorophyll-*a* concentration (chl-*a*), (b) MAOD and Ice, and (c) MAOD and Wind Speed. The lag period indicates the number of months the timeseries of MAOD is shifted while timeseries of chl-*a*, ice, and wind speed are kept constant. For example, in (a), a lag of +1 indicates that MAOD is shifted forwards one month while the chl-*a* timeseries remains stationary, i.e., with one month as a given example, the December maximum in MAOD corresponds to the January maximum in chl-*a*.

A seasonal increase typically begins in spring from September to October, with a maximum occurring annually in the summer to early fall between December to March. An annual decrease

follows this maximum, beginning in fall from March to May. The greatest and lowest magnitudes in summertime chl-*a* occurred in January 2013 at 0.87 ± 1.16 mg m^{-3} and February 2016 at 0.30 ± 0.26 mg m^{-3}, respectively. The high MADs indicate the large spread of these data across the spatial grid, also visualized in Figure 1.3.

The interannual seasonal variability present in MAOD and chl-*a* is also present in sea ice (Figure 1.1.c). Variation exists in the timing of the monthly maxima and minima; nevertheless, seasonality in the formation and melt of ice persist annually. The minimum and maximum typically occur late in January and August, respectively. A minimum in ice extent occurs in February from 2007 to 2011, with depolarization ratio values ranging from 0.33 ± 0.36 to 0.41 ± 0.39 before increasing until the wintertime maximum. From 2011 to 2018 in the multi-year time-series, lengthening of the summertime ice-free season by ~89 days occurs as ice extent reaches a minimum in February and persists until May until the end of the temporal range of record (Figure 1.1.c). 2017 is a particularly low ice year in our record, and the summer ice extent persists from January to June, with a minimum in May of 0.44 ± 0.38, indicating the lengthening of summertime ice melt in our study from 2006 to 2018. The large MAD is explained by the spread of these data in the spatial grid across seasons of interest, also visualized in Figure 1.5.

3.1.2. Lagged Correlation Analysis between MAOD and chl-*a*

The seasonality between MAOD and chl-*a* was examined using a lagged correlation analysis (Figure 1.2.) with Spearman's rho. In doing so, the multi-year time series of MAOD was shifted while time series of chl-*a,* sea ice, and wind speed were kept constant. With respect to chl-*a*, the greatest magnitude of rho occurs when the time series of MAOD is shifted forwards one month. This indicates a lag of +1, and MAOD and chl-*a* are in-phase as observed by the

positive magnitude of rho (lag +1, rho = 0.6181). As rho is positive, this further indicates that MAOD reaches a maximum and minimum one month before the maximum and minimum in chl-*a* occurs, respectively. These trends are also visualized in Figure 1.1.a, where multiple years have a December maximum in MAOD that precedes the January maximum in chl-a, also present in the monthly temporal climatology (Figure S1.5). Nevertheless, this relationship exhibits variability across years. When MAOD is not shifted, the correlation remains high (lag 0, rho = 0.4154). As such, an increase in MAOD occurs alongside, or even slightly before, an increase in chl-*a*.

3.1.3. Lagged Correlation Analysis between MAOD and Ice

We examined seasonality in the relationship between MAOD and ice in Figure 1.2. using lagged correlation analysis. The greatest magnitude of rho occurs when MAOD is shifted forwards three months, indicating a lag of +3, and when these time-series are out of phase (lag +3, rho = −0.5873). As rho is negative, this correlation indicates that MAOD reaches a seasonal summertime maxima three months before the summertime minima in ice presence, and the seasonal increase in MAOD is coincident with the seasonal melt in sea ice.

3.1.4. Lagged Correlation Analysis between MAOD and Wind Speed

We examined the influence of wind speed on the observed seasonality of MAOD (Figure 1.2). The greatest magnitude of rho between MAOD and wind speed occurs when MAOD is shifted forwards one month, indicating a lag of +1, and MAOD and wind speed are out of phase (lag +1, rho = –0.5986). MAOD therefore reaches a maximum one month before the minimum in wind speed occurs. When MAOD is not shifted, the correlation weakened (lag 0, rho = –0.3602).

We examine whether seasonal dynamics of increased wind speed are responsible for driving increases in MAOD linked to sea state and sea spray/salt further in Section 4.2.3.

3.2. Spatial Trends and Correlation Analyses

3.2.1. Spatial Seasonal Climatologies

Spatial trends of MAOD are observed in Figure 1.3. and reflect the seasonal variability exhibited in Figure 1.1.a. MAOD is lowest in winter, particularly evident in latitudes south of 66 °S. MAOD increases in southward extent from winter to summer, with values south of 66 °S

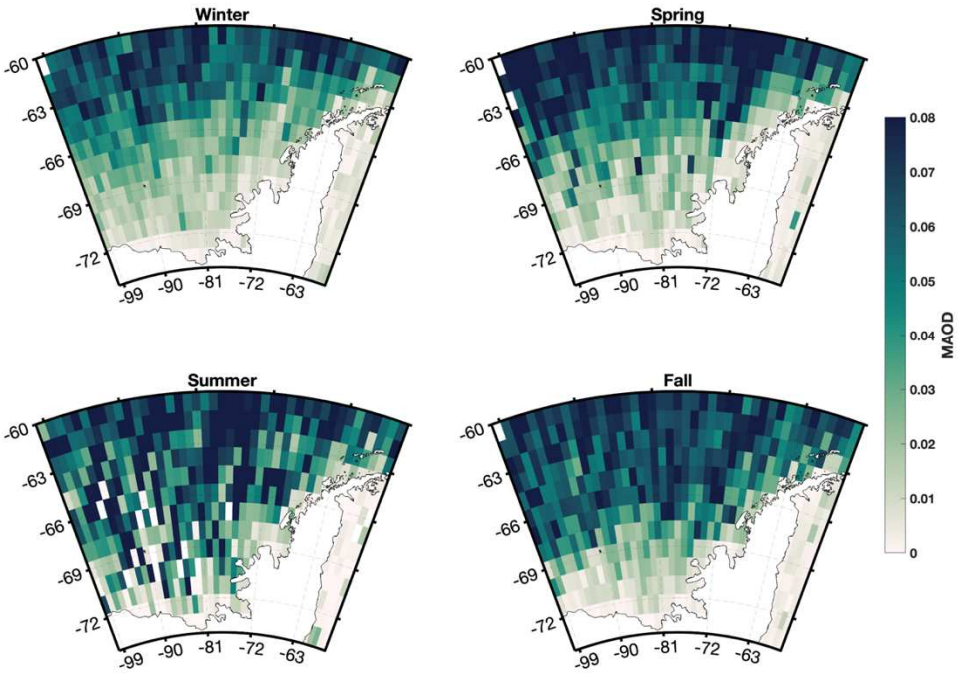

Figure 1.3. Seasonal climatology of marine aerosol optical depth (MAOD) from NASA CALIOP (1 ° x 1 ° latitude-longitude resolution). These data were obtained from June 2006 to December 2018 across the spatial grid between 100 °W to 54 °W and 60 °S to 75 °S. Southern hemisphere seasons are defined as winter: June 1st to September 1st, spring: September 1st to December 1st, summer: December 1st to March 1st, fall: March 1st to June 1st.

increasing from 0.02 to 0.03 in winter to 0.05 to 0.08 in summer. In fall, the southward

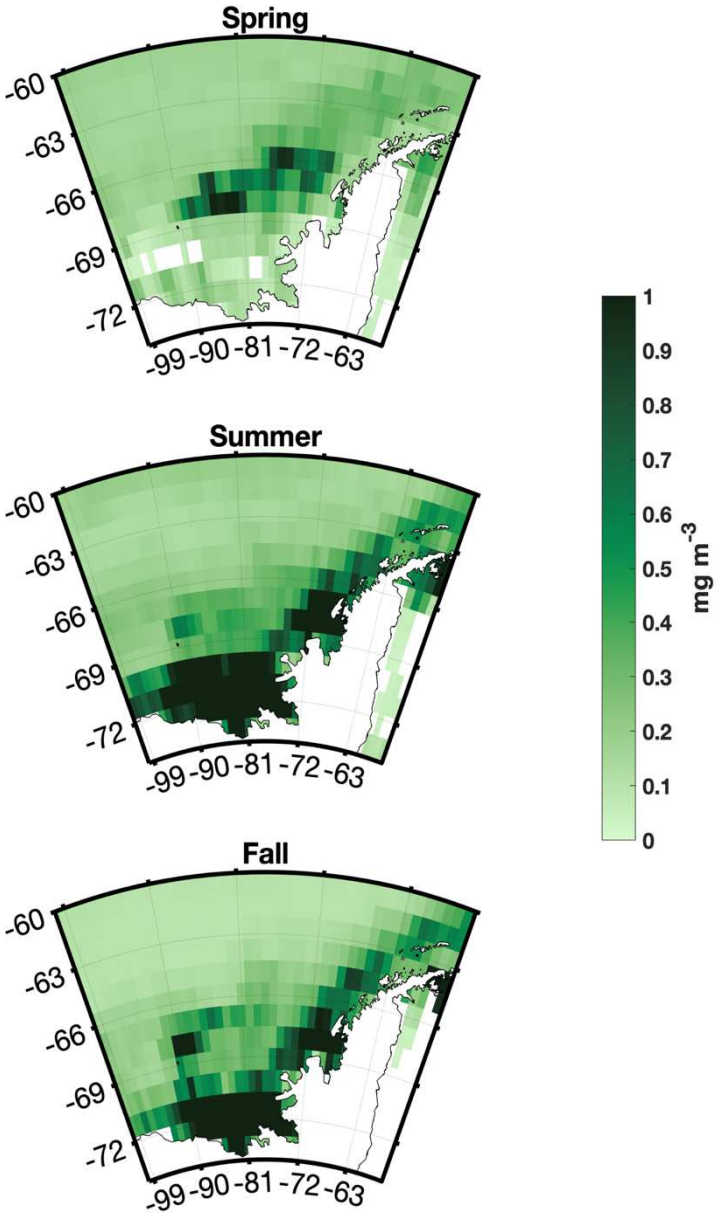

Figure 1.4. Seasonal climatology of chlorophyll-*a* concentration (chl-*a*) from MODIS Aqua (1 ° x 1 ° latitude-longitude resolution). These data were obtained from June 2006 to December 2018 across the spatial grid between 100 °W to 54 °W and 60 °S to 75 °S. Southern hemisphere seasons are defined as winter: June 1st to September 1st, spring: September 1st to December 1st, summer: December 1st to March 1st, fall: March 1st to June 1st. Wintertime corresponds to missing data as a result of nighttime conditions in this high-latitude region.

expansion of the pulse in MAOD diminishes, and values range from 0 to 0.05 south of 66 °S. Interestingly, north of 66 °S, wintertime MAOD is in the range of 0.03 to 0.08, similar to summertime MAOD south of 66 °S. This may be due to the seasonal enhancement of wind stress, as suggested by the spatial correlation between MAOD and wind speed, with correlation coefficients ranging from 0 to 0.7. This topic is explored further in section 4.3 (Figures S1.6, S1.8). Nevertheless, even at these lower latitudes, MAOD north of 66 °S increases from winter to summer. A decrease in magnitude and southward extent of MAOD is observed from summer to fall.

Spatial seasonal trends in chl-*a* are exhibited in Figure 1.4. Phytoplankton occur slightly away from the coastline in spring, with chl-*a* ranging from 0.1 to 1 mg m^{-3} south of 64 °S and between 90 °W and 71 °W. In the summer, an increase emerges southeastward and closer to the coastline, with chl-*a* ranging from 0.3 to 1.5 mg m^{-3}. This appears coincident to observed ice melt, and the spatial climatology of ice (Figure 1.5.) exhibits the same temporality seen in the multi-year time-series (Figure 1.1.c). The maximum and minimum extent of ice occurs in winter and summer, respectively. Nevertheless, variability in seasonal dynamics of melt and freeze occur, most notably the regional freezing in spring along the coastline north of 68 °S. A winter to spring polynya also persists west of 81 ºW and north of 68 ºS, with reduced ice cover in winter and therefore reduced melt in spring. This is coincident with an observed phytoplankton bloom in springtime west of 81 ºW (Figures 1.4, 1.5.). Ice extent generally remains low from summer to fall, indicating that most of the freeze to maximum ice extent in this area occurs in fall to winter, likely from May to September, reflected in the multi-year time-series (Figure 1.1.c).

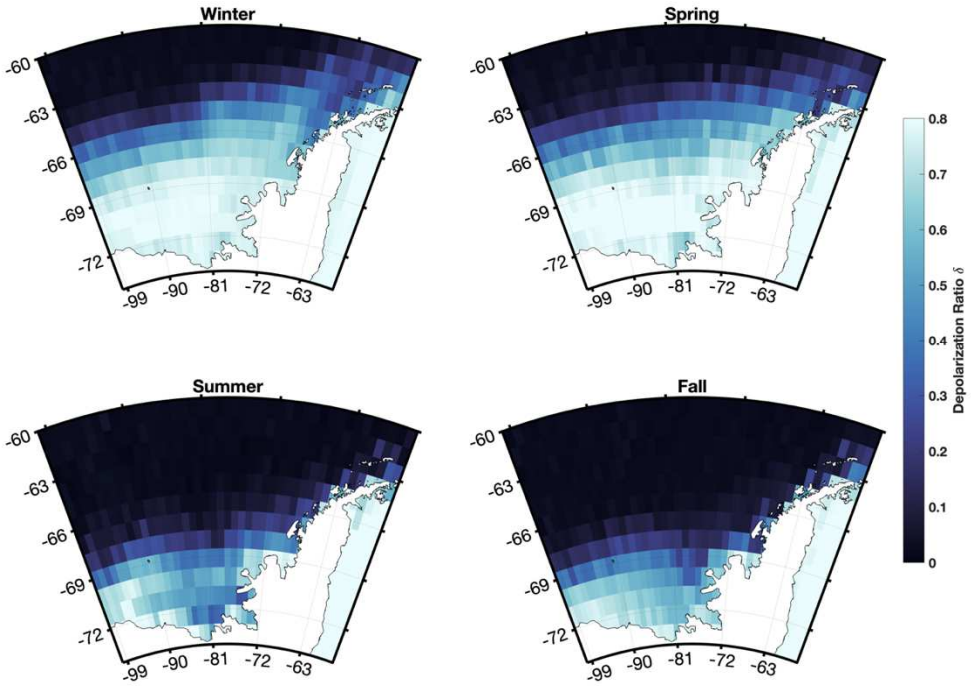

Figure 1.5. Seasonal climatology of ice represented as depolarization ratio from NASA CALIOP (1 ° x 1 ° latitude-longitude resolution). Values less than 0.15 indicate water presence, 0.15 to 0.65 indicate a mix between water and ice presence, and values greater than 0.65 indicate ice presence (thresholds from Lu et al., 2017). These data were obtained from June 2006 to December 2018 across the spatial grid between 100 °W to 54 °W and 60 °S to 75 °S. Southern hemisphere seasons are defined as winter: June 1st to September 1st, spring: September 1st to December 1st, summer: December 1st to March 1st, fall: March 1st to June 1st.

3.2.2 Spatial Correlations between MAOD, chl-*a*, and Ice

We examined the spatial correlation between MAOD, chl-*a*, ice, and wind speed to ascertain whether these data were spatially coherent, thereby indicating regional dynamics in the biogenic source of aerosol (Figures 1.6., 1.7.; discussion in Section 4.3). We first examine the relationship between MAOD and ice across seasons (Figure 1.6.). In winter, largely north of the ice edge and stretching southward, a predominantly negative relationship between MAOD and

ice is seen, with values ranging from –0.8 to 0.2. This likely indicates MAOD decreasing during freeze-up. Wintertime MAOD is in the range of 0.02 to 0.08 north of 66 °S, similar to southward

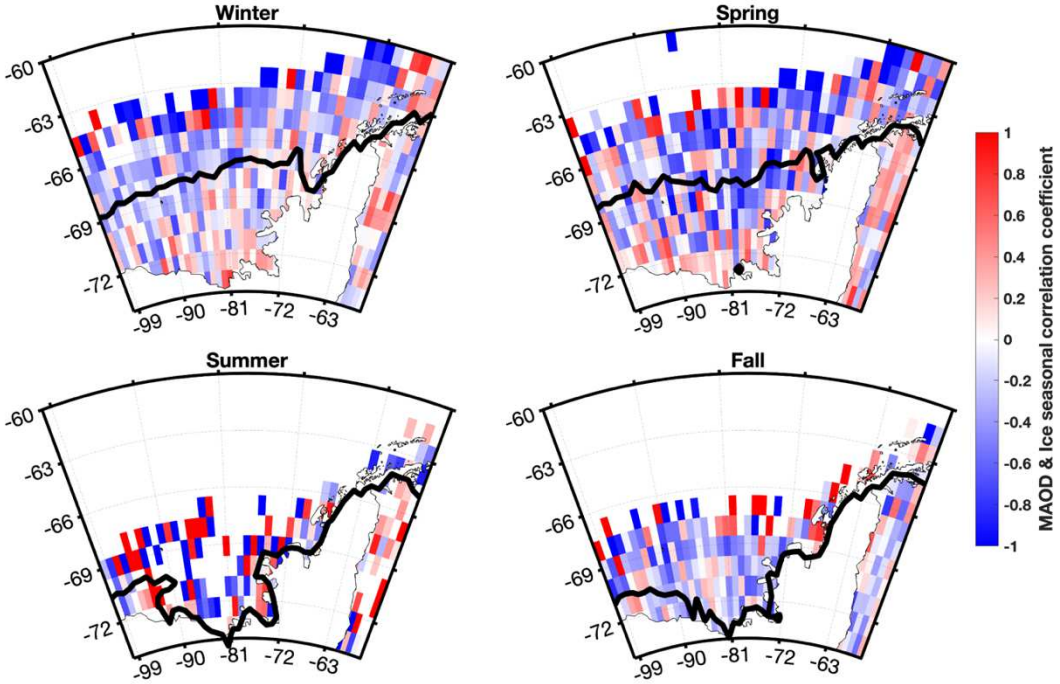

Figure 1.6. Seasonal spatial correlation between MAOD and Ice (1 ° x 1 ° latitude-longitude resolution). The contour line corresponds to the ice edge, defined as the point in which the depolarization ratio equals 0.65. Southern hemisphere seasons from June 2006 to December 2018 are defined as winter: June 1st to September 1st, spring: September 1st to December 1st, summer: December 1st to March 1st, fall: March 1st to June 1st.

expansion of summertime MAOD and exhibited in values south of 66 °S (Figure 1.3.). From winter to spring, the negative relationship between MAOD and ice has increased in magnitude with values ranging from –0.8 to –0.2 and has moved southward from 90 ºW to 72 ºW and north along the coastline from 72 ºW to 67 ºW (Figure 1.6.). These dynamics occur alongside a negative correlation between ice and chl-*a* in the same spatial region south of 62 ºS, indicating an increase in MAOD, continued sea ice melt, and coincident seasonal phytoplankton bloom (Figures 1.6., 1.7.). Regional fluctuations in MAOD also occur. From winter to spring, a pulse is exhibited near the coastline north of 66 °S in the same area as the phytoplankton bloom and melt

in ice (Figures 1.3., 1.4., & 1.5.). As such, we hypothesize that this springtime pulse in MAOD is caused by biogenic aerosol formation.

We also examine the spatial correlation between ice and chl-*a* in context of MAOD and biogenic aerosol presence (Figure 1.7.). In springtime, a negative correlation between ice and chl-*a* is exhibited north of the ice edge stretching towards the coastline, with values ranging from –0.6 to –0.2 (Figure 1.7.), indicating the coincident seasonal increases in chl-*a* alongside ice melt. A winter to spring polynya also persists west of 81 ºW and north of 68 ºS, with a lack of

total freezing occurring in winter and melt occurring in spring, as visualized in Figure 1.5. and

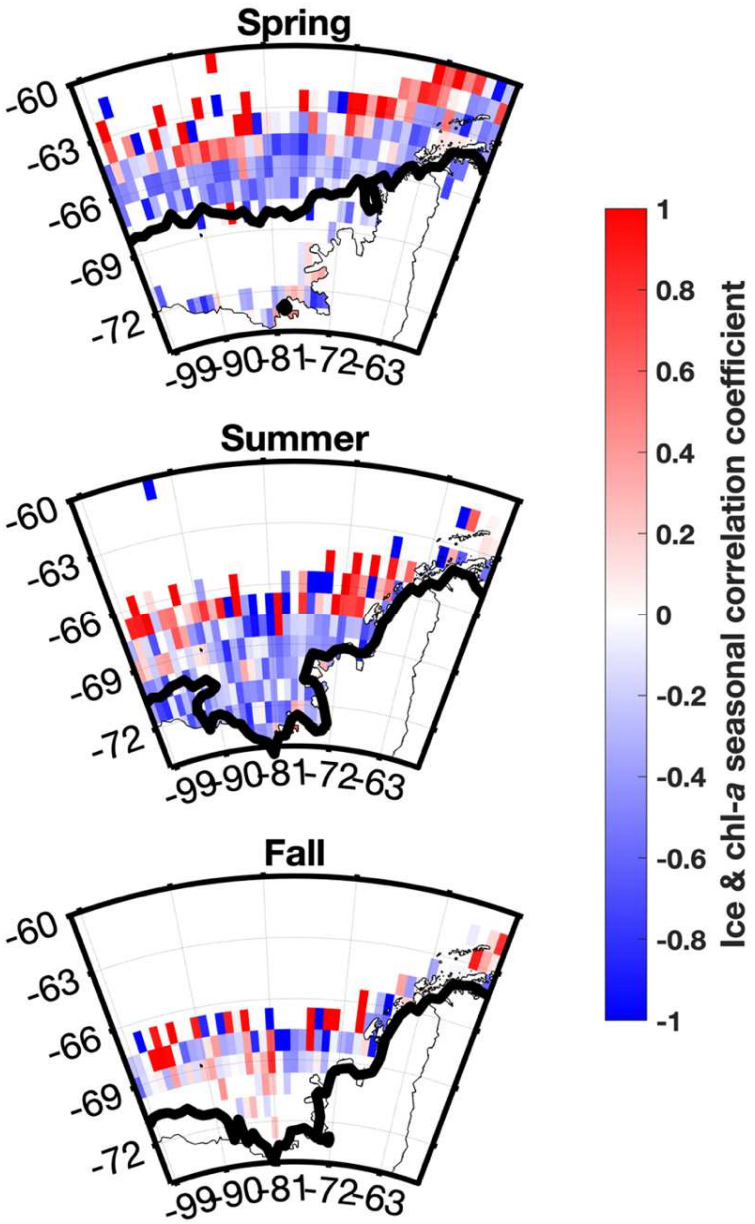

Figure 1.7. Seasonal spatial correlation (1 ° x 1 ° latitude-longitude) between ice and chl-*a*. The contour line corresponds to the ice edge, defined as the point in which the depolarization ratio equals 0.65. Southern hemisphere seasons are defined as winter: June 1st to September 1st, spring: September 1st to December 1st, summer: December 1st to March 1st, fall: March 1st to June 1st.

supported by previous work (Y. Li, Ji, Jenouvrier, Jin, & Stroeve, 2016; Turner, Maksym, Phillips, Marshall, & Meredith, 2013). A phytoplankton bloom also occurs in springtime west of 81 ºW (Figure 1.4.), and a negative correlation between ice and chl-*a* of –0.4 to –0.6 is present (Figure 1.7.).

In summertime, the negative correlation between ice and chl-*a* appears to decrease in magnitude while spreading southward, approaching the coastline (Figure 1.7.). However, the summertime correlation between MAOD and ice cannot be readily characterized due to the paucity of MAOD samples during this season (Figure 1.6. & S2, further discussed in Section 4.3.3). The negative fall correlation between MAOD and ice decreases in magnitude in comparison to springtime but persists with less noise south of 66 ºS near the peninsula (Figure 1.6.). Annual variability exists in fall ice dynamics, with certain years exhibiting a melt that proceeds until a winter freeze, and other years showing a general freezing until maximum extent in winter. This is also illustrated in the monthly climatology (Figure S1.5), in which ice from March to May is not highly variable, indicating fluctuations present in the multi-year time-series (Figures 1.1.a). Furthermore, the fall spatial correlation between ice and chl-*a* is largely dominated by noise, indicating the varied trends of ice formation and chl-*a* increase (Figure 1.7.).

4. Discussion

4.1. Temporal Trends: MAOD, chl-*a*, ice, and wind speed

Tropospheric marine aerosol species contributing to the observed seasonal cycles of MAOD in the Bellingshausen Sea are likely composed of diverse aerosol species. These include sea spray/salt, and biogenic aerosol species including non-sea-salt (NSS) sulphate aerosol, nitrate, water-soluble organic carbon, and MSA derived from DMS (Brechtel et al., 1998;

Cavalli, 2004; Rathke et al., 2002). Assessing seasonal cycles of MAOD is important as these aerosol species have the capacity to affect the regional climate of remote environments, either directly through absorption and scattering of solar radiation, or indirectly by acting as CCN, thereby influencing cloud dynamics, including albedo and lifetime (Coakley et al., 1983; Gabric et al., 2018; McCoy et al., 2015). Seasonal cycles of aerosol particle formation can increase the albedo of marine environments, thereby reducing the amount of short wave radiation that reaches the troposphere and causing cooling of the Earth's surface (Charlson, Lovelock, Andreae, & Warren, 1987). In contrast to lower latitude environments, the Bellingshausen Sea is also removed from aerosol sources linked to anthropogenic influences, and the WAP region is also remote from continental sources of mineral dust (Gabric et al., 2005; Gao, 2003). A study by Li et al. (2010) examined the transport of Patagonian dust to west Antarctica using CALIOP measurements. They surmised that only a small fraction of air masses from Patagonia are capable of transporting dust to west Antarctica, with a large fraction of continental dust likely removed before reaching the peninsula as well as transported outside of our study region by eastward transport from the westerlies (F. Li et al., 2010). As such, we do not attribute the seasonal variability of MAOD to continental-derived mineral dust nor to anthropogenic sources. Our observed temporality of MAOD values reflect past observed seasonal variability of AOD in this region. In a zonal analysis of AOD in the Southern Ocean using NASA SeaWiFS at 856 nm, Gabric et al. (2005) found summertime AOD maxima and minima from 60 ºS to 65 ºS and 65 ºS to 70 ºS ranging from 0.1 to 0.12 and 0.07 to 0.08, respectively. Those authors observed the seasonality of AOD across distinct zonal bands and sectors of the Southern Ocean and correlated AOD with sea ice and chl-*a*, finding strong synchrony. A later study by Gabric et al., (2018) similarly examined AOD in the Arctic and observed that peaks in AOD occur alongside melt of

sea ice and increases in annual primary productivity and biomass. They attributed seasonal AOD to a biogenic source of aerosols across both studies. Although it is not possible to directly compare magnitudes of AOD used in the Gabric et al. (2005, 2018) studies against MAOD due to wavelength differences between CALIPSO (532 nm) and SeaWiFS (856 nm), seasonal dynamics of MAOD reported in this work agree with these prior investigations. This supports our hypotheses of a contribution of biogenic aerosols to the seasonal MAOD signal.

4.2. Lagged Correlations between MAOD, chl-*a*, ice, and wind speed

The decoupling of chl-*a* and MAOD – with the timing of MAOD preceding or coincident with the maximum in chl-*a* – supports the hypothesis that phytoplankton bloom periods are associated with the release of biogenic sulfur species and contribute to aerosol concentration (Figure 1.2.). Previous work by Rinaldi et al. (2013) investigated whether model fits or satellite ocean color fields best predicted the chemical composition of submicron sea spray aerosol measured at the Mace Head Atmospheric Research Station, Ireland. They identified chl-*a* as the best biological surrogate for predicting the organic enrichment of sea spray aerosol. The correlation between these variables peaked with a time lag of 8 days, with chl-*a* preceding the enrichment of sea spray aerosol. In our study the reverse is true, and MAOD reaches a maximum one month before the maximum in chl-*a.* This is also observed in a study by Gabric et al. (2005) in which the maxima in satellite-derived AOD precedes maxima in chl-*a* with increasing latitudes, and at 60 °S to 65 °S the correlation between AOD and chl-*a* is at the greatest magnitude when out of phase. Those authors suggested that in these high latitude environments, the observed satellite retrievals of AOD are likely instead related to a sea-ice biogenic sulfur source in contrast to being solely derived from phytoplankton activity. As such, while we do

attribute increases in biological activity to the presence of organic matter enrichment and biogenic aerosol production observed as MAOD in our study, in this polar environment we nevertheless must note the importance of the concomitant influence of melt of sea ice and associated release of sulfur-based aerosol precursors further seeding the growth of biogenic aerosol. Our observations support prior trends observed in Gabric et al. (2005) and emphasize that the region of the planet is vitally important when examining dynamics between biology and biogenic aerosol formation.

We observe seasonal dynamics of MAOD increase as melt of sea ice occurs (Figure 1.2.). Similar trends are also exhibited by Gabric et al. (2005) who observed that the timing of the earlier peak in AOD agrees with the proposed hypothesis of sea-ice melt contributing to the release of biogenic sulfur aerosol species, thereby increasing AOD measurements. Numerous field campaigns have found statistically significant increases in aerosols, DMS, and dimethylsulfoniopropionate (DMSP) associated with the melt of sea ice (Chen et al., 2012; Stefels et al., 2007; Trevena & Jones, 2006). For example, in the east Antarctic, Trevana & Jones (2006) found that DMS in sea ice ranges from < 0.3 to 75 nM with greatest concentrations in upper ice that melts quickly at the onset of spring to summer leading to venting of DMS into the lower atmosphere. Prior studies by Zemmelink et al. (2008) have also found DMS concentrations of up to 6000 nmol m^{-3} (6 nM) in multi-year ice in the western Weddell Sea in the first weeks of December which sharply declined in concentration as summer progressed, with mean flux of DMS equaling 11 μmol DMS m^{-2} per day. Trevana & Jones (2012) further emphasize that three distinct time periods of DMS emission occur in polar regions: first, the degassing of DMS from sea ice in late spring; second, the melting of sea ice in summertime; and third, the increased biological productivity in ice-free coastal waters in late summer. These prior studies support our

observations on the seasonality of MAOD coupled to the melting of sea ice and support our hypothesis on the release and formation of biogenic aerosol from sulfur-based precursors.

As mean wind speeds are relatively high year-round in the Southern Ocean, with a maximum occurring in winter to spring (June to October) (Figure 1.1.d), prior studies have posited wind speed as a constant source of a background aerosol signature rather than a driver of observed seasonal aerosol trends (Gabric et al., 2005). Past work has noted the increase in sea salt aerosol associated with increasing wind speeds: Prijith et al. (2014) noted the linear relationship between wind speed and sea salt aerosol production, with bottom layer AOD observed to increase alongside an increase in wind speed, and Grythe et al. (2014) have noted a power law dependence with sea salt aerosol production proportional to windspeed by about the power of 3.5. If wind speed was thus the sole driver of seasonal MAOD trends, we would expect an immediate response in the MAOD increase caused by pulses in wind speed, which is not observed in our study. As such, we do not attribute the seasonal variability and summertime maxima in MAOD observed in Figure 1.1.a to the production of sea salt aerosol from winds. The seasonal late spring and summer increase in MAOD to summertime maxima likely indicates the presence of biogenic aerosol formation from sea ice melt and phytoplankton production (Trevana & Jones 2006; 2012).

Interestingly, as observed from the time-series, multiple years exhibit an initial pulse in MAOD from June to September before the later maxima. This could be tied the initial degassing of DMS from breaks in sea ice during springtime as indicated in Gabric et al., 2005. The breakup of sea ice is a known source of increasing DMS concentrations (Leck, Tjernström, Matrai, Swietlicki, & Bigg, 2004; Shepson, Matrai, Barrie, & Bottenheim, 2003), and springtime pulses are also indicated in ice core publications of MSA resulting from the oxidation of DMS (Curran

et al., 2003). One field study even noted measured DMS concentrations increasing while transecting and breaking through ice in the Southern Ocean seasonal ice zone (Koga et al., 2014). As the presence of MSA within ice cores is solely linked to biological activity and production of DMS in the Southern Ocean, these studies lend evidence to a possible biological signature in the springtime peak in MAOD resulting from breaks in ice that occur before the main summertime maxima associated with peak biological activity and sea ice melt (Curran, van Ommen, Morgan, Phillips, & Palmer, 2003; E. R. Thomas & Abram, 2016). Another possibility is that this initial pulse is instead tied to the maxima in wind speed (June to October) as observed in Figures 1.1.a and 1d, thereby tied to an aerosol signal dominated by wind-driven sea salt aerosol production before the summertime maxima takes place. With the lengthening of the summer ice-free season, an increase in open water, and strengthening of northerly winds, some studies have suggested that an increase in wind-induced sea spray may occur (Browse et al., 2014). This has the potential to increase MAOD tied to the strengthening of wind stress over the surface ocean. Regardless of whether this springtime peak is related to biological or physical processes, prior studies have not observed these trends from optical depth measurements due to the lack of passive sensor retrievals in early spring at high latitudes (Gabric et al., 2005, 2018). The possible link between wind speed and sea spray/salt will need to be investigated in future work.

4.3. Spatial Trends and Correlations between MAOD & ice and ice & chl-*a*

Past field work in the WAP examined a seasonal summertime phytoplankton bloom with significant levels of DMSP present within algal cells (Gabric et al., 2005; Thomas, 2002; Webb et al., 2019). Different species of ice algae contain varying quantities of DMSP, and in times of biological productivity, the transformation of DMSP to DMS may occur when the algal cell is

grazed or when viral lysis occurs. The total Antarctic seasonal ice zone is predicted to contain as much as 9 Gmol S as DMSP, and with seasonal melting, ice-algae can be released into the surrounding water, initiating ice-edge phytoplankton blooms (Trevena et al., 2003). The sea-air flux of DMS to the overlying atmosphere may then cause the formation of biogenic aerosol (Ducklow et al., 2013; Gabric et al., 2005). Therefore, we examined spatial correlations between MAOD, chl-*a*, ice, and wind speed to ascertain whether distinct zones recurrent across seasons could be observed (Figures 1.6., 1.7., S7, & S8). We compared these relationships against null models of randomized data (Figures S1.9 to S1.12), and observed that significant spatial clustering occurs in the signal between MAOD & ice and ice & chl-*a.* This provides compelling evidence to the suggestion that melt of sea-ice and associated seasonal phytoplankton blooms are linked with the release of biogenic sulfur species thereby contributing to aerosol presence (Table S1.1). We describe these trends spatially across seasons below.

In wintertime, we attribute the cause of enhanced MAOD in spatial pixels north of 66 °S to that of sea salt/spray from wind speed versus that linked to biological activity and/or melt of ice (Figure 1.3.). In these same spatial regions, a seasonal enhancement of wind stress persists as visualized in the spatial climatology of wind speed (Figure S1.6) and observed in spatial correlations between MAOD and wind speed, with correlation coefficients ranging from –0.4 to 0.6 (Figure S1.8). South of 66 °S, the Bellingshausen Sea is predominantly ice covered (Figure 1.5.). In this region, frost flowers, highly saline ice crystals that rapidly form on fresh sea ice, may occur. These ice crystals are posited to be a source of aerosol precursors and sea salt aerosol through wind action breaking and lofting of ice crystal fragments (Perovich & Richter-Menge, 1994; Xu, Russell, & Burrows, 2016). Future work must focus more carefully on the drivers of enhanced aerosol formation in the wintertime Bellingshausen Sea region. These studies are

particularly elusive since studies using passive remote sensing measurements such as AOD lack wintertime reporting in this region (Gabric et al., 2005, 2018).

The springtime northwestward bloom is further away from coastlines and corresponds spatially to where ice begins to melt at 69 °S to 66 °S and 90 °S to 72 °S (Figures 1.4., 1.5.). These observations are also supported by prior studies and suggest that chl-*a* increases in the marginal ice zone alongside melting (Gabric et al., 2018; Schofield et al., 2017; Trevana & Jones, 2006). The springtime increase is likely dominated by ice algae, known to be released into the surrounding water column alongside seasonal ice melt, triggering under-ice or ice-edge phytoplankton blooms (Bowman et al., 2018; Gabric et al., 2005; Galindo et al., 2014; Leeuwe et al., 2020, Trevana & Jones, 2006). The coincident seasonal increases in chl-*a* alongside sea ice melt are supported by field evidence of spring to summer phytoplankton bloom periods (Ducklow et al., 2013; Schofield et al., 2017). In contrast to negative correlations between ice and chl-*a,* the high positive correlations in spring are particularly interesting as the increase in chl-*a* starts along the ice edge, likely indicating a phytoplankton bloom alongside the marginal ice zone (e.g., as seen in Lu et al. (2020)). In spring to summer, phytoplankton bloom sites are associated with areas of rapidly melting sea ice, due to the incubation of phytoplankton species beneath sea ice alongside increasing seasonal solar irradiation and release of nutrients from surrounding sea-ice melt. As these phytoplankton blooms increase DMS concentration, regions of rapid ice melt and coincident phytoplankton blooms can become areas of significant DMS emission. Prior work supports these findings, with observations of phytoplankton bloom sites within polynyas in the East Antarctic and associated emission of atmospheric sulfur species (Zhang et al., 2015). Melting can trigger active microalgal release of DMS and DMSP, and the sudden increase in light intensity when cells exit the ice pack may also trigger a rapid DMSP

release (Delille et al., 2007; Galindo et al., 2016). Our observations of springtime trends support the possible links between seasonal phytoplankton blooms and melt of ice and underscore the importance of these seasonal trends on the release of aerosol precursors and formation of biogenic aerosol (Becagli et al., 2016; Jarníková & Tortell, 2016).

In the summertime, the spatial climatology of MAOD (Figure 1.3.) exhibits a southward expansion of MAOD that corresponds to the same spatial regions as the continued melt of ice and increase in chl-*a* (Figures 1.4., 1.5.), suggesting a seasonal MAOD signal tied to sea ice melt and biogenic aerosol presence. In contrast to the wintertime MAOD climatology, the increase in MAOD north of 66 °S is not tied to wind speed, which exhibits the lowest magnitude across the study range in the summer. This increase in MAOD is likely instead linked to the sea ice melt and associated chl-*a* increase (Figures 1.6., 1.7.). The annual summertime enhancement of MAOD observed in Figures 1.1.a, S1.5, & 1.3. is supported by prior *in situ* studies from McMurdo Station in the Ross Sea region of Antarctica. In a study by Liu et al. (2018), the ARM West Antarctic Radiation Experiment (AWARE) campaign observed organic matter enrichment of aerosol 150 times greater with summer organic matter equaling 0.27 $\mu g\ m^{-3}$ in contrast to wintertime organic matter enrichment at 0.04 $\mu g\ m^{-3}$. As the Ross Sea has a high primary production rate in the summertime (Kevin R. Arrigo, van Dijken, & Bushinsky, 2008), and as prior studies have also attributed aerosol formation to seabird emissions with particles containing CHN and CHNO fragments linked to uric acid and nitrogen-containing components from penguin guano (Schmale et al., 2013; Weber et al., 1998), the authors attribute the elevated organic matter observed in summertime to increased biological activity and seabird emissions of nitrogen-containing compounds seeding growth of aerosol particles (J. Liu et al., 2018). Thus,

our hypotheses of the source of elevated summertime MAOD as caused by biological activity is supported by both field studies and prior remote sensing analyses.

In examining summertime spatial correlations (Figures 1.6., 1.7.), a lack of strong correlations between MAOD, increases in chl-*a*, and decreases in ice, which are implied by their respective seasonal climatologies, is present. In contrast to observing the summertime MAOD climatology (Figure 1.3.) in which all profiles within each pixel are averaged, a limited number of MAOD profiles occur across each annual summer within each spatial pixel (Figure S1.2). As only nighttime and cloud-free profiles were used in calculating MAOD, the summertime spatial relationship between MAOD, ice, and chl-*a* is less established than in spring and fall due to the fewer number of profiles available when computing spatial correlations. The relationship between MAOD, chl-*a*, and ice is nevertheless visualized across spring and fall coincident with regional ice dynamics and phytoplankton bloom periods (Section 4.3.2 & 4.3.4) and is explored temporally (Section 4.2). As such, we nevertheless attribute seasonal cycles of MAOD maxima to the seasonal cycles of melt of ice and increases in biological productivity.

The decrease in magnitude and southward extent of MAOD from summer to fall (Figure 1.3.) is likely tied to the diminishment of phytoplankton productivity (Figures 1.1.b, 1.4.), thus limiting the formation and emission of biogenic aerosol. Fall trends can be varied as visualized in spatial climatologies (Figures 1.6.,1.7.). As ice formation takes place with certain areas freezing before maximum extent in winter and with the formation of polynyas, phytoplankton blooms can be further triggered, thereby increasing DMS emissions (Zhang et al., 2015). In particular, regions of open water within sea ice, such as polynyas, can have a large impact on the local atmospheric DMS load (Tortell et al., 2012; Zhang et al., 2015). In the fall in Arctic shelf regions, direct emissions of aerosol precursors have been tied to the formation of sea ice and

frost flowers (Xu et al., 2016). As the negative correlation between MAOD and ice is low in magnitude in some regions in the fall (Figure 1.6.), it is not possible to dismiss the role of ice formation in direct emission of aerosol (Ardyna et al., 2014; Kaleschke, 2004).

5. Conclusions

This study presents a satellite remote sensing analysis of seasonal trends in marine tropospheric aerosol arising from the interplay between physical and biological processes in the polar sea ice habitat of the Bellingshausen Sea. We examined seasonal variability of marine aerosol optical depth (MAOD) alongside fluctuations in chlorophyll-*a* (chl-*a*) concentration and sea ice dynamics. A seasonal increase in MAOD was observed across temporal scales alongside a seasonal increase in chl-*a* and across spatial and temporal scales alongside a melt in sea ice. To the best of our knowledge, this study is also the first to further distinguish a late winter to early spring temporal MAOD signal, likely tied to an aerosol source from either venting of biogenic aerosol from breaks in sea ice or to sea spray/salt aerosol resulting from pulses in wind speed. This pulse in MAOD occurs before the formation of biogenic aerosol predicted in the summertime maxima and main peak of MAOD. This works supports previous studies that have found similar trends in aerosol optical depth (AOD) in the Arctic and Antarctic (Gabric et al., 2005, 2018). The temporality and onset of the summertime maxima and main peak of MAOD indicate the central role of aerosol emission tied to biogenic sources, particularly pronounced as it occurs alongside the biologically productive spring-summer season and release of sulfur species associated with sea ice melt. Future work is needed to identify a MAOD signal distinctly tied to organic aerosols across spatiotemporal scales, particularly in high-latitude summertime, as

the MAOD signal is limited and obscured by noise from ambient sunlit conditions that adversely affect data retrieval from the lidar.

Acknowledgments

Chapter 1, in full, is a reprint of the material as it appears in Journal of Geophysical Research: Atmospheres 2021. Dasarathy, Srishti; Kar, Jayanta; Tackett, Jason; Rodier, Sharon D.; Lu, Xiaomei; Vaughan, Mark; Toth, Travis D.; Trepte, Charles; Bowman, Jeff S.; 2021. DOI: 10.1029/2021JD034737. The dissertation author was the primary investigator and author of this paper. Graduate student peers Kelley McBride and Dr. Kara Voss provided insight in accessing and processing of the CALIOP dataset. Dr. Nicole Couto likewise aided in mapping techniques. This work was supported by NSF-OPP 1846837, NSF-OPP 1821911, and a Simons Foundation Early Career Marine Microbial Investigator Award. This work was further supported by the NASA Internship Program at the Langley Research Center.

Data Availability Statement

CALIPSO data were obtained from the NASA Langley Research Center Atmospheric Science Data Center, available at https://doi/org/10.5067/CALIOP/CALIPSO/LID_L2_05KMAPRO-STANDARD-V4-20. AMSR data are produced by Remote Sensing Systems and were sponsored by the NASA AMSR-E Science Team and the NASA Earth Science MEaSUREs Program. Data are available at www.remss.com. Chl-*a* concentrations were obtained from Level 3 (4 x 4 km^2) monthly mapped data products from the Ocean Data Archive (https://oceandata.sci.gsfc.nasa.gov/MODIS-Aqua/Mapped/Monthly/4km/chlor_a/). The authors

would like to thank the NASA/GSFC MODAPS Services website for the MODIS L3 mapped data. (NASA Ocean Biology Processing Group, 2017). All coding scripts for calculation and plotting of these data can be downloaded from GitHub at https://github.com/srdasara/Multiyear_SeasonalTrends_BellingshausenSea.

CHAPTER 2: WIND-DRIVEN AND SEASONAL EFFECTS ON MARINE AEROSOL PRODUCTION IN THE BELLINGSHAUSEN SEA, ANTARCTICA

1. Introduction

The production of marine tropospheric aerosol in the Bellingshausen Sea of the western Antarctic Peninsula (WAP) is coupled to environmental variability. Distant from most continental sources of anthropogenic pollution and mineral dust, variability in the sources of marine aerosol in this polar sea ice environment is largely driven by the ocean itself. The Bellingshausen Sea is thus a relatively pristine environment to study the impact of primary and secondary sources as drivers of marine tropospheric aerosol. Primary sources contribute to the mechanical production of marine aerosol, most notably wind-driven sea spray aerosol (SSA) (O'Dowd & de Leeuw, 2007). Sea surface temperature (SST) also contributes to SSA production across a wide range of wind speeds, and prior field observations have observed that SST enhances the SSA when wind exceeds 5 m s^{-1} (S. Liu et al., 2021). Secondary sources are also contributed by the oxidation of precursor compounds (Kroll & Seinfeld, 2008; Lewis & Schwartz, 2004). As such, aerosol production is influenced by physical and biological processes including wind stress, SST, water column stability, sea ice melt, and the timing and magnitude of phytoplankton blooms (Figure 2.1.) (Ardyna et al., 2014; Tremblay & Gagnon, 2009).

Prior studies have observed variation in the timing and magnitudes of marine aerosol production in relation to environmental drivers, with studies in high-latitude environments supporting a biogenic component of marine aerosol observations due to the coincident timing of seasonal sea ice melt and phytoplankton production. These processes can foster wind-driven SSA, the formation of primary organic aerosol, and the growth of sea spray from volatile organic compounds (Becagli et al., 2016; Brooks & Thornton, 2018; Leck & Bigg, 2005; Liss et al.,

2000; Orellana et al., 2011; Stefels et al., 2007; Trevena & Jones, 2006). In contrast, other studies emphasize the anticorrelation between biological activity and marine aerosol production with suppression of SSA production in relation to seasonal biological activity through processes affecting the sea surface microlayer (Dror et al., 2018; Fuentes et al., 2010; Modini et al., 2013; K. Sellegri et al., 2006). Disparate findings across these studies underscore the broad uncertainty in the degree of biological and physical influence on marine aerosol production across ocean basins.

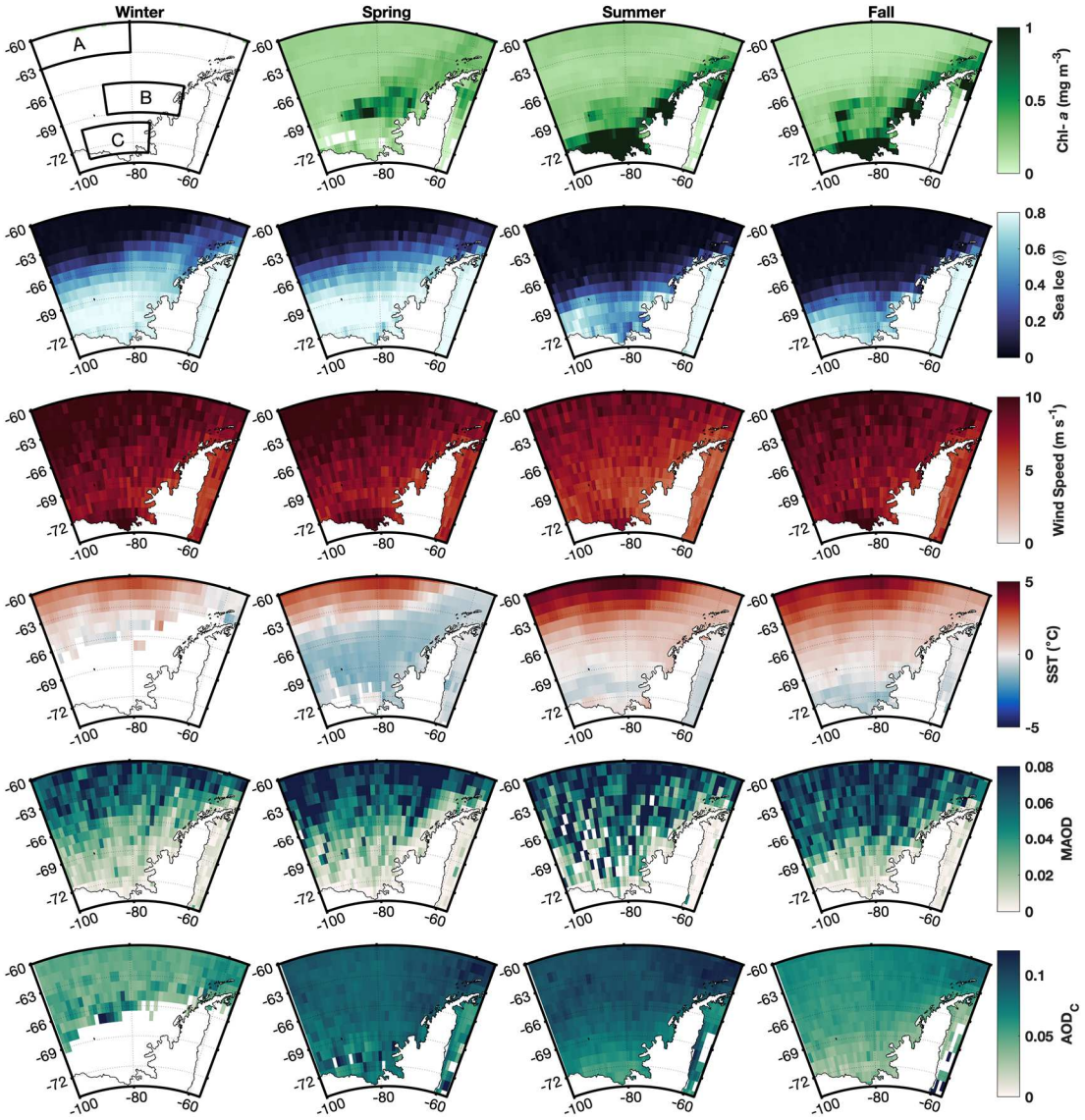

Figure 2.1. Seasonal climatologies of chl-*a*, sea ice, wind speed, SST, MAOD, and AOD_C. These data were obtained from January 2007 to December 2018 (with the exception of SST obtained from January 2013 to December 2018) across 100°W–54°W and 60°S–75°S. Missing data is present in winter for chl-*a* due to solar nighttime. This subplot is instead used to depict regions of interest used in further statistical analysis (for more information, see Figure S2.1). For sea ice, values less than 0.15 indicate water presence, 0.15 to 0.65 indicate a mix between water and ice presence, and values greater than 0.65 indicate ice presence (Lu et al., 2017). Southern hemisphere seasons are defined as winter: June 1–September 1, spring: September 1–December 1, summer: December 1–March 1, fall: March 1–June 1.

There is an overall agreement that biological and physical dynamics are likely to affect marine aerosol production, and multiple studies have quantified the SSA response to changes in wind speed, SST, and phytoplankton abundance (Dror et al., 2018; Fuentes et al., 2010; S. Liu et al., 2021; Modini et al., 2013; K. Sellegri et al., 2006). One study found that time scales of observation were important in assessing the link between coarse-mode Aerosol Optical Depth (AOD_C) and wind speed in the tropical South Pacific gyre. Those authors found that AOD_C and wind speed were positively correlated on both daily and interannual time scales but were anticorrelated on the seasonal time scale (Dror et al., 2018). They further surmised that this significant anticorrelation was due to the suppression of SSA during increased chlorophyll–*a* concentrations (chl-*a*) and associated high surfactant concentrations in the sea surface microlayer (Dror et al., 2018; Modini et al., 2013). Contrasting this study, analyses of time-lagged data binned by month in several high-latitude studies show that Marine Aerosol Optical Depth (MAOD) (Dasarathy et al., 2021) and AOD increased alongside seasonal increases in chl-*a* and sea ice melt (Gabric et al., 2005, 2018) . Those authors attributed a biological component of marine aerosol contributing to fluctuations in seasonal magnitudes of AOD. However, these studies use different methods than Dror et al. (2018), and, in contrast to the South Pacific gyre study, high-latitude studies have not yet assessed AOD_C dynamics in relation to environmental parameters.

In this study we examined the scale-dependent effects of oceanic factors on marine aerosol production using satellite observations over the Bellingshausen Sea. As in Dror et al. (2018), we retrieved AOD_C from the Moderate Resolution Imaging Spectroradiometer (MODIS) Aqua. Using methods previously developed in Dasarathy et al. (2021), we further examined MAOD, retrieved from the Cloud-Aerosol Lidar with Orthogonal Polarization (CALIOP)

onboard the Cloud-Aerosol Lidar and Infrared Pathfinder Satellite Observation (CALIPSO). AOD_C is a measure of the coarse mode of aerosol particles (those with radii >1 μm) (Fitzgerald, 1991; Kleefeld, 2002; Karine Sellegri, Gourdeau, Putaud, & Despiau, 2001). SSA dominates the mass concentration of marine aerosol in remote oceanic regions, with the coarse mode of aerosol composed mainly of SSA. As SSA accounts for the vast majority of supermicron aerosol in remote oceanic regions (de Leeuw et al., 2011; Fitzgerald, 1991), AOD_C is a good proxy for SSA in the remote Bellingshausen Sea atmosphere. Nevertheless, passive sensor retrievals have limitations, and in high-latitude environments these include the full omission of wintertime data due to lack of nighttime retrievals. To address these challenges, previously we developed a novel method of quantifying low-lying aerosols (Dasarathy et al., 2021). MAOD—retrieved in high-latitude winter despite lack of solar radiation—is used alongside AOD_C to characterize these aerosols (For more information, see Appendix Chapter 2 Section S1). Because MAOD enables retrievals of lower altitude marine aerosol particles with radii > ~100 nm (Tackett, 2009), our use of both MAOD and AOD_C accomplished distinct, complementary tasks. This high sensitivity to submicron aerosol, alongside the ability to limit optical depth retrievals to the marine boundary layer, provided a distinct advantage in examining trends when the aerosol source is the ocean itself. In contrast, AOD_C by definition retrieves aerosol particles with radii > 1 μm, thereby restricting observations of trends of marine aerosol in remote regions as in the Bellingshausen Sea to SSA, and possibly obscuring the observation of trends of biogenics such as non-sea salt (NSS) sulfate aerosol and methanesulfonic acid (MSA) from oxidation of dimethyl sulfide (DMS) as well as water-soluble organic carbon (Brechtel et al., 1998; Cavalli, 2004; Rathke et al., 2002). Nevertheless, as a passive sensor measurement, AOD_C corresponds to daytime

retrievals, and in high-latitude regions such as the Bellingshausen Sea, use of AOD_C provided exceptional coverage of marine aerosol in summertime.

A prior study in the pristine South Pacific gyre indicated the significance of both daily and annual links between AOD_C and wind speed as well as the importance of the suppression of AOD_C in relation to high chl-*a* (Dror et al., 2018). Those authors attributed, to first order, variations in AOD_C to variations in wind, but they found that summertime blooms masked the wind speed dependence (Dror et al., 2018). We considered whether the high-latitude coastal region of the Bellingshausen Sea would show MAOD and AOD_C suppression due to stronger biological seasonality as supported by prior studies (Dasarathy et al., 2021; Gabric et al., 2005, 2018). We used AOD_C, a proxy for aerosol particles with radii > 1 μm (most notably SSA in remote marine environments), as well as MAOD, a proxy for lower altitude marine aerosol particles with radii > 100 nm to answer the following: (i) Do MAOD and AOD_C correlate to wind speed across time scales in the Bellingshausen Sea region? (ii) Across open ocean and coastal regions, are MAOD and AOD_C suppressed during periods of high wind speed and high biological activity in contrast to periods of low biological activity?

2. Data Sources and Methods

All satellite data were obtained from January 2007 to December 2018 across 100 °W to 54 °W and 60 °S to 75 °S. Sea ice and MAOD retrievals were obtained from CALIOP onboard CALIPSO (Winker, 2018), AOD_C retrievals were obtained from the Collection 6.1 algorithm of MODIS aerosol products (Levy et al., 2013), chl-*a* and SST retrievals were obtained from MODIS Aqua (NASA Ocean Biology Processing Group, 2017), and surface wind speed

retrievals were obtained from the Advanced Microwave Scanning Radiometer for the Earth Observing System (AMSR-E & AMSR-2).

Three distinct regions (A, B, and C) were selected across a North-to-South gradient from capturing variations in wind speed, light availability, seasonal cycles of phytoplankton blooms, and the melt and refreeze of sea ice (Figures S2.1, 2.1., & 2.2.). Statistical analyses were carried out individually within these regions. Detailed methods for retrieving MAOD, AOD_C, AOD_T, AOD_f, chl-*a*, SST, depolarization ratio (ice), and wind speed are within S1. We also consider trends in total column AOD (AOD_T) and the fine-mode fraction of AOD (AOD_f) across daily, seasonal, and annual scales to determine dependence on wind speed across regions. Methods and results are reported in Appendix Chapter 2 Section S1 and visualized in Figures S2.5 to S2.9 and Tables S2.1 to S2.6.

Daily averaged time-series were constructed for MAOD, ice, and wind speed by averaging profile values across daily time steps throughout all regions (thin lines in Figure 2.2.). Darker solid lines represent smoothed values using a moving average filter of 30 days. Time-series for AOD_C and chl-*a* were constructed by temporally averaging these data across the same regions. Further information on statistical analyses is found in Appendix Chapter 2 Section S1.

3. Results

We examined the impact of varying environmental conditions on magnitudes of MAOD and AOD_C over three regions from open ocean to coastal (Regions A, B, & C, see Figure S2.1). Across the multi-year record from 2007 to 2018, daily means of AOD_C (thin lines in Figure 2.2.), are 0.0879 ± 0.0780, 0.0848 ± 0.0744, and 0.0680 ± 0.0422 for AOD_C across Regions A, B and C, respectively, and equal 0.0989 ± 0.0955, 0.0638 ± 0.0721, and 0.0461 ± 0.0545 for MAOD

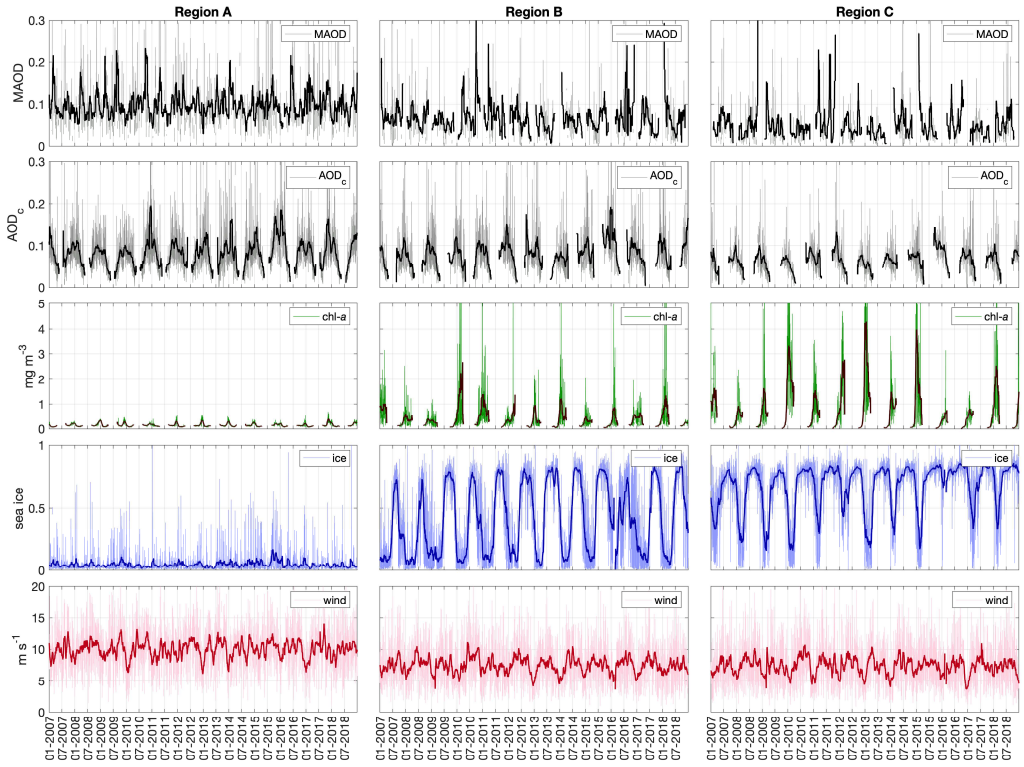

Figure 2.2.A, 2.2.B, & 2.2.C. Daily timeseries of MAOD, AOD_C, chl-*a*, sea ice presence, and wind speed. For sea ice, values less than 0.15 indicate water presence, 0.15 to 0.65 indicate a mix between water and ice presence, and values greater than 0.65 indicate ice presence (Lu et al., 2017). Darker shaded lines represent a 30-day moving average.

across the same. Large standard deviations indicate the high variability and spread of these data as well as the abrupt day-to-day changes of AOD_C and MAOD across all regions. The open ocean Region A had large differences in wind speed between summer and winter (Figures 2.1. & 2.2.). In contrast, Regions B and C exhibited large interannual variability in sea ice and blooms of phytoplankton observed as chl-*a*. These dynamics are visualized spatiotemporally in Figures 2.1. and 2.2.; as such, we used the open ocean Region A for further examining the dependence of marine aerosol production on diurnal wind speed. Across daily timescales, wind speed had a significant impact on increasing magnitudes of MAOD (nighttime winds) and AOD_C (daytime winds), indicating that SSA was likely a major constituent of MAOD and AOD_C driven by wind

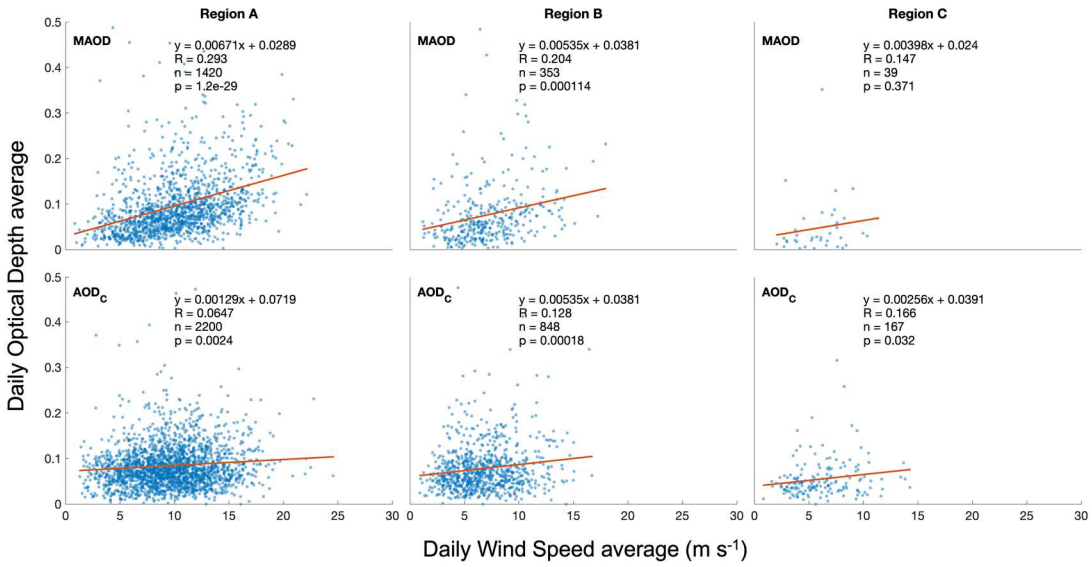

Figure 2.3.A, 2.3.B, & 2.3.C. Daily scatterplot assessing MAOD vs nighttime winds and AOD_C vs. daytime winds across all regions in open ocean (no sea ice) conditions.

action over the surface ocean (Figure 2.3., Table S2.4). When considering the daily variability of MAOD in relation to nighttime wind speed, we observed weak positive significant ($p < 0.05$) correlations in Regions A and B ($R > 0.2$: thresholds for defining "weak" are taken from Correlation and Regression: The BMJ., 2020). Correlation analyses for Region A had n = 1420 and n = 2200 overlapping points between MAOD, AOD_C and diurnal wind speed. In Region B, points overlapping were n = 343 and n = 858 for MAOD and AOD_C, respectively (Figure 2.3.). The lack of significance in Region C was perhaps due to the paucity of valid data points (n = 39) in this high-latitude region (Figure 2.3.C, Table S2.4). Similarly, very weak but significant correlations of AOD_C to wind speed emerged across all Regions (Figure 2.3., Table S2.4) alongside weak significant positive correlations to SST particularly in Region A (Figure S2.11). We also observed a significant–albeit small–link between AOD_C at high versus low wind speed conditions in the open ocean Region A (Figure S2.4). Significant differences occurred across

both MAOD and AOD_C with median values between high versus low wind speed differing by 0.034 for MAOD and 0.005 for AOD_C (Figure S2.4).

We further assessed the correlation between daily MAOD and AOD_C to daily wind speed in austral winter versus summer (Figure 2.4.). With a similar analysis to Dror et al. (2018), we found no seasonal differences in MAOD in the open ocean Region A (the positive, significant correlation of MAOD to nighttime winds was nearly identical), and some seasonal differences in Region B (a more positive significant correlation existed in the summer). For AOD_C, we found some seasonal differences in Region A (summer exhibited a more positive significant relationship to daytime winds), and some seasonal differences in Region B (all seasons had significant positive correlations). Notably, in contrast to the tropical Pacific in which enhanced biological activity suppressed SSA particle production (Dror et al., 2018), we did not observe any evidence of lessening or suppression of MAOD and AOD_C magnitudes during the biologically productive austral summertime (Figure 2.4., Table S2.4).

4. Discussion

This study constitutes the first examination of drivers of AOD_C across the Southern Ocean and builds upon prior observations of trends in MAOD that were discussed previously by Dasarathy et al. (2021). We examined whether MAOD and AOD_C have an SSA component and whether there is an influence of other environmental parameters on high-latitude marine aerosol production across an open ocean and two coastal regions (Figure S2.1). These regions captured the increased seasonality moving southwards and nearer to shore, with distinct impacts on the production of marine aerosol driven by primary and secondary processes (Dasarathy et al., 2021; Gabric et al., 2005, 2018). In the pristine South Pacific gyre, daily and annual correlations

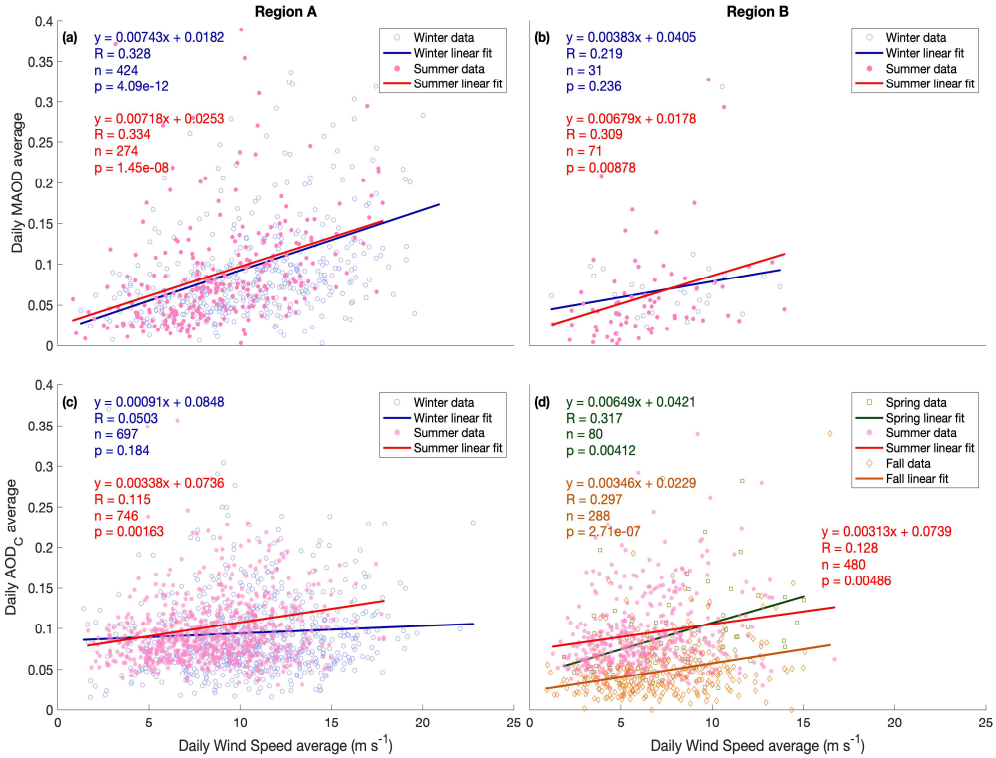

Figures 2.4.a & 2.4.b. Seasonal scatterplots of MAOD vs. nighttime wind speed, winter vs. summer. **Figures 2.4.c & 2.4.d.** Seasonal scatterplots of AOD_C vs. daytime wind speed. Region C is excluded due to insufficient data across seasons. **In Figure 2.4.d**, spring and fall are compared to summer due to lack of wintertime data. Seasons are defined as winter: June 1–September 1, spring: September 1–December 1, summer: December 1–March 1, fall: March 1–June 1.

showed links between AOD_C and wind speed as well as the suppression of AOD_C during seasonal phytoplankton blooms (Dror et al., 2018). We examined whether the Bellingshausen Sea, subject to high interannual variability in various environmental processes, showed similar trends or whether there instead exist regional differences that must be examined closely when ascertaining drivers of natural marine aerosol (also see Appendix Chapter Two Section S2 for a discussion of seasonal and annual correlations).

We discerned main characteristics of the dependence of MAOD and AOD_C on wind speed across timescales and across periods of variable biological activity across all regions

(Figures 2.3., 2.4., S2.4 to S2.8, S2.10, S2.11, and Tables S2.1 to S2.6). Interestingly, we observed that MAOD had stronger correlation to winds than AOD_C. Contrary to the expected robust correlation of AOD_C to wind speed due to its association with SSA, AOD_C had very weak magnitudes of correlation to wind speed across regions, even in the open ocean Region A. We suggest two possible theories:

First, we predict that SSA production in this region was modulated by SST. Prior in situ work found that SST impacts the production of water droplets by reducing the viscosity and ocean surface tension at higher temperatures, thus potentially enhancing the production of SSA (Jaeglé, Quinn, Bates, Alexander, & Lin, 2011; S. Liu et al., 2021; Saliba et al., 2019). Prior observations also found that, across ocean basins, higher SST enhances the production of SSA across a wide range of wind speed levels (S. Liu et al., 2021). In support of these findings, we observe that the open ocean Region A had weak significant correlations of SST to AOD_C (Figure S2.11). Second, weaker correlations of AOD_C to wind speed across regions may be due to AOD retrievals obscured by free troposphere aerosol layers aloft. Prior work by Thomas et al. (2022) indicated the presence of long-range transported aerosols in the free troposphere over the Southern Ocean consisting of continental aerosol species. This may have contributed to magnitudes of AOD in Region A, thus obscuring any dependence with wind speed. In contrast to AOD_C, the stronger dependence of MAOD on wind speed, particularly pronounced in the open ocean, may be due to differences in their derivation: MAOD is a low-altitude marine aerosol that includes smaller sized marine aerosol particles, whereas AOD_C constitutes a column-based retrieval selective for larger particles (Appendix Chapter 2 Section S1). Through our derivation of MAOD from quality-screened and subtyped extinction coefficient profiles, we directly evaluated the variability of aerosol in the marine boundary layer. Using MAOD, we observed a

low-altitude marine aerosol signature that was significantly driven by day-to-day changes in wind speed across all regions, indicating a likely SSA contribution to MAOD.

We further examined whether high biological productivity caused lower magnitudes of MAOD or AOD_C even at high wind speed. While suppression of SSA may still take place, SSA is unlikely to be the only component contributing to cycles of MAOD or AOD in marine environments. Numerous mechanisms may explain MAOD and AOD_C magnitudes in summertime. Prior studies have found that the Antarctic seasonal ice zone is predicted to contain as much as 9 Gmol S as dimethylsulfoniopropionate (DMSP), and with seasonal summertime melting, ice-algae are released into the surrounding water and initiate ice-edge phytoplankton blooms (Trevena, 2003). The sea-air flux of DMS to the overlying atmosphere may then cause the formation of biogenic aerosol. Prior studies have indicated bimodal distributions of biogenic aerosol from 50 nm up to 1 micron, including species such as NSS sulphate aerosol, nitrate, water-soluble organic carbon, and MSA derived from DMS; thus, MAOD is relevant for the analysis of biogenic aerosol distribution (see S1) (Barth, Rasch, Kiehl, Benkovitz, & Schwartz, 2000; Brechtel et al., 1998; Cavalli, 2004; Gabric et al., 2005; Lannuzel et al., 2020; J. Liu et al., 2018; Rathke et al., 2002; Stefels et al., 2007; Trevena & Jones, 2012).

Summertime enhancements of MAOD and AOD_C were also supported by prior in situ studies from McMurdo Station. Organic aerosol mass concentrations have been recorded at 150 times greater in summer than winter, with summer organic mass concentration equaling 0.27 μg m^{-3} in contrast to wintertime organic mass concentration at 0.04 μg m^{-3} (J. Liu et al., 2018). As the Ross Sea has high primary production rates in the summertime (Kevin R. Arrigo, van Dijken, & Pabi, 2008), and as prior studies have also attributed aerosol formation to seabird emissions with particles containing CHN and CHNO fragments linked to uric acid and nitrogen-containing

components from penguin guano (Schmale et al., 2013; Weber et al., 1998), the authors attributed the elevated organic mass concentration to increased biological activity and seabird emissions of nitrogen-containing compounds seeding growth of aerosol particles (J. Liu et al., 2018).

Non-biological drivers may also explain summertime enhancements MAOD and AOD_C. In polar regions, melt of sea ice and the associated increase in open ocean fraction may by itself increase wind-induced sea spray (Browse et al., 2014). Further, warmer SST may further enhance the production of SSA. Aircraft measurements have shown that predicting SSA using wind speed alone underestimates SSA in warm waters and overestimates SSA in cold waters, with the difference instead explained by SST (S. Liu et al., 2021). In contrast, prior work from the North Atlantic Aerosol and Marine Ecosystems Study (NAAMES) show that climate models relying solely on wind speed may overestimate SSA concentrations and underestimate SSA scattering if not also taking into account SST (Jaeglé et al., 2011; Saliba et al., 2019). Thus, sources of elevated summertime MAOD and AOD_C are varied, resulting in high-latitude polar regions from increases in open ocean, warmer summertime SST, or increases in biological activity. Importantly, we did not observe suppression of MAOD or AOD during periods of high biological activity even at high wind speeds.

5. Conclusions

Our objective was to examine whether the high-latitude coastal region of the Bellingshausen Sea showed MAOD and AOD_C suppression due to stronger biological seasonality. We examined three regions that ranged from open ocean to coastal across daily, seasonal, and annual timescales and assessed whether wind speed drove trends in marine aerosol

and whether suppression of MAOD and AOD_C occurred during high biological activity. Similar to the pristine South Pacific gyre, daily wind speed was significantly correlated with increasing MAOD and AOD_C indicating likely SSA, further supported by correlations of AOD_C to warmer SST in the open ocean. We further found that MAOD and AOD_C increased or remained constant with wind speed during the biologically productive austral summer, supporting biological enhancement rather than suppression of MAOD and AOD_C magnitudes in summer. Our study illustrates the complexity of the underlying environmental processes that drive marine aerosol, making it necessary to determine regional differences across the world's ocean basins.

Acknowledgements

Chapter 2, in full, is a reprint of the material as it appears in Geophysical Research Letters 2023. Dasarathy, Srishti; Russell, Lynn M.; Rodier, Sharon D.; Bowman, Jeff S.; 2023. DOI: 10.1029/2022GL099723. The dissertation author was the primary investigator and author. This research was supported by NSF-OPP 1846837 and the Climate and Environmental Sciences Division of the U.S. Department of Energy under Contract DE-SC0021045. Initial phases of this work were supported by the NASA Internship Program at the Langley Research Center.

Data Availability Statement

CALIPSO data were at https://doi.org/10.5067/CALIOP/CALIPSO/LID_L2_05KMAPRO-STANDARD-V4-20 . MODIS data were obtained at https://ladsweb.modaps.eosdis.nasa.gov/search/ under the MYD08_D3 product. Wind speed (AMSR-E and AMSR-2) are available for download at https://www.remss.com/missions/amsr/. Chl-*a* concentrations and SST were obtained from

https://oceancolor.gsfc.nasa.gov/l3/ and https://oceandata.sci.gsfc.nasa.gov/directdataaccess/Level-3%20Mapped/Aqua-MODIS). Coding scripts can be downloaded from GitHub at https://github.com/srdasara/Bellingshausen_marine_aerosol_production (Dasarathy, S. (2022). srdasara/Bellingshausen_marine_aerosol_production: Initial Release (Version 0.1.0). Zenodo. https://doi.org/10.5281/ZENODO.6608952)

CHAPTER 3: How sea ice albedo effects biogeochemical and physical diagnostics of the western Antarctic: A perturbation experiment using the Biogeochemical Southern Ocean State Estimate (B-SOSE)

1. Introduction

Sea ice coverage in the Southern Ocean has shown fluctuations of both steady increases and decreases in areal coverage across the last several decades. In contrast to the rapid sea ice decline of the Arctic and a warming climatic regime, sea ice extent (SIE) in the Southern Ocean has instead steadily increased across the satellite record from 1979 to 1999 (Comiso et al., 2017; Parkinson, 2019; Simmonds, 2015; Turner, Hosking, Bracegirdle, Marshall, & Phillips, 2015). Following this, an accelerated increase began in 2000 persisting until 2014, with record high sea ice in 2014 (Comiso et al., 2017). While these trends seemingly opposed the overall devastating losses in Arctic SIE, in most recent years, dramatic decreases in SIE in the Southern Ocean have now also been observed. A retreat in sea ice began in 2016, with record lows observed across 2017 to 2019. In the most recent austral summer of 2021 to 2022, SIE reached its lowest point yet across a 43-year satellite record, breaking numerous headlines and sparking public interest (Turner et al., 2022). Numerous factors are predicted to have led to these record lows. Prior work suggests that the low SIE observed in 2016 was largely induced by tropical sea surface temperature (SST) anomalies and a strong negative Southern Annular Mode event in late austral spring that drove sea ice southwards producing decreased SIE (Schlosser, Haumann, & Raphael, 2018; Stuecker, Bitz, & Armour, 2017; Turner et al., 2017). Persistence in SIE lows were then caused by enhanced northward Ekman transport that led to upwelling of warmer subsurface waters from below the mixed layer alongside simultaneous atmosphere and ocean coupled variabilities. This work supports that warmer ocean temperatures, combined with the direct

effects of surface wind forcing on sea ice, produced the rapid decrease of Antarctic SIE observed from 2016 to present day (Meehl et al., 2019; Schroeter, O'Kane, & Sandery, 2023).

While more recent years have shown dramatic decreases in SIE across the Southern Ocean, stark regional deviations are nevertheless present. At odds to the varied trends of highs and recent lows in SIE in the larger spatial region of the Southern Ocean, the Bellingshausen Sea of the western Antarctic Peninsula (WAP) has shown intense decline in SIE across the past half century. In the past five decades, SST in the Bellingshausen Sea region has increased by more than 1 °C (Meredith & King, 2005) and annual mean air temperatures have increased by 2–3 °C (Turner et al., 2005). Since 2011, the summertime ice-free season has increased by nearly three months as ice extent reaches a minimum in February and persists until late in the austral winter until May (Dasarathy et al., 2021). In the coming century, greenhouse gas driven warming is projected to further drive a decline in the summertime SIE (Eayrs, Li, Raphael, & Holland, 2021).

Large-scale changes in SIE dynamics have potential consequences for marine ecosystems. The arrival of austral spring marks the beginning of significant phytoplankton growth after a period of near darkness during polar winter. This is particularly important when also coinciding with water column stabilization caused by warming or freshening due to melt water input from melting sea ice or glaciers. This stabilization of the water column leads to a decreased mixed layer depth (MLD), and light conditions become favorable for phytoplankton growth and bloom formation (Bowman et al., 2018). In contrast, deep mixing and deepening of the MLD can reduce the light available for photosynthesis. Thus, this may affect the phytoplankton community including altering total biomass and changing species composition (Sverdrup, 1953). Prior studies support these hypotheses: austral summers following winters

with low sea-ice cover are characterized by decreased stratification strength and low phytoplankton biomass (Rozema et al., 2017). Low, fragmented sea-ice coverage in winter may also permit the development of an early spring phytoplankton bloom and decrease the frequency of Austral summer nearshore blooms (Bowman et al., 2018). In comparison, summers that follow winters with higher sea ice coverage exhibit increased stratification and are dominated by larger phytoplankton groups > 20 μm: these are typically diatoms that are favored under relatively high irradiance conditions (Rozema et al., 2017). With regional warming and increasing duration of the ice-free season, studies have noted declines in chlorophyll *a* (chl-*a*) concentration along the WAP over the last three decades. These changes can have cascading effects on the rest of the trophic system, making it imperative to understand how an increased duration of the summertime ice free season will affect the Bellingshausen Sea ecosystem.

To examine how changes to the presence, timing, and magnitude of sea ice affect the ecosystem of the Bellingshausen Sea, we take advantage of a modeled state estimate of the Southern Ocean: The Biogeochemical Southern Ocean State Estimate (B-SOSE). The Southern Ocean State Estimate (SOSE) was previously developed to provide a baseline to understand the physics controlling the Southern Ocean (Mazloff, Heimbach, & Wunsch, 2010). SOSE is an eddy-permitting general circulation model of the Southern Ocean. The state estimate is fit by constrained least squares to a large suite of observational data from Argo float profiles, CTD synoptic sections, Southern Elephant Seals as Oceanographic Samplers (SEaOS) instrument-mounted seal profiles, XBTs, altimetric observations, and infrared and microwave radiometer observed sea surface temperature (Verdy & Mazloff, 2017). More recently, a biogeochemical model has been incorporated into the SOSE framework and constrained to observations, thereby producing B-SOSE. B-SOSE was conceived with the central purpose of attaining a best estimate

of the large-scale carbon system properties of the Southern Ocean. This state estimate utilizes the Biogeochemistry with Light, Iron, Nutrients, and Gases (BLING) model to realistically simulate large-scale ocean biogeochemistry. For example, using BLING, biomass-based phytoplankton size structure estimation is a function of light, nutrient limitation, temperature, and steady-state growth versus loss (Dunne et al., 2020). Using B-SOSE, we studied realistic simulations of biogeochemical parameters relevant to examining the surface ocean biosphere of the WAP and attained these data at 1/6-degree resolution.

As the WAP and Bellingshausen Sea exhibit the largest and fastest Antarctic sea-ice decreases, herein we conducted a perturbation experiment that modeled the WAP environment with both increased and decreased magnitudes of sea ice. To isolate the impact of sea ice, we perturbed the sea ice albedo of the Bellingshausen Sea. By modeling changes to the magnitude and extent of sea ice in the WAP, we examined whether differences to an ice-free duration and extent leads to expected changes in biomass and structure of small and large phytoplankton groups. We also examined the effects on the other biogeochemical and physical diagnostics including mixed layer depth (MLD), phytoplankton growth rate, net primary and community production (NPP and NCP), particulate organic carbon (POC), and nutrient concentrations of iron and nitrate. We perturb the sea ice albedo of the Biogeochemical Southern Ocean State Estimate (B-SOSE) to answer the following: (1) How does perturbing sea ice albedo impact the timing and magnitude of sea ice melt in spring and freezing in late fall? Is the timing of freezing the same, or is there delayed onset of sea-ice return? (2) What is the impact on the MLD? (3) How do these changes affect the distribution of biogeochemical diagnostics small and large phytoplankton biomass, particulate organic carbon (POC), net primary production (NPP), net

community production (NCP), phytoplankton growth rate, and iron and nitrate concentration in the Bellingshausen Sea?

2. Data Sources and Methods

2.1 Experimental Setup

B-SOSE – within the NASA Estimating the Circulation and Climate of the Ocean (ECCO) consortium – is a coupled biogeochemical-sea ice-ocean state estimate of the Southern Ocean and is the product of 4D-Var data assimilation to fit observations from Biogeochemical (BGC) Argo floats and is found at http://sose.ucsd.edu. Using B-SOSE, we studied realistic simulations of biogeochemical parameters relevant to examining the surface ocean biosphere of the WAP and attained these data at 1/6-degree resolution. Through perturbing the modeled sea ice albedo, we examined three different model scenarios that capture a gradient of SIE in the Bellingshausen Sea across the spatial grid between 100 °W to 54 °W and 60 °S to 75 °S. We were therefore able to examine what realistically happens to the downstream ecosystem and biogeochemistry of this environment when the timing and magnitude of sea ice melt and refreeze is perturbed.

To examine how perturbing sea ice albedo affected this environment, we examined the physical diagnostics sea ice area and mixed layer depth (MLD) and the 3-D diagnostics large surface (>5 μm) phytoplankton biomass (LSPB), small surface phytoplankton biomass (SSPB), NCP, NPP, POC, and phytoplankton growth rate integrated from the surface ocean to a depth of 80 meters. Spatial analyses are conducted by examining the first year of perturbations from October 2013 until May 2014 (Figures 3.1, 3.2, 3.5 to 3.10, S1 to S12). Temporal analyses are conducted by examining these weekly data across December 4th 2012 to January 6th 2015

(Figures 3.3 and 3.4). In doing so, we examine how the onset of perturbations to the timing of sea ice melt and associated refreeze immediately impacts the downstream ecosystem.

2.2 Gradient of Perturbations

All perturbations are visualized in Figure 3.1. Our **first scenario**–the control–is the B-SOSE model solution without perturbation to sea ice albedo, with expected melt of sea ice in austral spring and refreeze in austral fall (Figure 3.1b). We examine our control against the **second scenario**–the high albedo condition–in which sea ice is perturbed by increasing its albedo thereby absorbing less shortwave radiation and theoretically slowing down sea ice melt in austral spring and summer (Figure 3.1a). The control without perturbation to sea ice albedo is also examined against the **third scenario**–the low albedo condition–in which sea ice is perturbed by decreasing its albedo, thereby absorbing more shortwave radiation, theoretically a quicker melt in sea ice in austral spring (Figure 3.1c).

2.3. Time-Series and Percent Change

Weekly averaged time-series (Figure 3.2) were constructed for sea ice, MLD, small surface phytoplankton biomass (SSPB), large surface phytoplankton biomass (LSPB), particulate organic carbon (POC), net primary production (NPP), net community production (NCP), phytoplankton growth rate, iron concentration, and nitrate concentration across December 2012 to December 2014. To calculate the time series, first, the integral of the biogeochemical diagnostics SSPB, LSPB, POC, NPP, NCP, and growth rate was taken from the surface ocean to a depth of 80 meters across each pixel of the spatial grid. The integral of iron and nitrate concentration was similarly calculated to a depth of 250 meters. Weekly values were then calculated by averaging these values within the Bellingshausen Sea spatial grid. In calculating

the mean within spatial bins, missing values were excluded. SSPB, LSPB, POC, NPP, and NCP are in units of mol $\frac{C}{m^3}$. Iron and nitration concentrations are similarly in units of $\frac{mol}{m^3}$. Using weekly averages of all variables, percent change (Figure 3.4) was calculated by differencing the high albedo and low albedo conditions against the control for all variables.

2.. Spatial Gridding and Difference Plots

Spatial grids were constructed for all variables, sea ice area, MLD, SSPB, LSPB, POC, NPP, NCP, growth rate, iron, and nitrate concentration at a resolution of 1/6-degree from October 2013 to May 2014 (Figures 3.1, 3.2, 3.5 to 3.10, S3.1 to S3.12). The integral was taken from the surface ocean to a depth of 80 meters for SSPB, LSPB, POC, NPP, NCP, and growth rate. The integral was also taken for nitrate and iron concentration from the surface to a depth 250 meters. Difference plots were constructed for the same months by subtracting the control from the high albedo and low albedo conditions, respectively. We therefore assess how both the high albedo and low albedo perturbations compare against the control across space and time.

3. Results

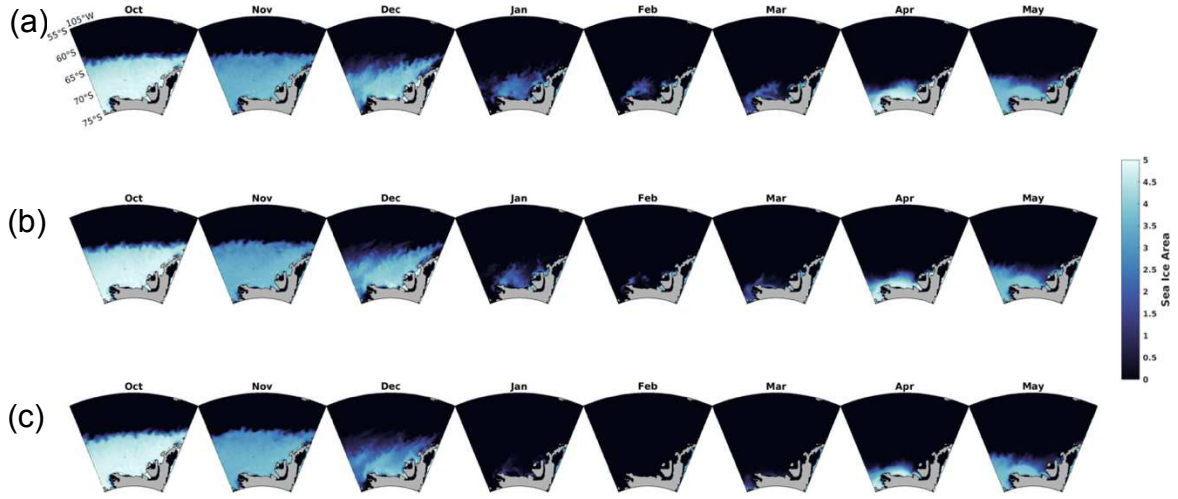

Figure 3.1. Sea Ice areal coverage across October 2013 to May 2014 in the Bellingshausen Sea. **Row a** represents the high sea ice albedo perturbation to the Biogeochemical Southern Ocean State Estimate. **Row b** represents the control scenario without perturbation to sea ice albedo. **Row c** represents low sea ice albedo perturbation.

The model solution with perturbations to sea ice albedo began its run for the month of December 2012. We examined spatial trends for all variables across the months of October 2013 to May 2014 (Figures 3.1 and 3.2), thereby observing how the perturbation to sea ice albedo impacted downstream physical and biogeochemical diagnostics soon after the perturbations took effect. We also examined temporal trends across the first two years of perturbations from December 2012 to December 2014.

3.1 Impact of Perturbations on Sea Ice

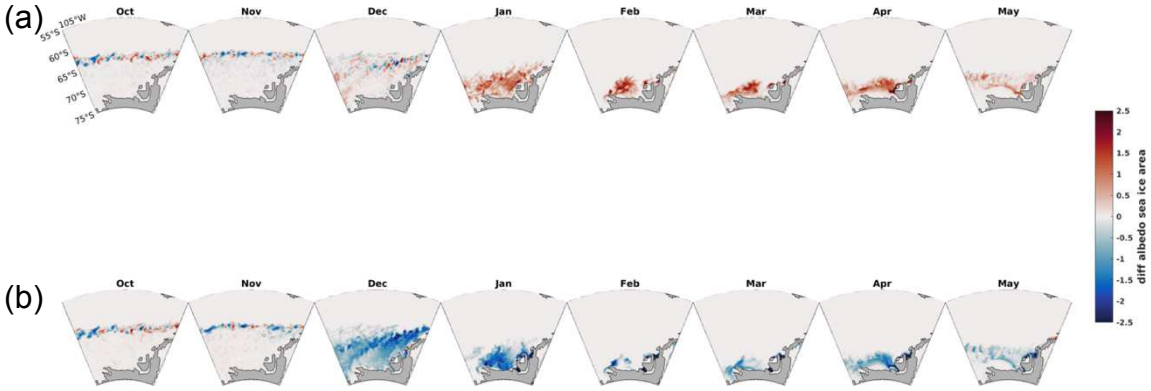

Figures 3.2. Sea ice difference plots across October 2013 to May 2014 in the Bellingshausen Sea. **Row a** represents the high albedo perturbation minus the control albedo perturbation. **Row b** represents the low albedo perturbation minus the control albedo perturbation.

When examining spatial trends of the high albedo scenario across October 2013 to May 2014 (Figure 3.1a and 3.2a), an increase in sea ice albedo caused the expected increase in magnitudes of sea ice in comparison to the control, particularly pronounced in the month of January 2014 (Figure 3.2a). In January 2014, sea ice melt is occurring but is still of greater magnitude than the control; in fact, sea ice extent is greater than the control across all months, best visualized in Figure 3.2a. Interestingly, refreeze of sea ice begins at the same time as the control following February 2014 (timeseries Figure 3.3a). This month shows an increase in sea ice magnitudes with further coverage across the southern coastline of the WAP following austral summer in comparison the control scenario without perturbation (Figure 3.1). In contrast, the low albedo scenario (Figure 3.1c, 3.2b) shows the opposite when compared against the control. Sea

ice melt is more pronounced than in the control particularly in the month of December (Figure 3.2b).

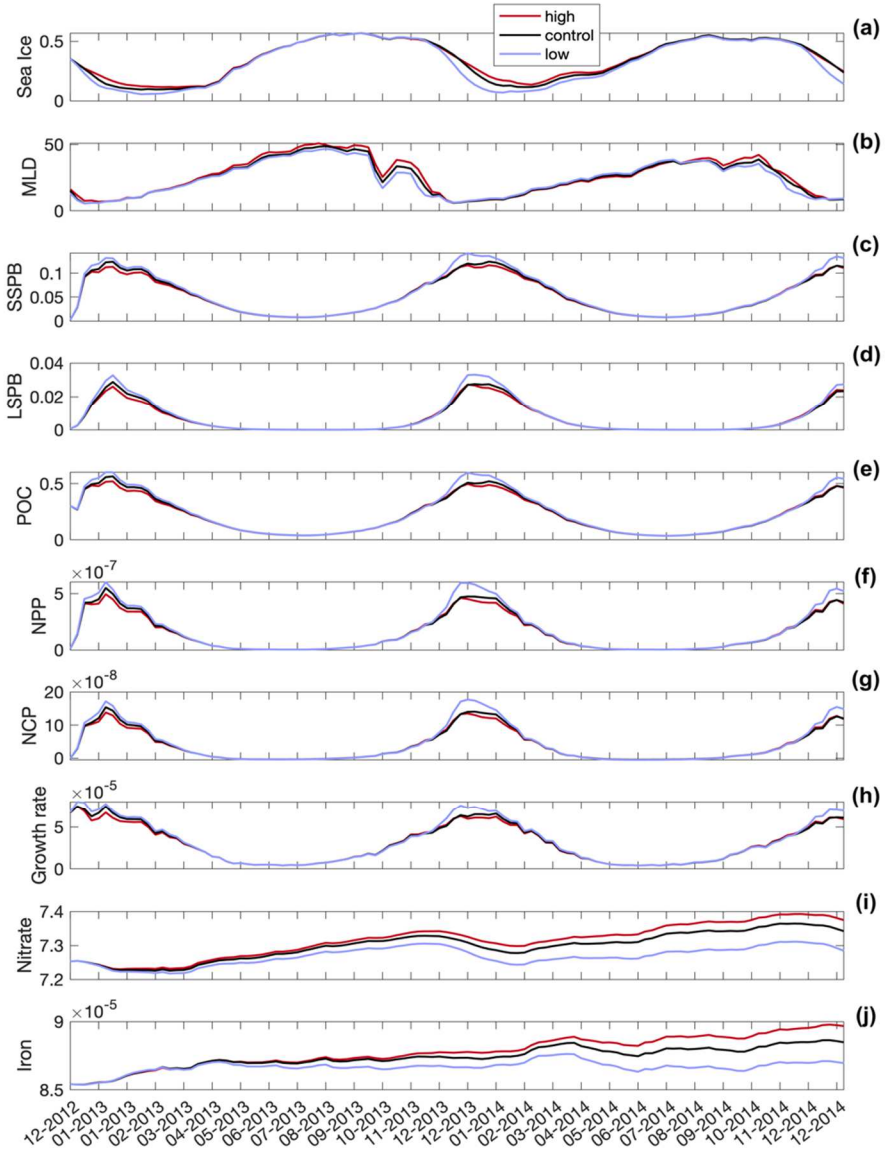

Figure 3.3. Weekly time series of all diagnostics across December 2012 to December 2014. Diagnostics examined are sea ice area, mixed layer depth (MLD), small surface phytoplankton biomass (SSPB), large surface phytoplankton biomass (LSPB), particulate organic carbon (POC), net primary production (NPP), net community production (NCP), phytoplankton growth rate, nitrate, and iron concentration. To obtain weekly average, these diagnostics are averaged across the Bellingshausen Sea spatial grid between 100 °W to 54 °W and 60 °S to 75 °S. Red lines represent the high albedo perturbation, black lines represent the control albedo scenario, and the blue lines represent the low albedo scenario.

While magnitudes of SIE are different in austral summers December to March (Figure

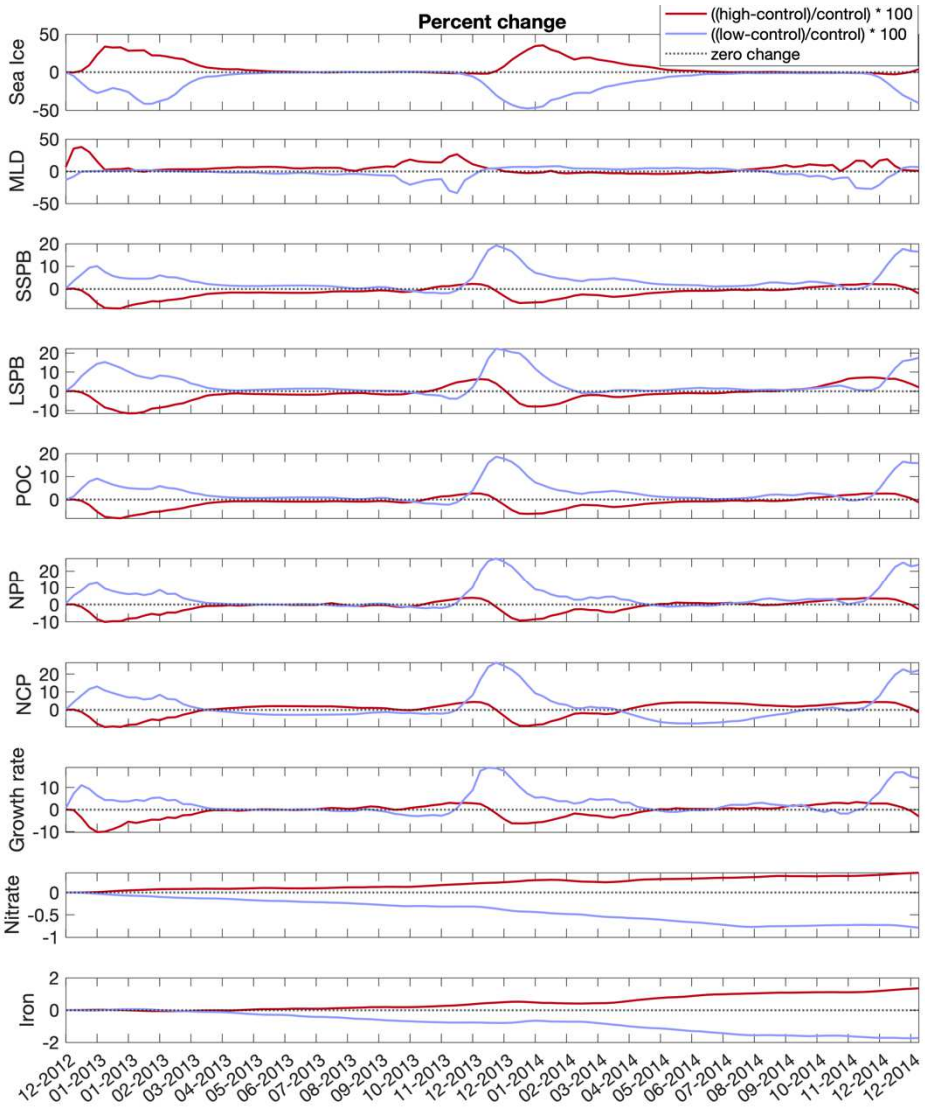

Figure 3.4. Percent change of the high albedo scenario versus the control (red lines) and the low albedo versus the control (blue lines) for all diagnostics across December 2012 to December 2014. Diagnostics examined are sea ice area, mixed layer depth (MLD), small surface phytoplankton biomass (SSPB), large surface phytoplankton biomass (LSPB), particulate organic carbon (POC), net primary production (NPP), net community production (NCP), phytoplankton growth rate, nitrate, and iron concentration. Percent change is calculated using averages of these diagnostics throughout the Bellingshausen Sea spatial grid between 100 °W to 54 °W and 60 °S to 75 °S. The black dotted line represents zero change.

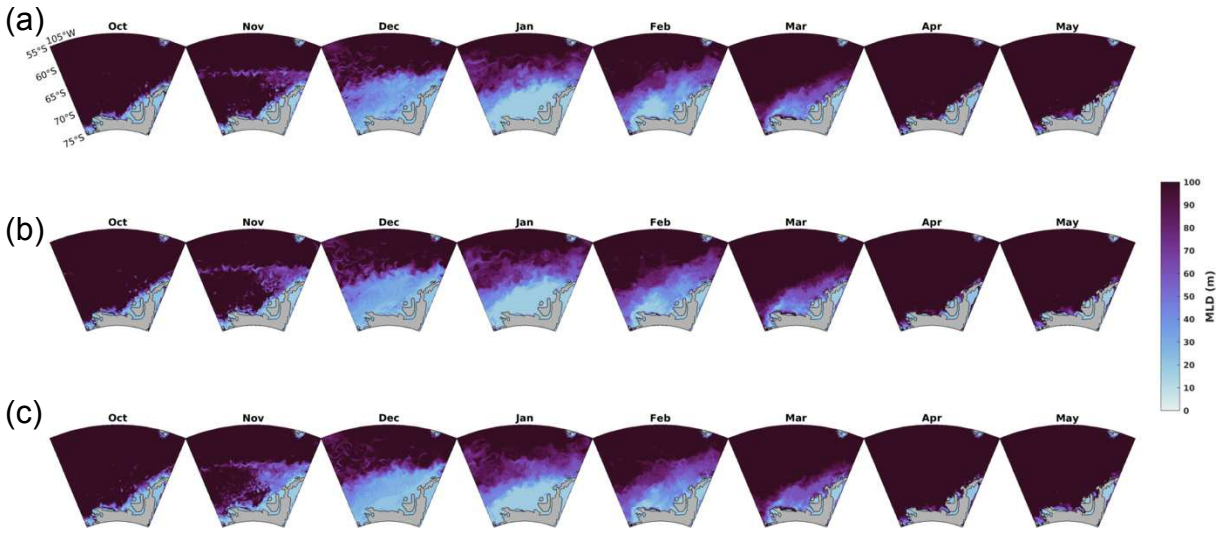

Figure 3.5. Spatial distribution of mixed layer depth (MLD) across October 2013 to May 2014 in the Bellingshausen Sea. **Row a** represents the perturbation of increase in sea ice albedo to the Biogeochemical Southern Ocean State Estimate. **Row b** represents the control scenario without perturbation to sea ice albedo. **Row c** represents the perturbation of decrease in sea ice albedo.

3.3a) across all three perturbation scenarios, the timing in the initial onset of melt (December 2013) and refreeze (beginning February 2014) are at the same time (Figure 3.3a). In the first summer from December 2012, in which the model solution was initiated, we observe a greater melt of sea ice with lowered magnitudes in the low albedo scenario in comparison to both the control and high albedo scenarios. In the first austral fall and the month of April 2013, the refreeze of sea ice reaches the same magnitude across all perturbations, also visualized as percent change collapses to near zero (Figure 3.4a). In the second summer of analysis, deviations across perturbations in magnitudes of melt and refreeze of sea ice are pronounced. In the low albedo scenario, the melt of sea ice begins at the same time but shows a steeper decline in magnitude than the high albedo scenario (Figure 3.3a). Refreeze of sea ice begins across the same month in austral fall in all albedo scenarios, February to March 2014, but is lesser in magnitude (Figures 3.1c, Figure 3.3a). A longer ice-free summer occurs in the low albedo scenario during the second

austral summer. There is a delay in which sea ice magnitudes approach the same refreeze magnitude as the control and high albedo scenarios. In the first year of analysis, sea ice in the low albedo scenario reached the same magnitude as the control when refreezing in April 2013. In the second year of analysis this doesn't happen until June 2014, indicating a longer summer of two months (Figure 3.3a).

3.2 Impact of Perturbations on MLD

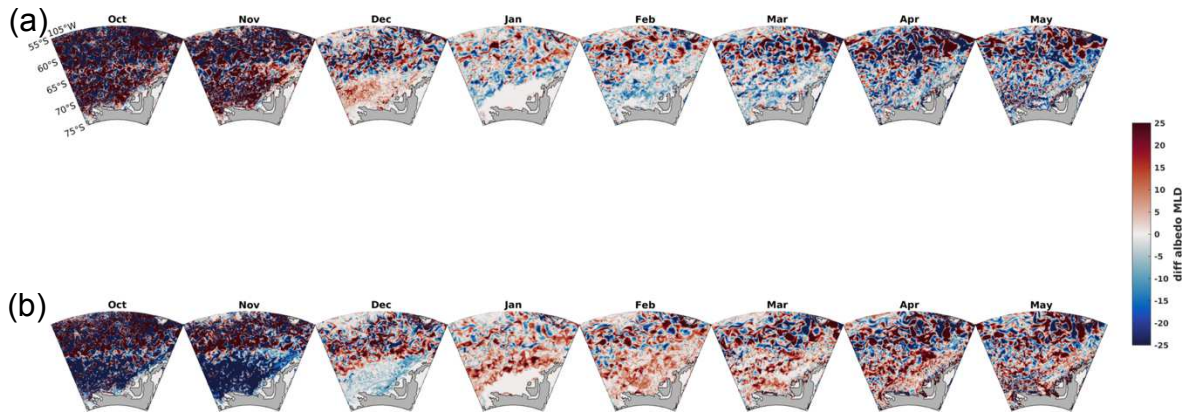

Figure 3.6. Mixed layer depth (MLD) difference plots across October 2013 to May 2014 in the Bellingshausen Sea. **Row a** represents the high albedo perturbation minus the control albedo perturbation. **Row b** represents the low albedo perturbation minus the control albedo perturbation.

Spatial trends indicate that perturbing sea ice albedo had varied impacts on MLD across the Bellingshausen Sea spatial grid (Figures 3.5 and 3.6). In the high albedo scenario, with greater sea ice coverage than the control across all months of analysis, the months of October through December exhibit a deeper MLD particularly near the coastline of the WAP from latitudes of 65 to 73 °S. This same region then appears to switch trends from January to May 2014, with the MLD shoaling in comparison to the control. The opposite trends are true in the low albedo scenario in comparison to the control, with a shallower MLD across October 2013 to

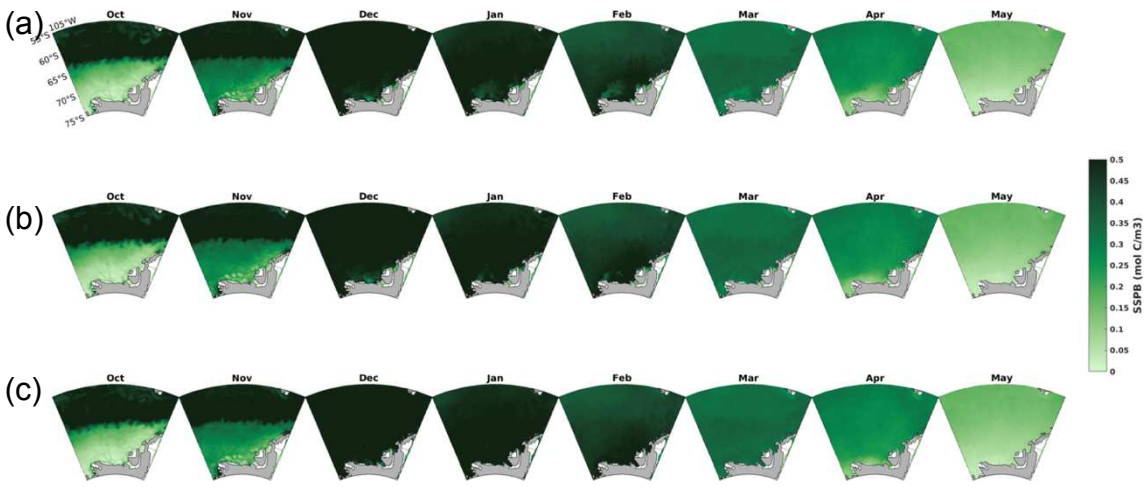

Figure 3.7. Spatial distribution of small surface phytoplankton biomass across October 2013 to May 2014 in the Bellingshausen Sea. **Row a** represents the perturbation of increase in sea ice albedo to the Biogeochemical Southern Ocean State Estimate. **Row b** represents the control scenario without perturbation to sea ice albedo. **Row c** represents the perturbation of decrease in sea ice albedo.

December 2013 and a deeper MLD across January 2014 to March 2014, particularly pronounced near the coastlines of the WAP from latitudes of 65 to 73 °S. When examining the time series, trends in MLD across all perturbation scenarios follow similar patterns of shoaling during austral spring (Figures 3.3 and 3.4). The MLD then deepens from austral summer to the following austral winter. On average across the Bellingshausen Sea spatial grid, the high albedo scenario has a deeper MLD by nearly 1 to 5 meters in comparison to the control. The opposite is true for the low albedo scenario, with a shallower MLD in comparison to the control on average throughout the spatial grid. The low albedo scenario had the shallowest MLD out of all perturbation scenarios when averaged across the Bellingshausen Sea spatial grid (Figures 3.3 and 3.4).

3.2 Impact of Perturbations on SSPB, LSPB, POC, NCP, NPP, and Phytoplankton Growth Rate

We also examined spatial trends for the biogeochemical 3D diagnostics SSPB, LSPB, POC, NCP, NPP, and phytoplankton growth rate across the months of October 2013 to May 2014 (Figures 3.7 to 3.10, S3.1 to S3.8), thereby observing how the perturbation to sea ice albedo impacted the primary trophic community structure and production of the Bellingshausen Sea. These variables represent the integral across each latitude-longitude pixel from the surface ocean to a depth of 80 meters. In contrast to the control, an increase in sea ice albedo caused an overall decrease in magnitudes of blooms of SSPB and LSPB in austral summer in comparison to the

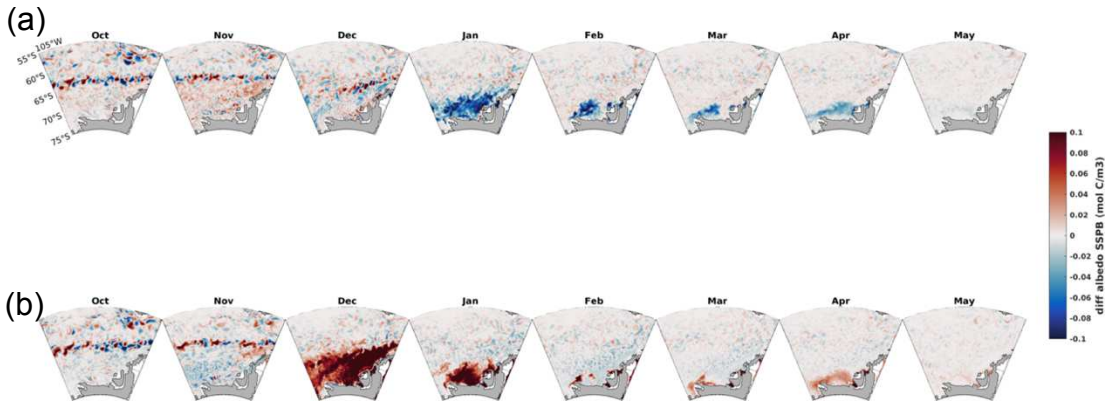

Figure 3.8. Small surface phytoplankton biomass (SSPB) spatial difference plots across October 2013 to May 2014 in the Bellingshausen Sea. **Row a** represents the high albedo perturbation minus the control albedo perturbation. **Row b** represents the low albedo perturbation minus the control albedo perturbation.

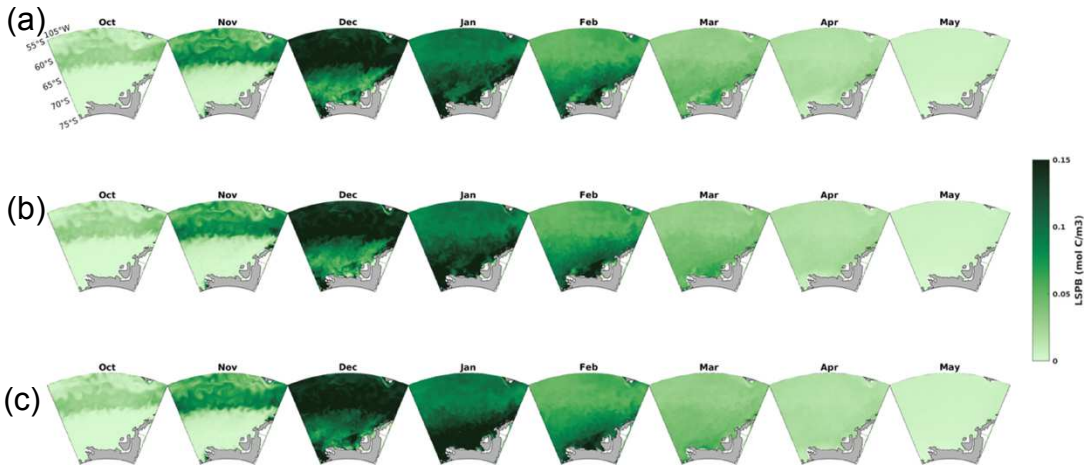

Figure 3.9. Spatial distribution of large surface phytoplankton biomass (LSPB) across October 2013 to May 2014 in the Bellingshausen Sea. **Row a** represents the perturbation of increase in sea ice albedo to the Biogeochemical Southern Ocean State Estimate. **Row b** represents the control scenario without perturbation to sea ice albedo. **Row c** represents the perturbation of decrease in sea ice albedo.

control scenario (Figures 3.7 to 3.10). Similar trends in the high albedo scenario in comparison to the control are visualized across POC, NCP, NPP, and phytoplankton growth rate (S3.1 to S3.8). Across the coastline of the WAP, the decrease in magnitudes of SSPB, LSPB, POC, NCP, NPP and phytoplankton growth rate persisted until the following austral fall.

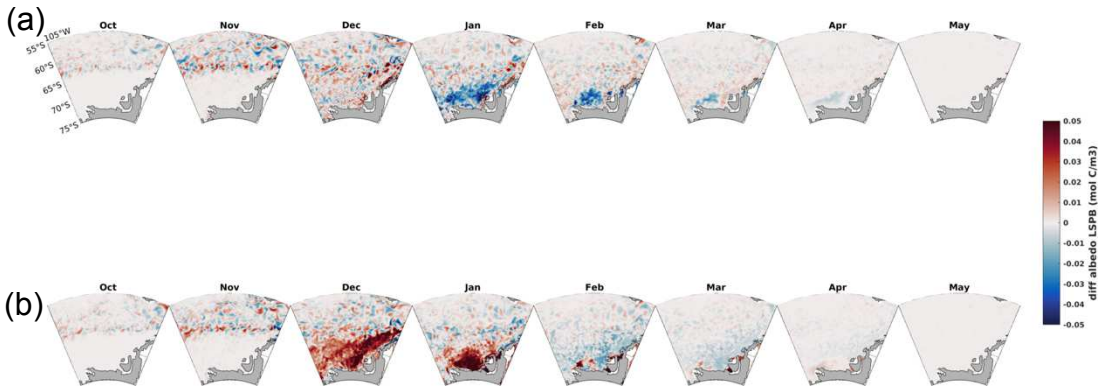

Figure 3.10. Large surface phytoplankton biomass (LSPB) difference plots across October 2013 to May 2014 in the Bellingshausen Sea. **Row a** represents the high albedo perturbation minus the control albedo perturbation. **Row b** represents the low albedo perturbation minus the control albedo perturbation.

In the low albedo scenario, the melt of sea ice is associated with visually striking increases in magnitudes of SSPB, LSPB, POC, NCP, NPP, and phytoplankton growth rate, particularly pronounced in the summer months of December 2013 and January 2014. This increase in comparison to the control is visualized until the following fall in April 2014. The time series also represent these trends, with the low albedo scenario being associated across both austral summers on record with increases in overall magnitudes of SSPB, LSPB, POC, NPP, NCP, and growth rate. This is also visualized in the percent change plots. In the low albedo scenario, there is a large increase across the variables in comparison to the control scenario. The high albedo scenario is the opposite: while there is a summertime increase in these diagnostics, the high albedo scenario nevertheless shows an otherwise overall decrease in these variables across time in comparison to the control.

Interestingly, when examining LSPB in the high albedo scenario (Figures 3.9a and 3.10a), while there is otherwise an overall decrease in LSPB magnitudes as visualized in the time series and percent change plots (Figures 3.3 and 3.4), blooms of large phytoplankton at greater magnitudes than the control occur across the peninsular arm stretching northwards. These

blooms persist from December 2013 until March 2014. This spatial trend is not as pronounced for SSPB magnitudes across the same spatial region (Figures 3.7c and 3.8b), which also have a dramatic increase versus the control. High albedo trends of the increase in magnitudes across the peninsular arm stretching northwards also appears but also appears when examining spatial trends of NPP, NCP, and phytoplankton growth rate (Figures S3.3 to 3.8). While otherwise the high albedo scenario and increased sea ice coverage causes an overall drop in magnitudes of these biogeochemical diagnostics (Figures 3.3 and 3.4), an increase in magnitudes of LSPB, NCP, NPP, and phytoplankton growth rate occur across the peninsula.

3.3 Impact of Perturbations on Nitrate and Iron

We examined spatiotemporal trends for the diagnostics nitrate and iron (Figures 3.3, 3.4, S3.9 to S3.12), thereby observing how the perturbation to sea ice albedo and associated phytoplankton blooms and ecosystem effects impacted nutrients present in the Bellingshausen Sea environment. These variables represent the integral across each latitude-longitude pixel from the surface ocean to a depth of 250 meters. Spatial trends (Figures S3.9 to S3.12), most pronounced in the spatial difference plots (S3.10 and S3.12), indicate that trends in the high albedo and low albedo plots are varied across small regional scales. Distinct differences in the distribution of these nutrients persist across the spatial grid. However, a clearer picture of what is happening to nutrient concentrations over time emerges when examining the timeseries and percent change plots (Figures 3.3 and 3.4). Over time, nitrate and iron concentrations become depleted in the low albedo scenario versus the control and high albedo scenario. In comparison to the control, this depletion in nitrate and iron occurs throughout the two years of analysis (Figure 3.4). The opposite is true for the high albedo scenario throughout the Bellingshausen Sea, with

an accumulation of nutrients in comparison to the control across the temporal record (Figure 3.4).

4. Discussion & Conclusions

In this study we evaluated how perturbing sea ice albedo in the modeled B-SOSE effected physical and biogeochemical diagnostics of the Bellingshausen Sea. We explored the following research questions: (1) How does perturbing sea ice albedo impact the timing and magnitude of sea ice melt in austral spring and summer and freezing in austral fall? Is the timing of freezing the same, or is there delayed onset of sea-ice return? (2) How do these changes affect the distribution of biogeochemical diagnostics small and large phytoplankton biomass, particulate organic carbon (POC), net primary production (NPP), net community production (NCP), phytoplankton growth rate, and iron and nitrate concentration in the Bellingshausen Sea?

(1) We found that magnitudes and extent of sea ice was increased throughout the analysis in the high albedo scenario in comparison to the control and low albedo scenarios. While the acceleration of melt and refreeze were different across perturbations, the timing of the onset of sea ice melt in austral summer remained the same, with melt of sea ice initiating across perturbations in December 2013 and refreeze initiating in February 2014 (Figure 3.3). The impact of perturbing sea ice albedo was more drastic in the second year of analysis. The low albedo scenario exhibited a longer summer by nearly two months characterized by less SIE and fragmented sea ice coverage in the second year of analysis (Figures 3.1 to 3.3), not fully reaching the same magnitude of refreeze as the control and high albedo scenarios until July 2014. In comparison, the low albedo scenario matched the same magnitude of refreeze in the first summer in April 2013. This model perturbation of a longer summertime ice-free season mimics the real

world. Since 2011, the summertime ice-free season of the WAP has increased by nearly three months as ice extent reaches a minimum in February and persists until late in the austral winter until May (Dasarathy et al., 2021).

(2) With the modeled melt of sea ice in the low albedo scenario, despite a longer ice-free summer, the biogeochemical diagnostics SSPB, LSPB, phytoplankton growth rate, POC, NPP, and NCP were greater in magnitude over austral summers than the control or high albedo scenarios. This initially seems at odds to prior work which indicates the detriments to WAP food web structure in a warming climate. For example, this prior work has supported that the ongoing loss of winter sea-ice, associated to the recent rapid regional climate warming, modulates the dynamics of phytoplankton blooms with alterations to phytoplankton community structure by a shift from large phytoplankton (diatoms) to smaller flagellated species (Saba et al., 2014). However, the shifts in community structure and decreased biogeochemical diagnostics are caused by austral winters with less SIE and fragmented ice coverage. A low SIE winter was not observed in our analysis. Even in the second austral summer, the low albedo scenario exhibited a winter of the same sea ice magnitudes as the control and high albedo scenarios persisting from nearly June 2014 to December 2013. Thus, the increase in magnitudes of SSPB, LSPB, phytoplankton growth rate, NPP, and NCP observed in our study across austral summers in Figure 3.3 was instead likely caused by water column stabilization from warming and freshening due to melt water input from melting sea ice following an icy winter. This is supported by our assessment of modeled MLD (Figure 3.3, 3.4, 3.5, and 3.6), in which a shallower MLD persists across time in the low albedo scenario, particularly pronounced during the austral spring to summer from October to December (Figure 3.5). Availability of iron and nitrate in the low albedo scenario also supports the phytoplankton blooms observed before both austral summer

(Figure 3.3, 3.4, S3.9 to S3.12). As such, with the shoaling of the MLD caused from melting of sea ice in winter, light conditions become favorable for phytoplankton growth and bloom formation. This, combined with nutrient availability for phytoplankton growth, cause the increase in magnitudes of SSPB, LSPB, phytoplankton growth rate, NPP, and NCP.

While the first two years of modeled perturbations indicate that an increase in biogeochemical diagnostics happens over both austral summers from December 2012 to March 2013 and December 2013 to March 2014, we predict that the model will capture the opposite with a decrease in magnitudes of LSPB, phytoplankton growth rate, NCP, and NPP given more time in the model run. For example, nutrient limitation is a well-known inhibitor of phytoplankton blooms (Kevin R. Arrigo, 1999). In our study, nutrient limitation has not yet set in as a factor inhibiting bloom formation; however, warning signs are present as nutrient depletion is observed in the low albedo versus the control and high albedo scenarios (Figures 3.3 and 3.4). Alongside nutrient depletion, we also observe the beginnings of a longer ice-free summer. We predict that subsequent winters in the low albedo perturbation model run will exhibit lower magnitudes of SIE and fragmented sea ice coverage, not matching the same winter ice extent as the control and high albedo scenarios. As icy winters induce the stratification and stabilization of the water column in austral summers from melting and freshwater input, the lack of icy winters might alter the intensity of phytoplankton blooms in our model. Prior work supports these hypotheses: relatively low biomass concentrations generally following winters with low sea ice cover (Ducklow et al., 2013; Rozema et al., 2017). These results have been associated with light limitation, most severe following winters with low sea ice cover, due to weak stratification and anomalously deep mixed layers during austral spring and summer, resulting from higher exposure to winter winds (Kevin R. Arrigo et al., 2017). As the MLD becomes deeper and less

stable, this can lead to overall lower phytoplankton biomass across the region (Bowman et al., 2018). As such, our study observing how sea ice in the WAP impacts biogeochemistry and nutrients is imperative. As interannual phytoplankton dynamics are tightly coupled to krill recruitment (Saba et al., 2014) and krill in turn are the main food source for penguins, seals, whales, and other predators (Ducklow et al., 2013), examining the changing sea ice landscape of the WAP is necessary to understand its future ecosystem structure.

REFERENCES

Akoglu, H. (2018). User's guide to correlation coefficients. *Turkish Journal of Emergency Medicine*, *18*(3), 91–93. https://doi.org/10.1016/j.tjem.2018.08.001

Ardyna, M., Babin, M., Gosselin, M., Devred, E., Rainville, L., & Tremblay, J.-É. (2014). Recent Arctic Ocean sea ice loss triggers novel fall phytoplankton blooms: PHYTOPLANKTON PHENOLOGY IN THE ARCTIC. *Geophysical Research Letters*, *41*(17), 6207–6212. https://doi.org/10.1002/2014GL061047

Arrigo, Kevin R. (1999). Phytoplankton Community Structure and the Drawdown of Nutrients and CO2 in the Southern Ocean. *Science*, *283*(5400), 365–367. https://doi.org/10.1126/science.283.5400.365

Arrigo, Kevin R. (2014). Sea Ice Ecosystems. *Annual Review of Marine Science*, *6*(1), 439–467. https://doi.org/10.1146/annurev-marine-010213-135103

Arrigo, Kevin R., van Dijken, G. L., Alderkamp, A., Erickson, Z. K., Lewis, K. M., Lowry, K. E., … van de Poll, W. (2017). Early Spring Phytoplankton Dynamics in the Western Antarctic Peninsula. *Journal of Geophysical Research: Oceans*, *122*(12), 9350–9369. https://doi.org/10.1002/2017JC013281

Arrigo, Kevin R., van Dijken, G. L., & Bushinsky, S. (2008). Primary production in the Southern Ocean, 1997–2006. *Journal of Geophysical Research*, *113*(C8), C08004. https://doi.org/10.1029/2007JC004551

Arrigo, Kevin R., van Dijken, G., & Pabi, S. (2008). Impact of a shrinking Arctic ice cover on marine primary production. *Geophysical Research Letters*, *35*(19), L19603. https://doi.org/10.1029/2008GL035028

Barth, M. C., Rasch, P. J., Kiehl, J. T., Benkovitz, C. M., & Schwartz, S. E. (2000). Sulfur chemistry in the National Center for Atmospheric Research Community Climate Model: Description, evaluation, features, and sensitivity to aqueous chemistry. *Journal of Geophysical Research: Atmospheres*, *105*(D1), 1387–1415. https://doi.org/10.1029/1999JD900773

Becagli, S., Lazzara, L., Marchese, C., Dayan, U., Ascanius, S. E., Cacciani, M., … Udisti, R. (2016). Relationships linking primary production, sea ice melting, and biogenic aerosol in the Arctic. *Atmospheric Environment*, *136*, 1–15. https://doi.org/10.1016/j.atmosenv.2016.04.002

Behrenfeld, M. J., Hu, Y., O'Malley, R. T., Boss, E. S., Hostetler, C. A., Siegel, D. A., … Scarino, A. J. (2017). Annual boom–bust cycles of polar phytoplankton biomass revealed by space-based lidar. *Nature Geoscience*, *10*(2), 118–122. https://doi.org/10.1038/ngeo2861

Blanchard, D. C., & Woodcock, A. H. (1980). THE PRODUCTION, CONCENTRATION, AND VERTICAL DISTRIBUTION OF THE SEA-SALT AEROSOL. *Annals of the New York Academy of Sciences*, *338*(1 Aerosols), 330–347. https://doi.org/10.1111/j.1749-6632.1980.tb17130.x

Bowman, J. S., Kavanaugh, M. T., Doney, S. C., & Ducklow, H. W. (2018). Recurrent seascape units identify key ecological processes along the western Antarctic Peninsula. *Global Change Biology*, *24*(7), 3065–3078. https://doi.org/10.1111/gcb.14161

Brechtel, F. J., Kreidenweis, S. M., & Swan, H. B. (1998). Air mass characteristics, aerosol particle number concentrations, and number size distributions at Macquarie Island during the First Aerosol Characterization Experiment (ACE 1). *Journal of Geophysical Research: Atmospheres*, *103*(D13), 16351–16367. https://doi.org/10.1029/97JD03014

Brooks, S. D., & Thornton, D. C. O. (2018). Marine Aerosols and Clouds. *Annual Review of Marine Science*, *10*(1), 289–313. https://doi.org/10.1146/annurev-marine-121916-063148

Browse, J., Carslaw, K. S., Mann, G. W., Birch, C. E., Arnold, S. R., & Leck, C. (2014). The complex response of Arctic aerosol to sea-ice retreat. *Atmospheric Chemistry and Physics*, *14*(14), 7543–7557. https://doi.org/10.5194/acp-14-7543-2014

Cavalli, F. (2004). Advances in characterization of size-resolved organic matter in marine aerosol over the North Atlantic. *Journal of Geophysical Research*, *109*(D24), D24215. https://doi.org/10.1029/2004JD005137

Charlson, R. J., Lovelock, J. E., Andreae, M. O., & Warren, S. G. (1987). Oceanic phytoplankton, atmospheric sulphur, cloud albedo and climate. *Nature*, *326*(6114), 655–661. https://doi.org/10.1038/326655a0

Chen, L., Wang, J., Gao, Y., Xu, G., Yang, X., Lin, Q., & Zhang, Y. (2012). Latitudinal distributions of atmospheric MSA and MSA/nss-SO_4^{2-} ratios in summer over the high latitude regions of the Southern and Northern Hemispheres: MSA AND NSS-SO_4^{2-} OVER POLAR REGIONS. *Journal of Geophysical Research: Atmospheres*, *117*(D10), n/a-n/a. https://doi.org/10.1029/2011JD016559

Coakley, J. A., Cess, R. D., & Yurevich, F. B. (1983). The Effect of Tropospheric Aerosols on the Earth's Radiation Budget: A Parameterization for Climate Models. *Journal of the Atmospheric Sciences*, *40*(1), 116–138. https://doi.org/10.1175/1520-0469(1983)040<0116:TEOTAO>2.0.CO;2

Comiso, J. C., Gersten, R. A., Stock, L. V., Turner, J., Perez, G. J., & Cho, K. (2017). Positive Trend in the Antarctic Sea Ice Cover and Associated Changes in Surface Temperature. *Journal of Climate*, *30*(6), 2251–2267. https://doi.org/10.1175/JCLI-D-16-0408.1

Comiso, J. C., & Hall, D. K. (2014). Climate trends in the Arctic as observed from space: Climate trends in the Arctic as observed from space. *Wiley Interdisciplinary Reviews: Climate Change*, *5*(3), 389–409. https://doi.org/10.1002/wcc.277

Curran, M. A. J., van Ommen, T. D., Morgan, V. I., Phillips, K. L., & Palmer, A. S. (2003). Ice Core Evidence for Antarctic Sea Ice Decline Since the 1950s. *Science*, *302*(5648), 1203. https://doi.org/10.1126/science.1087888

Dasarathy, S., Kar, J., Tackett, J., Rodier, S. D., Lu, X., Vaughan, M., … Bowman, J. S. (2021). Multi□Year Seasonal Trends in Sea Ice, Chlorophyll Concentration, and Marine Aerosol Optical Depth in the Bellingshausen Sea. *Journal of Geophysical Research: Atmospheres*, *126*(21). https://doi.org/10.1029/2021JD034737

Dasarathy, S., Russell, L. M., Rodier, S. D., & Bowman, J. S. (2023). Wind□Driven and Seasonal Effects on Marine Aerosol Production in the Bellingshausen Sea, Antarctica. *Geophysical Research Letters*, *50*(3). https://doi.org/10.1029/2022GL099723

de Leeuw, G., Andreas, E. L., Anguelova, M. D., Fairall, C. W., Lewis, E. R., O'Dowd, C., … Schwartz, S. E. (2011). Production flux of sea spray aerosol. *Reviews of Geophysics*, *49*(2), RG2001. https://doi.org/10.1029/2010RG000349

Delille, B., Jourdain, B., Borges, A. V., Tison, J.-L., & Delille, D. (2007). Biogas (CO_2, O_2, dimethylsulfide) dynamics in spring Antarctic fast ice. *Limnology and Oceanography*, *52*(4), 1367–1379. https://doi.org/10.4319/lo.2007.52.4.1367

Dror, T., Lehahn, Y., Altaratz, O., & Koren, I. (2018). Temporal□Scale Analysis of Environmental Controls on Sea Spray Aerosol Production Over the South Pacific Gyre. *Geophysical Research Letters*, *45*(16), 8637–8646. https://doi.org/10.1029/2018GL078707

Ducklow, H., Fraser, W., Meredith, M., Stammerjohn, S., Doney, S., Martinson, D., … Amsler, C. (2013). West Antarctic Peninsula: An Ice-Dependent Coastal Marine Ecosystem in Transition. *Oceanography*, *26*(3), 190–203. https://doi.org/10.5670/oceanog.2013.62

Dunne, J. P., Bociu, I., Bronselaer, B., Guo, H., John, J. G., Krasting, J. P., … Zadeh, N. (2020). Simple Global Ocean Biogeochemistry With Light, Iron, Nutrients and Gas Version 2 (BLINGv2): Model Description and Simulation Characteristics in GFDL's CM4.0. *Journal of Advances in Modeling Earth Systems*, *12*(10). https://doi.org/10.1029/2019MS002008

Eayrs, C., Li, X., Raphael, M. N., & Holland, D. M. (2021). Rapid decline in Antarctic sea ice in recent years hints at future change. *Nature Geoscience*, *14*(7), 460–464. https://doi.org/10.1038/s41561-021-00768-3

Feng, L., & Hu, C. (2016). Comparison of Valid Ocean Observations Between MODIS Terra and Aqua Over the Global Oceans. *IEEE Transactions on Geoscience and Remote Sensing*, *54*(3), 1575–1585. https://doi.org/10.1109/TGRS.2015.2483500

Fitzgerald, J. W. (1991). Marine aerosols: A review. *Atmospheric Environment. Part A. General Topics*, *25*(3–4), 533–545. https://doi.org/10.1016/0960-1686(91)90050-H

Forestieri, S. D., Moore, K. A., Martinez Borrero, R., Wang, A., Stokes, M. D., & Cappa, C. D. (2018). Temperature and Composition Dependence of Sea Spray Aerosol Production. *Geophysical Research Letters*, *45*(14), 7218–7225. https://doi.org/10.1029/2018GL078193

Franklin, C. A. (Ed.). (2007). *Guidelines for assessment and instruction in statistics education (GAISE) report: A pre-K-12 curriculum framework*. Alexandria, VA: American Statistical Association.

Fuentes, E., Coe, H., Green, D., de Leeuw, G., & McFiggans, G. (2010). On the impacts of phytoplankton-derived organic matter on the properties of the primary marine aerosol – Part 1: Source fluxes. *Atmospheric Chemistry and Physics*, *10*(19), 9295–9317. https://doi.org/10.5194/acp-10-9295-2010

Gabric, A. J., Matrai, P., Jones, G., & Middleton, J. (2018). The Nexus between Sea Ice and Polar Emissions of Marine Biogenic Aerosols. *Bulletin of the American Meteorological Society*, *99*(1), 61–81. https://doi.org/10.1175/BAMS-D-16-0254.1

Gabric, A. J., Shephard, J. M., Knight, J. M., Jones, G., & Trevena, A. J. (2005). Correlations between the satellite-derived seasonal cycles of phytoplankton biomass and aerosol optical depth in the Southern Ocean: Evidence for the influence of sea ice: CORRELATIONS BETWEEN CHL AND AOD IN SOUTHERN OCEAN. *Global Biogeochemical Cycles*, *19*(4), n/a-n/a. https://doi.org/10.1029/2005GB002546

Galindo, V., Levasseur, M., Mundy, C. J., Gosselin, M., Tremblay, J.-É., Scarratt, M., … Lizotte, M. (2014). Biological and physical processes influencing sea ice, under-ice algae, and dimethylsulfoniopropionate during spring in the Canadian Arctic Archipelago. *Journal of Geophysical Research: Oceans*, *119*(6), 3746–3766. https://doi.org/10.1002/2013JC009497

Galindo, Virginie, Levasseur, M., Mundy, C. J., Gosselin, M., Scarratt, M., Papakyriakou, T., … Lizotte, M. (2016). Contrasted sensitivity of DMSP production to high light exposure in two Arctic under-ice blooms. *Journal of Experimental Marine Biology and Ecology*, *475*, 38–48. https://doi.org/10.1016/j.jembe.2015.11.009

Gao, Y. (2003). Aeolian iron input to the ocean through precipitation scavenging: A modeling perspective and its implication for natural iron fertilization in the ocean. *Journal of Geophysical Research*, *108*(D7), 4221. https://doi.org/10.1029/2002JD002420

Getzewich, B. J., Vaughan, M. A., Hunt, W. H., Avery, M. A., Powell, K. A., Tackett, J. L., … Toth, T. D. (2018). CALIPSO lidar calibration at 532 nm: Version 4 daytime algorithm. *Atmospheric Measurement Techniques*, *11*(11), 6309–6326. https://doi.org/10.5194/amt-11-6309-2018

Grythe, H., Ström, J., Krejci, R., Quinn, P., & Stohl, A. (2014). A review of sea-spray aerosol source functions using a large global set of sea salt aerosol concentration measurements. *Atmospheric Chemistry and Physics*, *14*(3), 1277–1297. https://doi.org/10.5194/acp-14-1277-2014

Holland, P. R., & Kwok, R. (2012). Wind-driven trends in Antarctic sea-ice drift. *Nature Geoscience*, *5*(12), 872–875. https://doi.org/10.1038/ngeo1627

Jaeglé, L., Quinn, P. K., Bates, T. S., Alexander, B., & Lin, J.-T. (2011). Global distribution of sea salt aerosols: New constraints from in situ and remote sensing observations. *Atmospheric Chemistry and Physics*, *11*(7), 3137–3157. https://doi.org/10.5194/acp-11-3137-2011

Jarníková, T., & Tortell, P. D. (2016). Towards a revised climatology of summertime dimethylsulfide concentrations and sea–air fluxes in the Southern Ocean. *Environmental Chemistry*, *13*(2), 364. https://doi.org/10.1071/EN14272

Jena, B. (2017). The effect of phytoplankton pigment composition and packaging on the retrieval of chlorophyll-a concentration from satellite observations in the Southern Ocean. *International Journal of Remote Sensing*, *38*(13), 3763–3784. https://doi.org/10.1080/01431161.2017.1308034

Kaleschke, L. (2004). Frost flowers on sea ice as a source of sea salt and their influence on tropospheric halogen chemistry. *Geophysical Research Letters*, *31*(16), L16114. https://doi.org/10.1029/2004GL020655

Kar, J., Vaughan, M. A., Lee, K.-P., Tackett, J. L., Avery, M. A., Garnier, A., … Young, S. A. (2018). CALIPSO lidar calibration at 532 nm: Version 4 nighttime algorithm. *Atmospheric Measurement Techniques*, *11*(3), 1459–1479. https://doi.org/10.5194/amt-11-1459-2018

Kaufman, Y. J., Remer, L. A., Tanre, D., Rong-Rong Li, Kleidman, R., Mattoo, S., … Koren, I. (2005). A critical examination of the residual cloud contamination and diurnal sampling effects on MODIS estimates of aerosol over ocean. *IEEE Transactions on Geoscience and Remote Sensing*, *43*(12), 2886–2897. https://doi.org/10.1109/TGRS.2005.858430

Kim, M.-H., Kim, S.-W., Yoon, S.-C., & Omar, A. H. (2013). Comparison of aerosol optical depth between CALIOP and MODIS-Aqua for CALIOP aerosol subtypes over the ocean: AOD COMPARISON FOR CALIOP AEROSOL TYPES. *Journal of Geophysical Research: Atmospheres*, *118*(23), 13,241-13,252. https://doi.org/10.1002/2013JD019527

Kim, M.-H., Omar, A. H., Tackett, J. L., Vaughan, M. A., Winker, D. M., Trepte, C. R., … Magill, B. E. (2018). The CALIPSO version 4 automated aerosol classification and lidar ratio selection algorithm. *Atmospheric Measurement Techniques*, *11*(11), 6107–6135. https://doi.org/10.5194/amt-11-6107-2018

Kim, M.-H., Omar, A. H., Vaughan, M. A., Winker, D. M., Trepte, C. R., Hu, Y., … Kim, S.-W. (2017). Quantifying the low bias of CALIPSO's column aerosol optical depth due to undetected aerosol layers: Undetected Aerosols in CALIPSO AOD. *Journal of Geophysical Research: Atmospheres*, *122*(2), 1098–1113. https://doi.org/10.1002/2016JD025797

Kittaka, C., Winker, D. M., Vaughan, M. A., Omar, A., & Remer, L. A. (2011). Intercomparison of column aerosol optical depths from CALIPSO and MODIS-Aqua. *Atmospheric Measurement Techniques*, *4*(2), 131–141. https://doi.org/10.5194/amt-4-131-2011

Kleefeld, C. (2002). Relative contribution of submicron and supermicron particles to aerosol light scattering in the marine boundary layer. *Journal of Geophysical Research*, *107*(D19), 8103. https://doi.org/10.1029/2000JD000262

Koga, S., Nomura, D., & Wada, M. (2014). Variation of dimethylsulfide mixing ratio over the Southern Ocean from 36°S to 70°S. *Polar Science*, *8*(3), 306–313. https://doi.org/10.1016/j.polar.2014.04.002

Kroll, J. H., & Seinfeld, J. H. (2008). Chemistry of secondary organic aerosol: Formation and evolution of low-volatility organics in the atmosphere. *Atmospheric Environment*, *42*(16), 3593–3624. https://doi.org/10.1016/j.atmosenv.2008.01.003

Lannuzel, D., Tedesco, L., van Leeuwe, M., Campbell, K., Flores, H., Delille, B., … Wongpan, P. (2020). The future of Arctic sea-ice biogeochemistry and ice-associated ecosystems. *Nature Climate Change*, *10*(11), 983–992. https://doi.org/10.1038/s41558-020-00940-4

Leck, C., & Bigg, E. K. (2005). Biogenic particles in the surface microlayer and overlaying atmosphere in the central Arctic Ocean during summer. *Tellus B: Chemical and Physical Meteorology*, *57*(4), 305–316. https://doi.org/10.3402/tellusb.v57i4.16546

Leck, C., Tjernström, M., Matrai, P., Swietlicki, E., & Bigg, K. (2004). Can marine micro-organisms influence melting of the Arctic pack ice? *Eos, Transactions American Geophysical Union*, *85*(3), 25. https://doi.org/10.1029/2004EO030001

Leeuwe, M. A., Webb, A. L., Venables, H. J., Visser, R. J. W., Meredith, M. P., Elzenga, J. T. M., & Stefels, J. (2020). Annual patterns in phytoplankton phenology in Antarctic coastal

waters explained by environmental drivers. *Limnology and Oceanography*, lno.11477. https://doi.org/10.1002/lno.11477

Levy, R. C., Mattoo, S., Munchak, L. A., Remer, L. A., Sayer, A. M., Patadia, F., & Hsu, N. C. (2013). The Collection 6 MODIS aerosol products over land and ocean. *Atmospheric Measurement Techniques*, *6*(11), 2989–3034. https://doi.org/10.5194/amt-6-2989-2013

Lewis, R., & Schwartz, E. (2004). *Sea Salt Aerosol Production: Mechanisms, Methods, Measurements and Models—A Critical Review*. Washington, D. C.: American Geophysical Union. https://doi.org/10.1029/GM152

Li, F., Ginoux, P., & Ramaswamy, V. (2010). Transport of Patagonian dust to Antarctica. *Journal of Geophysical Research*, *115*(D18), D18217. https://doi.org/10.1029/2009JD012356

Li, Y., Ji, R., Jenouvrier, S., Jin, M., & Stroeve, J. (2016). Synchronicity between ice retreat and phytoplankton bloom in circum-Antarctic polynyas: Synchronicity of Ice Retreat and Bloom. *Geophysical Research Letters*, *43*(5), 2086–2093. https://doi.org/10.1002/2016GL067937

Liss, P. S., Broadgate, W. J., Hatton, A. D., Little, R. H., Malin, G., McArdle, N. C., … Turner, S. M. (2000). Biological Production of Trace Gases in Surface Sea Water and their Emission to the Atmosphere. In S. E. Larsen, F. Fiedler, & P. Borrell (Eds.), *Exchange*

and Transport of Air Pollutants over Complex Terrain and the Sea (pp. 139–144). Berlin, Heidelberg: Springer Berlin Heidelberg. https://doi.org/10.1007/978-3-642-57252-4_18

Liu, J., Dedrick, J., Russell, L. M., Senum, G. I., Uin, J., Kuang, C., … Lubin, D. (2018). High summertime aerosol organic functional group concentrations from marine and seabird sources at Ross Island, Antarctica, during AWARE. *Atmospheric Chemistry and Physics*, *18*(12), 8571–8587. https://doi.org/10.5194/acp-18-8571-2018

Liu, S., Liu, C.-C., Froyd, K. D., Schill, G. P., Murphy, D. M., Bui, T. P., … Gao, R.-S. (2021). Sea spray aerosol concentration modulated by sea surface temperature. *Proceedings of the National Academy of Sciences*, *118*(9), e2020583118. https://doi.org/10.1073/pnas.2020583118

Liu, Z., Kar, J., Zeng, S., Tackett, J., Vaughan, M., Avery, M., … Winker, D. (2019). Discriminating between clouds and aerosols in the CALIOP version 4.1 data products. *Atmospheric Measurement Techniques*, *12*(1), 703–734. https://doi.org/10.5194/amt-12-703-2019

Lu, X., Hu, Y., Liu, Z., Rodier, S., Vaughan, M., Lucker, P., … Pelon, J. (2017). Observations of Arctic snow and sea ice cover from CALIOP lidar measurements. *Remote Sensing of Environment*, *194*, 248–263. https://doi.org/10.1016/j.rse.2017.03.046

Lu, X., Hu, Y., Yang, Y., Bontempi, P., Omar, A., & Baize, R. (2020). Antarctic spring ice-edge blooms observed from space by ICESat-2. *Remote Sensing of Environment*, *245*, 111827. https://doi.org/10.1016/j.rse.2020.111827

Lu, X., Hu, Y., Yang, Y., Vaughan, M., Liu, Z., Rodier, S., … Trepte, C. (2018). Laser pulse bidirectional reflectance from CALIPSO mission. *Atmospheric Measurement Techniques*, *11*(6), 3281–3296. https://doi.org/10.5194/amt-11-3281-2018

Mazloff, M. R., Heimbach, P., & Wunsch, C. (2010). An Eddy-Permitting Southern Ocean State Estimate. *Journal of Physical Oceanography*, *40*(5), 880–899. https://doi.org/10.1175/2009JPO4236.1

McCoy, D. T., Burrows, S. M., Wood, R., Grosvenor, D. P., Elliott, S. M., Ma, P.-L., … Hartmann, D. L. (2015). Natural aerosols explain seasonal and spatial patterns of Southern Ocean cloud albedo. *Science Advances*, *1*(6), e1500157–e1500157. https://doi.org/10.1126/sciadv.1500157

Meehl, G. A., Arblaster, J. M., Chung, C. T. Y., Holland, M. M., DuVivier, A., Thompson, L., … Bitz, C. M. (2019). Sustained ocean changes contributed to sudden Antarctic sea ice retreat in late 2016. *Nature Communications*, *10*(1), 14. https://doi.org/10.1038/s41467-018-07865-9

Meredith, M. P., & King, J. C. (2005). Rapid climate change in the ocean west of the Antarctic Peninsula during the second half of the 20th century: RAPID OCEAN CLIMATE CHANGE AT THE WAP. *Geophysical Research Letters*, *32*(19), n/a-n/a. https://doi.org/10.1029/2005GL024042

Modini, R. L., Russell, L. M., Deane, G. B., & Stokes, M. D. (2013). Effect of soluble surfactant on bubble persistence and bubble-produced aerosol particles: SURFACTANT EFFECTS ON BUBBLE-PRODUCED PARTICLES. *Journal of Geophysical Research: Atmospheres*, *118*(3), 1388–1400. https://doi.org/10.1002/jgrd.50186

MODIS Atmosphere Science Team. (2017). *MYD08_D3 MODIS/Aqua Aerosol Cloud Water Vapor Ozone Daily L3 Global 1Deg CMG* [Data set]. NASA Level 1 and Atmosphere Archive and Distribution System. https://doi.org/10.5067/MODIS/MYD08_D3.061

NASA Ocean Biology Processing Group. (2017). *MODIS-Aqua Level 3 Mapped Chlorophyll Data Version R2018.0* [Data set]. NASA Ocean Biology DAAC. https://doi.org/10.5067/AQUA/MODIS/L3M/CHL/2018

O'Dowd, C. D., & de Leeuw, G. (2007). Marine aerosol production: A review of the current knowledge. *Philosophical Transactions of the Royal Society A: Mathematical, Physical and Engineering Sciences*, *365*(1856), 1753–1774. https://doi.org/10.1098/rsta.2007.2043

O'Dowd, C. D., Facchini, M. C., Cavalli, F., Ceburnis, D., Mircea, M., Decesari, S., … Putaud, J.-P. (2004). Biogenically driven organic contribution to marine aerosol. *Nature*, *431*(7009), 676–680. https://doi.org/10.1038/nature02959

Boucher, O., Randall, D., Artaxo, P., Bretherton, C., Feingold, G., Forster, P., … Zhang, X. (2013). 7. Clouds and Aerosols. In *Climate Change 2013: The Physical Science Basis. Contribution of Working Group I to the Fifth Assessment Report of the Intergovernmental Panel on Climate Change*. Cambridge University Press, Cambridge, United Kingdom and New York, NY, USA.

Omar, A. H., Winker, D. M., Tackett, J. L., Giles, D. M., Kar, J., Liu, Z., … Trepte, C. R. (2013). CALIOP and AERONET aerosol optical depth comparisons: One size fits none: CALIOP AND AERONET AOD: ONE SIZE FITS NONE. *Journal of Geophysical Research: Atmospheres*, *118*(10), 4748–4766. https://doi.org/10.1002/jgrd.50330

Orellana, M. V., Matrai, P. A., Leck, C., Rauschenberg, C. D., Lee, A. M., & Coz, E. (2011). Marine microgels as a source of cloud condensation nuclei in the high Arctic. *Proceedings of the National Academy of Sciences*, *108*(33), 13612–13617. https://doi.org/10.1073/pnas.1102457108

Parkinson, C. L. (2019). A 40-y record reveals gradual Antarctic sea ice increases followed by decreases at rates far exceeding the rates seen in the Arctic. *Proceedings of the National Academy of Sciences*, *116*(29), 14414–14423. https://doi.org/10.1073/pnas.1906556116

Perovich, D. K., & Richter-Menge, J. A. (1994). Surface characteristics of lead ice. *Journal of Geophysical Research*, *99*(C8), 16341. https://doi.org/10.1029/94JC01194

Rathke, C., Notholt, J., Fischer, J., & Herber, A. (2002). Properties of coastal Antarctic aerosol from combined FTIR spectrometer and sun photometer measurements: PROPERTIES OF COASTAL ANTARCTIC AEROSOL. *Geophysical Research Letters*, *29*(23), 46-1-46–4. https://doi.org/10.1029/2002GL015395

Redemann, J., Vaughan, M. A., Zhang, Q., Shinozuka, Y., Russell, P. B., Livingston, J. M., … Remer, L. A. (2012). The comparison of MODIS-Aqua (C5) and CALIOP (V2 & V3) aerosol optical depth. *Atmospheric Chemistry and Physics*, *12*(6), 3025–3043. https://doi.org/10.5194/acp-12-3025-2012

Remer, L. A., Kaufman, Y. J., Tanré, D., Mattoo, S., Chu, D. A., Martins, J. V., … Holben, B. N. (2005). The MODIS Aerosol Algorithm, Products, and Validation. *Journal of the Atmospheric Sciences*, *62*(4), 947–973. https://doi.org/10.1175/JAS3385.1

Rinaldi, M., Fuzzi, S., Decesari, S., Marullo, S., Santoleri, R., Provenzale, A., … Facchini, M. C. (2013). Is chlorophyll- *a* the best surrogate for organic matter enrichment in submicron primary marine aerosol?: CHLOROPHYLL AND OM IN FINE SEA SPRAY. *Journal of Geophysical Research: Atmospheres*, *118*(10), 4964–4973. https://doi.org/10.1002/jgrd.50417

Rogers, R. R., Vaughan, M. A., Hostetler, C. A., Burton, S. P., Ferrare, R. A., Young, S. A., … Winker, D. M. (2014). Looking through the haze: Evaluating the CALIPSO level 2 aerosol optical depth using airborne high spectral resolution lidar data. *Atmospheric Measurement Techniques*, *7*(12), 4317–4340. https://doi.org/10.5194/amt-7-4317-2014

Rozema, P. D., Venables, H. J., van de Poll, W. H., Clarke, A., Meredith, M. P., & Buma, A. G. J. (2017). Interannual variability in phytoplankton biomass and species composition in northern Marguerite Bay (West Antarctic Peninsula) is governed by both winter sea ice cover and summer stratification: Changing phytoplankton at the coastal WAP. *Limnology and Oceanography*, *62*(1), 235–252. https://doi.org/10.1002/lno.10391

Saba, G. K., Fraser, W. R., Saba, V. S., Iannuzzi, R. A., Coleman, K. E., Doney, S. C., … Schofield, O. M. (2014). Winter and spring controls on the summer food web of the coastal West Antarctic Peninsula. *Nature Communications*, *5*(1), 4318. https://doi.org/10.1038/ncomms5318

Saliba, G., Chen, C.-L., Lewis, S., Russell, L. M., Rivellini, L.-H., Lee, A. K. Y., … Behrenfeld, M. J. (2019). Factors driving the seasonal and hourly variability of sea-spray aerosol number in the North Atlantic. *Proceedings of the National Academy of Sciences*, *116*(41), 20309–20314. https://doi.org/10.1073/pnas.1907574116

Schlosser, E., Haumann, F. A., & Raphael, M. N. (2018). Atmospheric influences on the anomalous 2016 Antarctic sea ice decay. *The Cryosphere*, *12*(3), 1103–1119. https://doi.org/10.5194/tc-12-1103-2018

Schmale, J., Schneider, J., Nemitz, E., Tang, Y. S., Dragosits, U., Blackall, T. D., … Braban, C. F. (2013). Sub-Antarctic marine aerosol: Dominant contributions from biogenic sources. *Atmospheric Chemistry and Physics*, *13*(17), 8669–8694. https://doi.org/10.5194/acp-13-8669-2013

Schofield, O., Saba, G., Coleman, K., Carvalho, F., Couto, N., Ducklow, H., … Waite, N. (2017). Decadal variability in coastal phytoplankton community composition in a changing West Antarctic Peninsula. *Deep Sea Research Part I: Oceanographic Research Papers*, *124*, 42–54. https://doi.org/10.1016/j.dsr.2017.04.014

Schroeter, S., O'Kane, T. J., & Sandery, P. A. (2023). Antarctic sea ice regime shift associated with decreasing zonal symmetry in the Southern Annular Mode. *The Cryosphere*, *17*(2), 701–717. https://doi.org/10.5194/tc-17-701-2023

Schuster, G. L., Vaughan, M., MacDonnell, D., Su, W., Winker, D., Dubovik, O., … Trepte, C. (2012). Comparison of CALIPSO aerosol optical depth retrievals to AERONET measurements, and a climatology for the lidar ratio of dust. *Atmospheric Chemistry and Physics*, *12*(16), 7431–7452. https://doi.org/10.5194/acp-12-7431-2012

Sellegri, K., O'Dowd, C. D., Yoon, Y. J., Jennings, S. G., & de Leeuw, G. (2006). Surfactants and submicron sea spray generation. *Journal of Geophysical Research*, *111*(D22), D22215. https://doi.org/10.1029/2005JD006658

Sellegri, Karine, Gourdeau, J., Putaud, J.-P., & Despiau, S. (2001). Chemical composition of marine aerosol in a Mediterranean coastal zone during the FETCH experiment. *Journal of Geophysical Research: Atmospheres*, *106*(D11), 12023–12037. https://doi.org/10.1029/2000JD900629

Shepson, P., Matrai, P., Barrie, L., & Bottenheim, J. (2003). Ocean-atmosphere-sea ice-snowpack interactions in the Arctic, and global change. *Eos, Transactions American Geophysical Union*, *84*(36), 349–355. https://doi.org/10.1029/2003EO360002

Simmonds, I. (2015). Comparing and contrasting the behaviour of Arctic and Antarctic sea ice over the 35 year period 1979-2013. *Annals of Glaciology*, *56*(69), 18–28. https://doi.org/10.3189/2015AoG69A909

Stammerjohn, S., Massom, R., Rind, D., & Martinson, D. (2012). Regions of rapid sea ice change: An inter-hemispheric seasonal comparison: REGIONS OF RAPID SEA ICE CHANGE. *Geophysical Research Letters*, *39*(6), n/a-n/a. https://doi.org/10.1029/2012GL050874

Stefels, J., Steinke, M., Turner, S., Malin, G., & Belviso, S. (2007). Environmental constraints on the production and removal of the climatically active gas dimethylsulphide (DMS) and implications for ecosystem modelling. *Biogeochemistry*, *83*(1–3), 245–275. https://doi.org/10.1007/s10533-007-9091-5

Stuecker, M. F., Bitz, C. M., & Armour, K. C. (2017). Conditions leading to the unprecedented low Antarctic sea ice extent during the 2016 austral spring season: RECORD LOW 2016 ANTARCTIC SEA ICE EXTENT. *Geophysical Research Letters*, *44*(17), 9008–9019. https://doi.org/10.1002/2017GL074691

Sverdrup, H. U. (1953). On Conditions for the Vernal Blooming of Phytoplankton. *ICES Journal of Marine Science*, *18*(3), 287–295. https://doi.org/10.1093/icesjms/18.3.287

Tackett, J. L., Winker, D. M., Getzewich, B. J., Vaughan, M. A., Young, S. A., & Kar, J. (2018). CALIPSO lidar level 3 aerosol profile product: Version 3 algorithm design. *Atmospheric Measurement Techniques*, *11*(7), 4129–4152. https://doi.org/10.5194/amt-11-4129-2018

Thomas, D. N. (2002). Antarctic Sea Ice—A Habitat for Extremophiles. *Science*, *295*(5555), 641–644. https://doi.org/10.1126/science.1063391

Thomas, E. R., & Abram, N. J. (2016). Ice core reconstruction of sea ice change in the Amundsen-Ross Seas since 1702 A.D. *Geophysical Research Letters*, *43*(10), 5309–5317. https://doi.org/10.1002/2016GL068130

Thompson, D. W. J., Solomon, S., Kushner, P. J., England, M. H., Grise, K. M., & Karoly, D. J. (2011). Signatures of the Antarctic ozone hole in Southern Hemisphere surface climate change. *Nature Geoscience*, *4*(11), 741–749. https://doi.org/10.1038/ngeo1296

Tortell, P. D., Long, M. C., Payne, C. D., Alderkamp, A.-C., Dutrieux, P., & Arrigo, K. R. (2012). Spatial distribution of pCO2, ΔO2/Ar and dimethylsulfide (DMS) in polynya waters and the sea ice zone of the Amundsen Sea, Antarctica. *Deep Sea Research Part II: Topical Studies in Oceanography*, *71–76*, 77–93. https://doi.org/10.1016/j.dsr2.2012.03.010

Toth, T. D., Zhang, J., Campbell, J. R., Reid, J. S., Shi, Y., Johnson, R. S., … Winker, D. M. (2013). Investigating enhanced Aqua MODIS aerosol optical depth retrievals over the mid-to-high latitude Southern Oceans through intercomparison with co-located CALIOP, MAN, and AERONET data sets: ENHANCED AQUA MODIS SOUTHERN OCEANS AOD. *Journal of Geophysical Research: Atmospheres*, *118*(10), 4700–4714. https://doi.org/10.1002/jgrd.50311

Tremblay, J.-É., & Gagnon, J. (2009). The effects of irradiance and nutrient supply on the productivity of Arctic waters: A perspective on climate change. In J. C. J. Nihoul & A. G. Kostianoy (Eds.), *Influence of Climate Change on the Changing Arctic and Sub-Arctic Conditions* (pp. 73–93). Dordrecht: Springer Netherlands. https://doi.org/10.1007/978-1-4020-9460-6_7

Trevena, A. J. (2003). Profiles of dimethylsulphoniopropionate (DMSP), algal pigments, nutrients, and salinity in the fast ice of Prydz Bay, Antarctica. *Journal of Geophysical Research*, *108*(C5), 3145. https://doi.org/10.1029/2002JC001369

Trevena, A. J., & Jones, G. B. (2006). Dimethylsulphide and dimethylsulphoniopropionate in Antarctic sea ice and their release during sea ice melting. *Marine Chemistry*, *98*(2–4), 210–222. https://doi.org/10.1016/j.marchem.2005.09.005

Trevena & Jones. (2012). DMS flux over the Antarctic sea ice zone. *Mar. Chem.*, *134*, 47–58. https://doi.org/10.1016/j.marchem.2012.03.001

Turner, J., Colwell, S. R., Marshall, G. J., Lachlan-Cope, T. A., Carleton, A. M., Jones, P. D., … Iagovkina, S. (2005). Antarctic climate change during the last 50 years. *International Journal of Climatology*, *25*(3), 279–294. https://doi.org/10.1002/joc.1130

Turner, J., Holmes, C., Caton Harrison, T., Phillips, T., Jena, B., Reeves□Francois, T., … Bajish, C. C. (2022). Record Low Antarctic Sea Ice Cover in February 2022. *Geophysical Research Letters*, *49*(12). https://doi.org/10.1029/2022GL098904

Turner, J., Hosking, J. S., Bracegirdle, T. J., Marshall, G. J., & Phillips, T. (2015). Recent changes in Antarctic Sea Ice. *Philosophical Transactions of the Royal Society A: Mathematical, Physical and Engineering Sciences*, *373*(2045), 20140163. https://doi.org/10.1098/rsta.2014.0163

Turner, J., Maksym, T., Phillips, T., Marshall, G. J., & Meredith, M. P. (2013). The impact of changes in sea ice advance on the large winter warming on the western Antarctic

Peninsula. *International Journal of Climatology*, *33*(4), 852–861. https://doi.org/10.1002/joc.3474

Turner, J., Phillips, T., Marshall, G. J., Hosking, J. S., Pope, J. O., Bracegirdle, T. J., & Deb, P. (2017). Unprecedented springtime retreat of Antarctic sea ice in 2016: The 2016 Antarctic Sea Ice Retreat. *Geophysical Research Letters*, *44*(13), 6868–6875. https://doi.org/10.1002/2017GL073656

Vaughan, M., Garnier, A., Josset, D., Avery, M., Lee, K.-P., Liu, Z., … Rodier, S. (2019). CALIPSO lidar calibration at 1064 nm: Version 4 algorithm. *Atmospheric Measurement Techniques*, *12*(1), 51–82. https://doi.org/10.5194/amt-12-51-2019

Verdy, A., & Mazloff, M. R. (2017). A data assimilating model for estimating Southern Ocean biogeochemistry: SOUTHERN OCEAN BIOGEOCHEMISTRY ESTIMATE. *Journal of Geophysical Research: Oceans*, *122*(9), 6968–6988. https://doi.org/10.1002/2016JC012650

Webb, A. L., van Leeuwe, M. A., den Os, D., Meredith, M. P., J. Venables, H., & Stefels, J. (2019). Extreme spikes in DMS flux double estimates of biogenic sulfur export from the Antarctic coastal zone to the atmosphere. *Scientific Reports*, *9*(1), 2233. https://doi.org/10.1038/s41598-019-38714-4

Weber, R. J., McMurry, P. H., Mauldin, L., Tanner, D. J., Eisele, F. L., Brechtel, F. J., … Baumgardner, D. (1998). A study of new particle formation and growth involving biogenic and trace gas species measured during ACE 1. *Journal of Geophysical Research: Atmospheres*, *103*(D13), 16385–16396. https://doi.org/10.1029/97JD02465

Weng, Q. (Ed.). (2011). Forest Change Analysis Using Time-Series Landsat Observations. In *Advances in Environmental Remote Sensing* (0 ed., pp. 339–366). CRC Press. https://doi.org/10.1201/b10599-22

Winker, D. (2018). *CALIPSO Lidar Level 2 Aerosol Profile Data V4-20* [Data set]. NASA Langley Atmospheric Science Data Center DAAC. https://doi.org/10.5067/CALIOP/CALIPSO/LID_L2_05KMAPRO-STANDARD-V4-20

Xu, L., Russell, L. M., & Burrows, S. M. (2016). Potential sea salt aerosol sources from frost flowers in the pan-Arctic region: SALT AEROSOL SOURCES FROM FROST FLOWERS. *Journal of Geophysical Research: Atmospheres*, *121*(18), 10,840-10,856. https://doi.org/10.1002/2015JD024713

Young, S. A., Vaughan, M. A., Garnier, A., Tackett, J. L., Lambeth, J. D., & Powell, K. A. (2018). Extinction and optical depth retrievals for CALIPSO's Version 4 data release. *Atmospheric Measurement Techniques*, *11*(10), 5701–5727. https://doi.org/10.5194/amt-11-5701-2018

Zemmelink, H. J., Dacey, J. W. H., Houghton, L., Hintsa, E. J., & Liss, P. S. (2008). Dimethylsulfide emissions over the multi-year ice of the western Weddell Sea. *Geophysical Research Letters*, *35*(6), L06603. https://doi.org/10.1029/2007GL031847

Zhang, M., Chen, L., Xu, G., Lin, Q., & Liang, M. (2015). Linking Phytoplankton Activity in Polynyas and Sulfur Aerosols over Zhongshan Station, East Antarctica. *Journal of the Atmospheric Sciences*, *72*(12), 4629–4642. https://doi.org/10.1175/JAS-D-15-0094.1

APPENDICES

Chapter 1 Supporting Information

This document gives further information on the calculation of marine aerosol optical depth (MAOD) (Appendix Chapter 1 Section S1.1) as well as the number of observations averaged across in constructing each final seasonally averaged pixel in the seasonal arrays of MAOD, ice, and wind speed (Appendix Chapter 1 Section S1.2, Figures S1.2, S1.3, & S1.4). We further discuss the construction of a monthly-averaged time series (Figure S1.5) and temporal trends in chl-a, sea ice, and wind speed across the multi-year record as well as seasonal spatial trends of wind speed (Figure S1.6) in Appendix Chapter 1 Sections S2 & S3. Spatial Correlation figures between marine aerosol optical depth (MAOD), chlorophyll-*a* (chl-*a*), ice, and wind speed are also included. These show the spatial correlation between MAOD & chl-*a* concentration (Figure S1.7) and MAOD & wind speed (Figure S1.8). Seasonal spatial correlation figures given a null model with randomly generated numbers are also included as discussed in section 2.2.4 (Figure S1.9, S1.10, S1.11, & S1.12, multiple comparison plot S13). The pairwise comparison table alongside p-values is also presented (Table S1.1). Methods in retrieval and analysis of wind speed data are further discussed in Section 2.1, Satellite Data Retrieval & Computation. Methods in the calculation of spatial correlations are further discussed in Section 2.2.4, Spatial Correlation Calculation.

S1 Calculation of MAOD

S1.1Encompassing of Marine Aerosol Layer

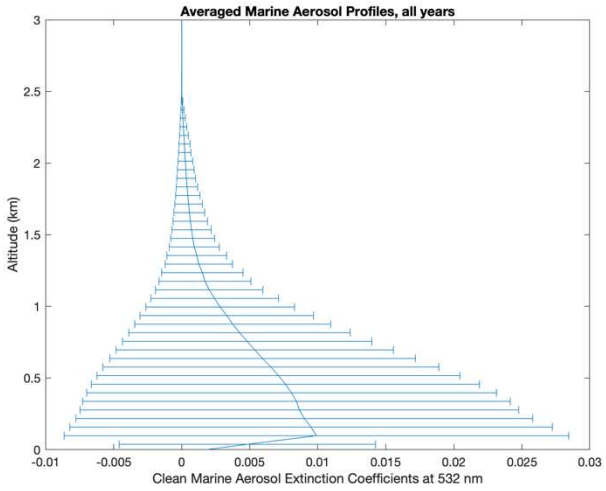

In Chapter 1 section 2.1 we define the calculation of MAOD as the trapezoidal integration of clean marine aerosol extinction across roughly sea level to 2 km across seasons. This is further visualized in Figure S1, in which quality-screened clean marine aerosol extinction coefficients across the spatiotemporal record from June 2006 to December 2018 are averaged with NaNs omitted. Error bars correspond to the mean absolute deviations, defined in Section 2.2.1, of extinction coefficients across each altitude range bin and exhibit the large spread of extinction coefficients across these altitudes. As such, the bulk of the signal is visualized from roughly sea level to 2km, leading to the calculation of MAOD as described in section 2.1.

S1.2 Construction of seasonal arrays of MAOD, ice, and wind speed

S1.2.1 Seasonally averaged pixels of MAOD, ice, and wind speed

The number of profiles used in constructing each final seasonally averaged pixel in MAOD, ice, and wind speed seasonal arrays are visualized in Figures S2, S3, and S4. With the exception of summertime MAOD, most pixels have > 20 observations in constructing seasonal averages.

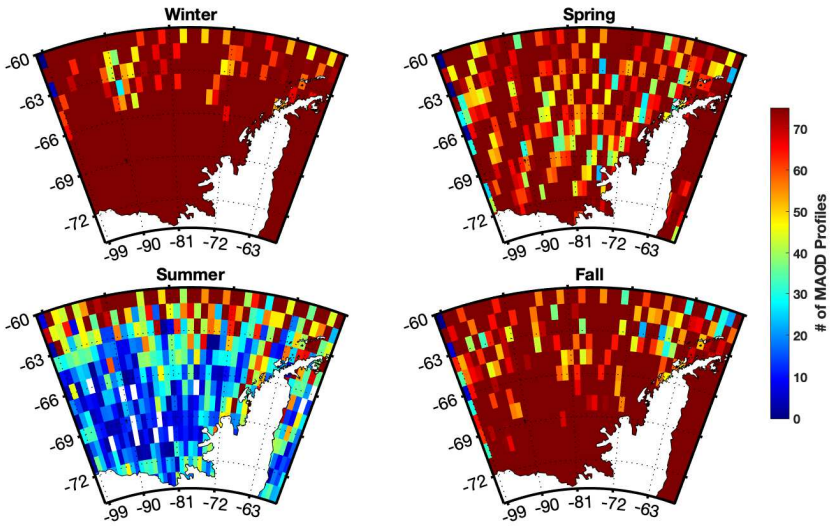

Figure S1.2. The number of MAOD profiles used in computing seasonal averages. As only nighttime quality-screened extinction coefficients are used in the derivation of MAOD, the summertime array exhibits the paucity of samples. Nevertheless, seasonal trends are observed across winter, spring, and fall, and seasonal trends are also observed using temporal analyses in this study.

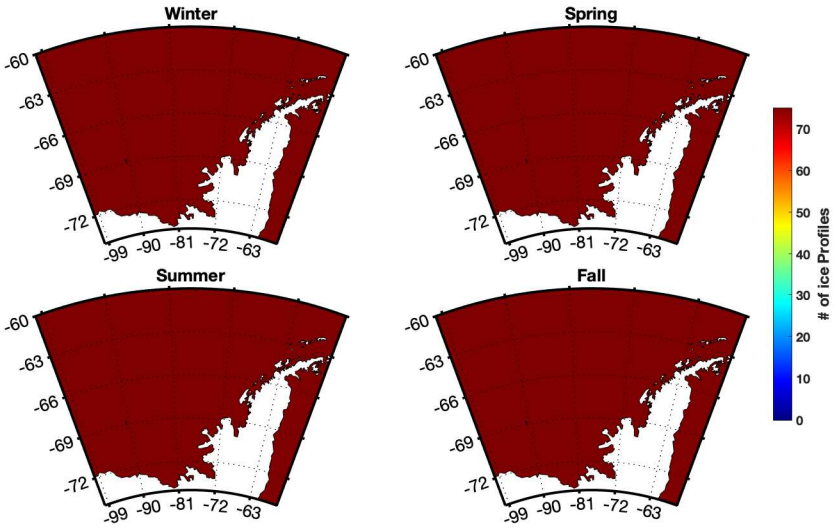

Figure S1.3. The number of depolarization ratio profiles used in computing seasonal sea ice averages.

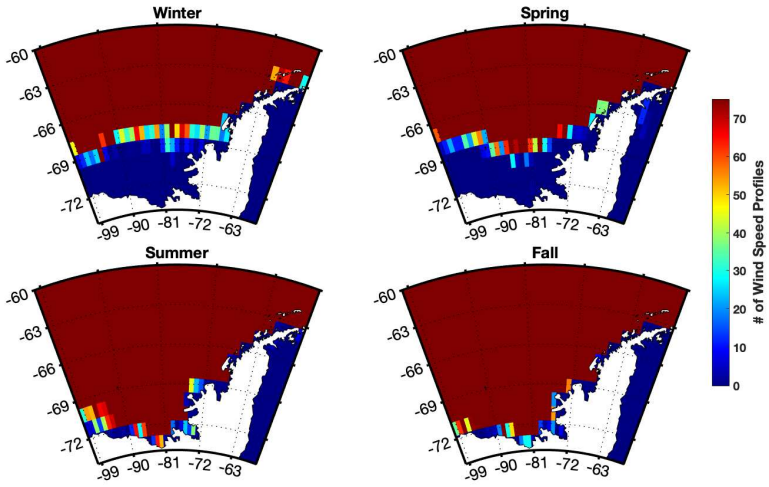

Figure S1.4. The number of wind speed observations used in computing seasonal averages. Missing data corresponds to ice presence, also observed in the wind speed climatology, figure S1.6.

S2 Monthly climatological construction and trends in MAOD, chl-*a*, and ice

Monthly-averaged climatology time-series of MAOD, ice, and wind speed were constructed by averaging all profiles for each month across the entire spatiotemporal range of analysis. Time-series of chl-*a* were constructed by subdividing the Level 3 (4 x 4 km^2) mapped data products and temporally averaging across each month.

The monthly climatology of MAOD exhibits much of the same variability as observed in the multi-year time-series (Figure 2). MAOD reaches a minimum in March (~0.024 ± 0.006), which persists until October (~0.026 ± 0.009). MAOD then begins to increase in late spring reaching a maximum in the summer in December (~0.078 ± 0.018). These maxima decrease rapidly in late summer. Interestingly, the late winter to early spring pulse that precedes the summertime maxima does not occur as distinctly in the monthly climatology. The climatological monthly average for September (~0.028 ± 0.009) exceeds the August (~0.023 ± 0.008) and October (~0.026 ± 0.009) averages. This record indicates that the late spring pulse in MAOD is a consistent feature across the temporal extent of our analysis. Nevertheless, the overlap in the MAD indicates that this late spring MAOD peak is less distinct in the monthly climatology than the multi-year time-series, signifying the temporal variability in occurrence (July to September) and smoothing of the monthly average.

Annual temporal trends of chl-a are also visualized when considering the monthly climatology (Figure 2). An increase in chl-*a* begins in September leading to a maximum in January, followed by a decrease in late summer into fall (March to May). Summertime chl-*a* (~0.24 ± 0.21 mg m^{-3}) is greater than springtime (~0.05 ± 0.03 mg m^{-3}) by approximately a factor of 5 (Figure 2). The high MAD relative to the mean represents the large spread of these data

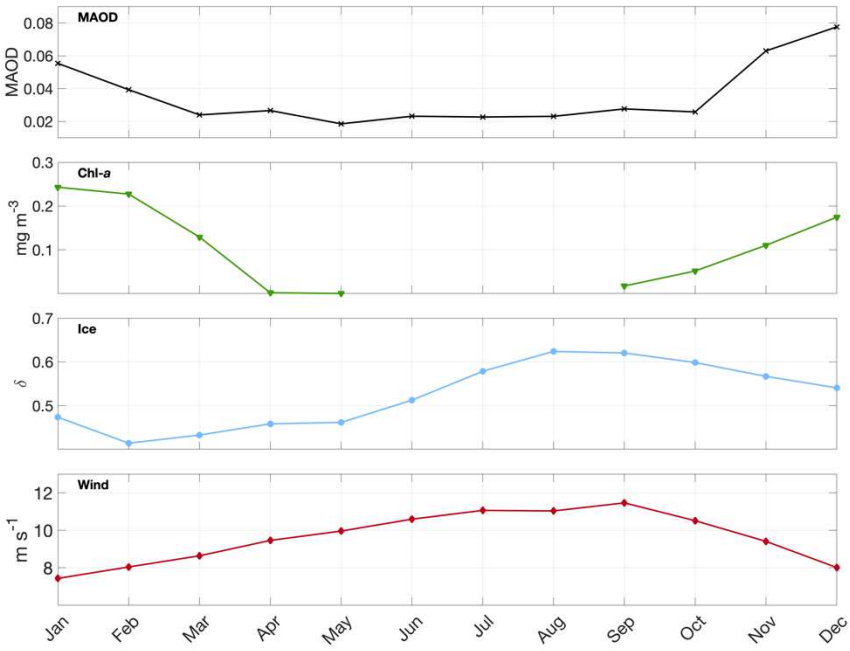

Figure S1.5. Monthly climatological time-series of MAOD, chl-*a*, ice, and wind speed across the entire temporal range of analysis from 2006 to 2018.

across spatiotemporal scales; nevertheless, trends that exist in the monthly time-series persist when averaged across each month, indicating the persistent annual seasonality of chl-*a*.

Monthly dynamics of sea ice evident in the multi-year time series are also present when examining the monthly climatology (Figure 2). As present in Figure 2, a maximum in ice occurs in winter from August to September with values of depolarization ratio equal to 0.62 ± 0.03 and 0.62 ± 0.05. Melt occurs from winter to early fall, with the minimum typically occurring in February with a value of 0.41 ± 0.03. As the WAP and southern Bellingshausen Sea exhibits the largest and fastest Antarctic sea ice decreases (Stammerjohn et al., 2012), we expect the monthly climatology to exhibit the lengthening of the summer ice-free region in the Bellingshausen Sea present in the multi-year time series over time.

S3 Spatiotemporal Trends of Chl-a, Sea Ice, and Wind Speed

S3.1 Seasonality of chl-*a*

Prior studies using both *in situ* and remote sensing techniques in the WAP andtheSouthern Ocean have also observed similar seasonality in chl-*a*. These works indicate that favorable conditions for the occurrence of the summertime chl-*a* max include an increased sea ice extent and duration in the preceding winter, declining summertime wind speed, and seasonal increase in light availability (Bowman et al., 2018). Although the timing of the minima and maxima in chl-*a* occurs across the same seasons in this multi-year record, the magnitudes exhibit notable variability. Mechanisms for variability in magnitude are numerous. For example, a high wintertime ice extent can cause buffering of the water column from high wind speeds, thus preventing the deepening of the winter mixed layer. Declining wind speeds in the summer can cause the persistence of a shallower mixed layer depth, and when these variables coincide with the seasonal summertime increase in light availability for primary production, a high summer maxima is observed (Saba et al., 2014). Similarly, high summertime winds or a shorter duration of the sea ice season along the marginal ice zone can lead to lower observed summertime chl-*a* max as the mixed layer depth is deeper, thereby inhibiting algal cells from overcoming light limitation (Schofield et al., 2017).

S3.2 Seasonality of sea ice

Our observations of multiyear dynamics of sea ice reflect prior studies of seasonal ice extent in the Arctic. Using CALIOP depolarization ratio, Lu et al. (2017) found seasonal fluctuations in ice cover with minimum values corresponding to late summer and maximum values corresponding to late winter and early spring. Those authors compared their results against passive microwave-based sea ice measurements, finding good agreement. To the best of our knowledge, our study is the first to use the CALIOP depolarization ratio to examine seasonal ice extent, melt, and freeze dynamics in the Southern Ocean. That the seasonal freeze and melt of ice exhibits variability is supported by prior studies indicating a significant lengthening of the summertime ice-free season from 1979/80 to 2012/13 (~92 days) in The Palmer Long-Term Ecological Research (LTER) study area, a United States Antarctic research station (Ducklow et al., 2013). In our study, the lengthening of the summer season is evident through the increase in the duration of the summertime sea ice or fast ice minima into autumn or fall (Figure 1c), also observed in Trevana & Jones (2006). Our results of the lengthening of the duration of the summertime ice-free season beyond 2011, as well as the record low ice year of 2017, are also supported in a study by Turner et al. (2017) that found Antarctic sea ice extent decreasing at a record rate of ~18% faster than prior years. Interestingly, in the spatial climatology, Figure XXX,

regional freezing in spring along occurs along the coastline north of ~68 °S. This is also exhibited in a study by Turner et al. (2013), who found that seasonal sea ice changes correspond with near-coastal changes, with a fall to winter elongated polynya-like feature extending from the northern tip of the peninsula to south of ~64ºS. This is likely associated with climate change induced regional-warming (Ducklow et al., 2013; Turner et al., 2013).

S3.3 Temporal Trends of Wind Speed

Wind speed exhibits seasonal variability across the temporal range of analysis (Figure 1d). The minima occur in the summertime (Dec – Jan) and the maxima occurs from winter to early spring (July – Sep). Variability across these seasonal trends exists. For example, wind speed is at a minimum in December 2012 of ~6.5 m/s. Following this minimum, wind speed increases until April to ~10.4 m/s. A decrease in wind speed of ~1.4 m/s occurs in late fall from April to May. From May onwards, wind speed increases until August 2013 to ~12.8 m/s. Following this wintertime maxima, wind speed began to decrease until the summertime minima in Dec 2013 of ~7.6 m/s, except for an increase of ~0.2 m/s from October to November 2013. Similar trends in wind speed are observed throughout the record: a minimum occurs in summer followed by a pulse in fall preceding the maximum in winter. Trends of an increase in wind speed in fall to winter before decreasing rapidly as summertime approaches are evident throughout this multi-year record.

Although seasonal patterns and temporal onset of the increase in wind speed are similar from one year to the next, the magnitude of the maxima and minima in wind speed exhibits variability. Some years, such as 2010 and 2011, had a maximum wind speed in June that was ~11.4 m/s. In other years, this maximum is higher: September 2017 had the highest wind speed on record, with a speed of ~14.5 m/s. Across this time series, the wintertime maxima in wind speed appears to increase from 2011 onwards, with many years exceeding the maximum wind speed in years prior from 2006 – 2011 of ~12.5 m/s in August 2008. The trend in the strengthening of winds is also shown in prior studies that examined drivers of ice cover in the WAP region. The strengthening of winds is considered to be the primary driver of the shortening of the winter ice season as the ice edge is driven southward, with the ice edge advance in fall becoming delayed and retreat in spring accelerated (Ducklow et al., 2013; Holland & Kwok, 2012). Although the timing of the minima, maxima, and increase and decrease in winds occurs across the same seasons in this multi-year record, the magnitude of wind speed thus exhibits variability, with ecosystem-wide effects taking place from the impact of wind-stress on sea-ice dynamics.

The monthly climatology of wind speed reflects averaged seasonal trends of increase and decrease in wind speed. Minimum values are observed in December – January and maximum values from July – September throughout the temporal range of record. Average wind speed in the winter minimum and summer maximum throughout the temporal range of analysis is ~7.4 m/s and ~11.5 m/s, respectively, indicating its seasonal variability.

S3.4 Spatial Trends of Wind Speed

Spatial climatologies of wind speed across the spatiotemporal range of this study reflect the time series with seasonal trends of highest wind speed in the winter and lowest wind speed in the summer (Figure S1). Missing data represents regions covered in ice. Wintertime winds range from ~8 m/s – 14 m/s. Values decrease from winter to spring, particularly in higher latitudes south of 66°S. Summertime wind speed exhibits lowest values across the spatial region of

analysis, and winds range from ~ 4 m/s – 10 m/s. Following the summertime minima, speed begins to increase in the fall from ~8 – 12 m/s. As shown in the timeseries, variability exists in different regions; for example, higher wind speeds occur south of 72°S in comparison to lower latitudes in the fall climatology. This is also shown in prior studies, and wind vectors appear to increase in the fall across the period from 1992 – 2010 in the WAP region in a study that linked wind stress to the delay in ice edge advance, thus causing the lengthening of the summer ice-free season (Holland & Kwok, 2012). Wind direction is important, with the strengthening of northerly winds and southward advection causing the freezing of ice to extend closer to the ice edge, delaying ice edge advance and lengthening the summer ice-free season. These same processes also accelerate ice retreat in the spring, advancing sea ice retreat (Ducklow et al., 2013; Stammerjohn et al., 2012). Prior studies have linked these changes to climate variability, and attribute strengthening of wind stress to the Southern Annular Mode and El Niño/Southern Oscillation. Modern trends in wind speed in this region can be due to natural variability, but may also be linked to anthropomorphic-induced changes such as the Southern Hemisphere ozone hole and

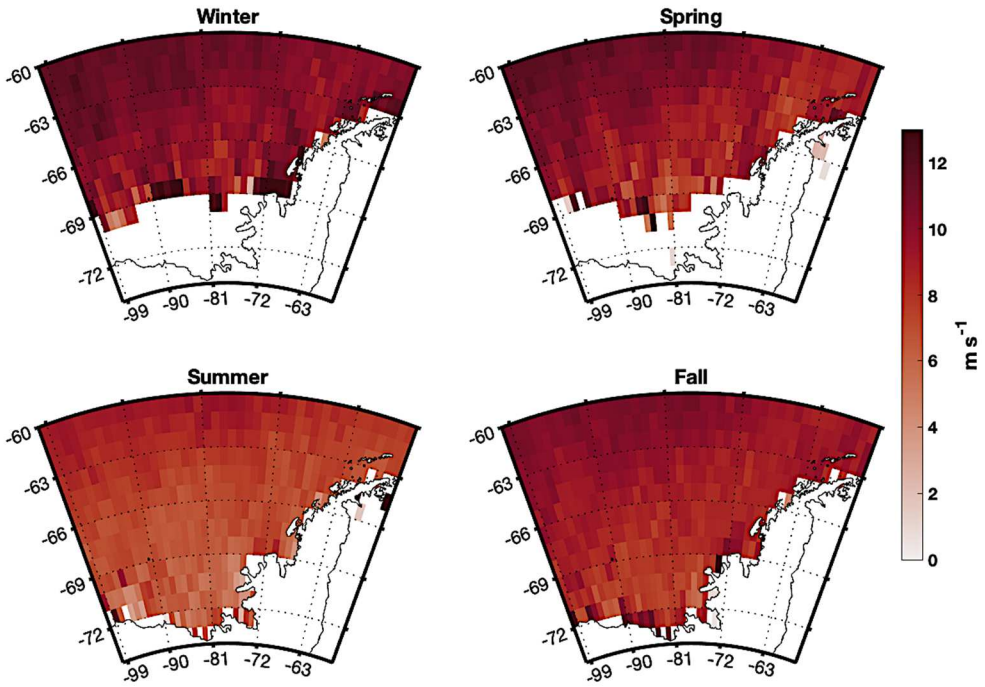

Figure S1.6. Seasonal climatology of wind speed. Missing data corresponds to sea-ice presence.

increased greenhouse gases causing significant change in surface climate (Thompson et al., 2011).

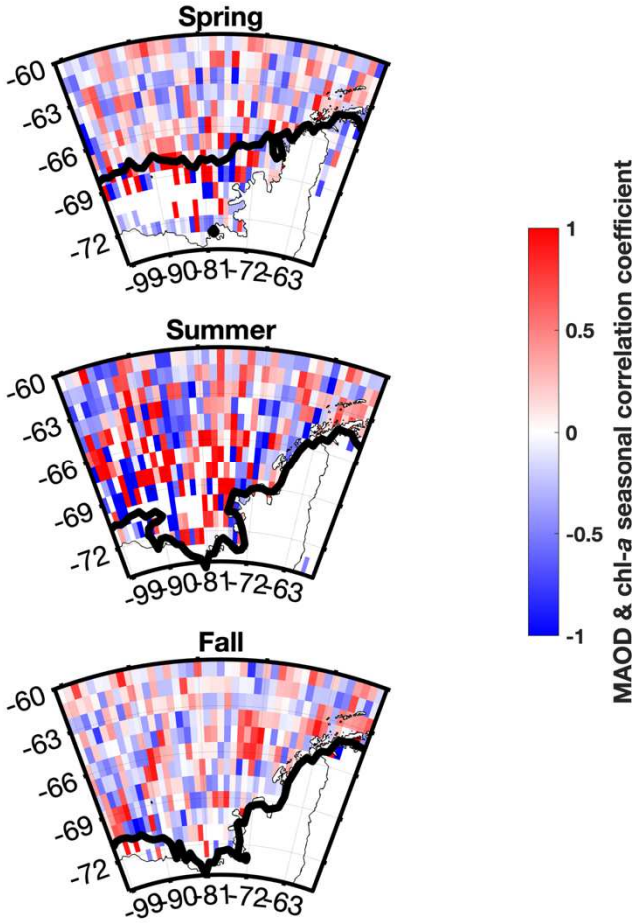

Figure S1.7. Seasonal correlation between MAOD and chl-*a*.

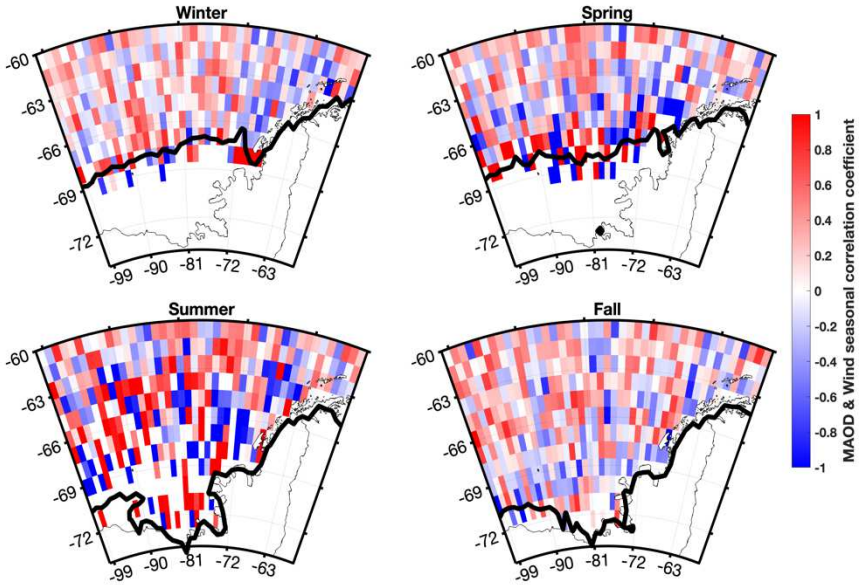

Figure S1.8. Seasonal correlation between MAOD and wind speed.

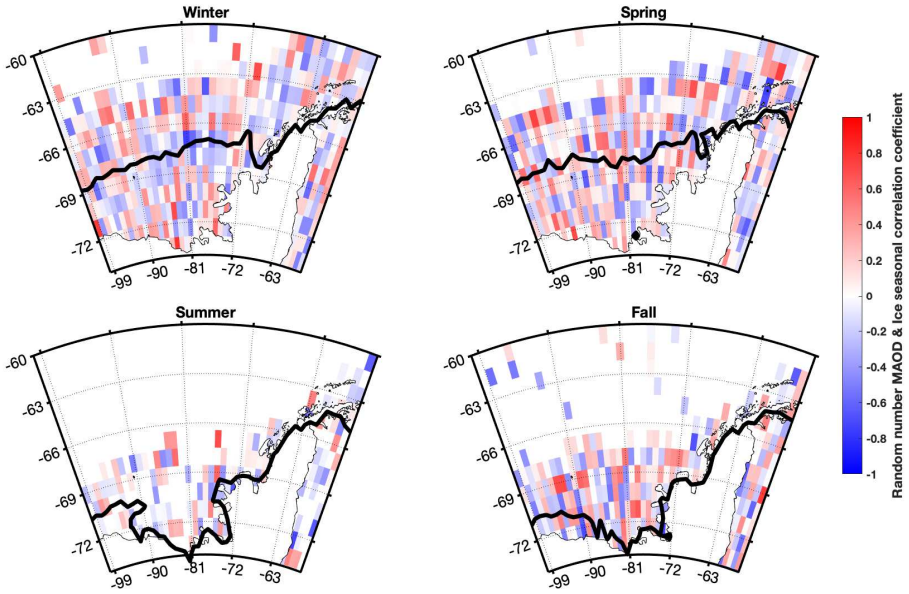

Figure S1.9. Seasonal correlation coefficients plotted given null model of randomly generated numbers for MAOD & ice.

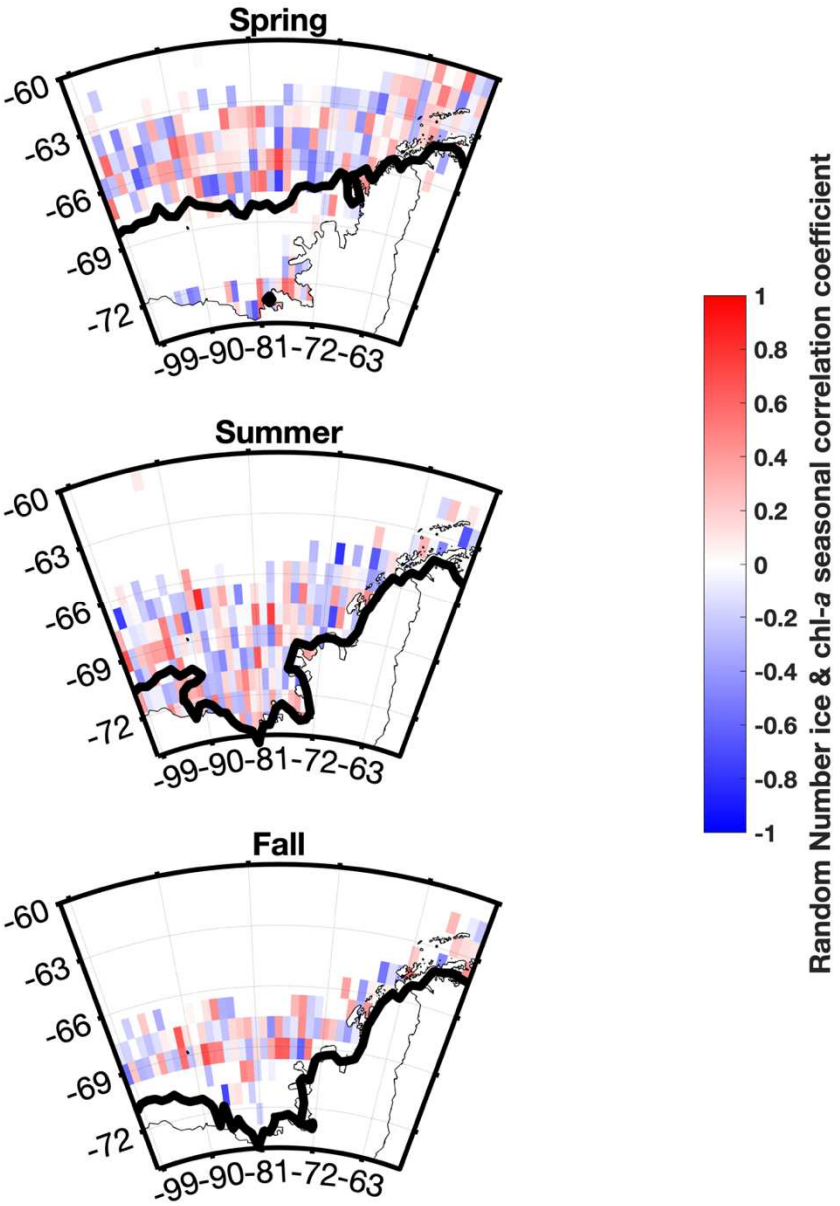

Figure S1.10. Seasonal correlation coefficients plotted given null model of randomly generated numbers for ice & chl-*a*.

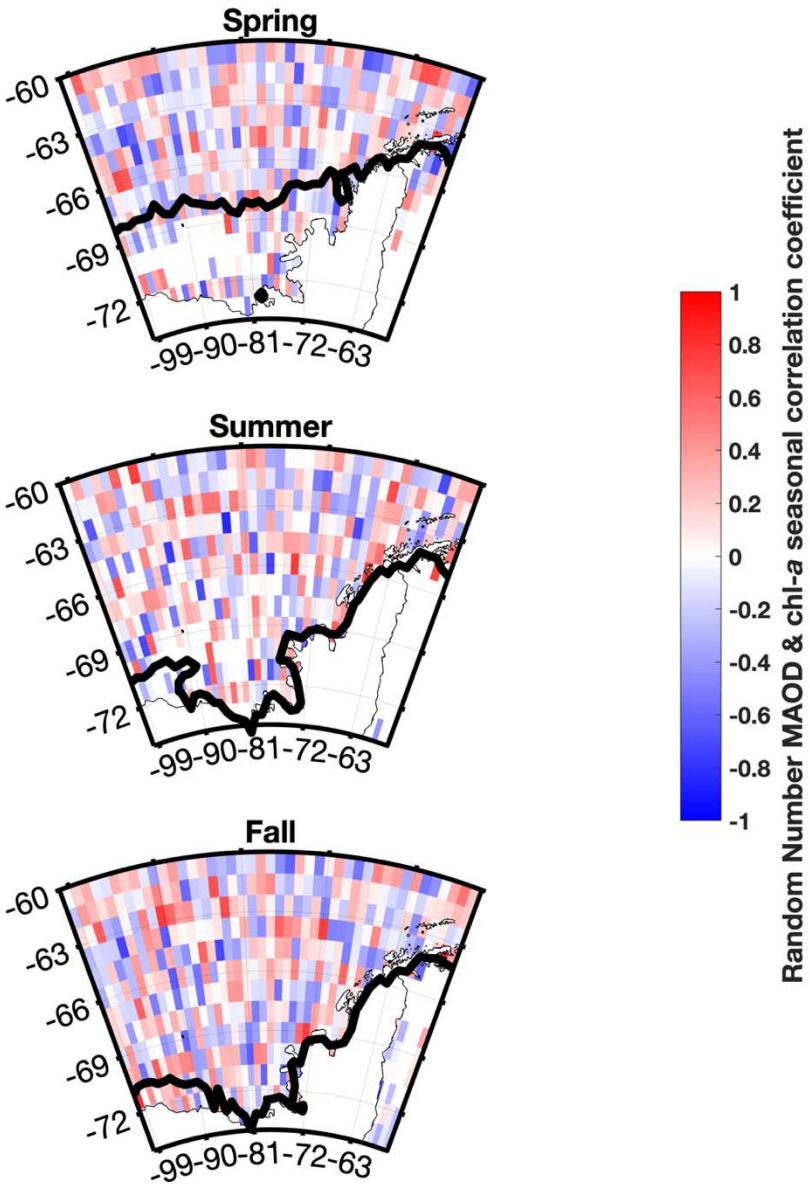

Figure S1.11. Seasonal correlation coefficients plotted given null model of randomly generated numbers for MAOD & chl-*a*.

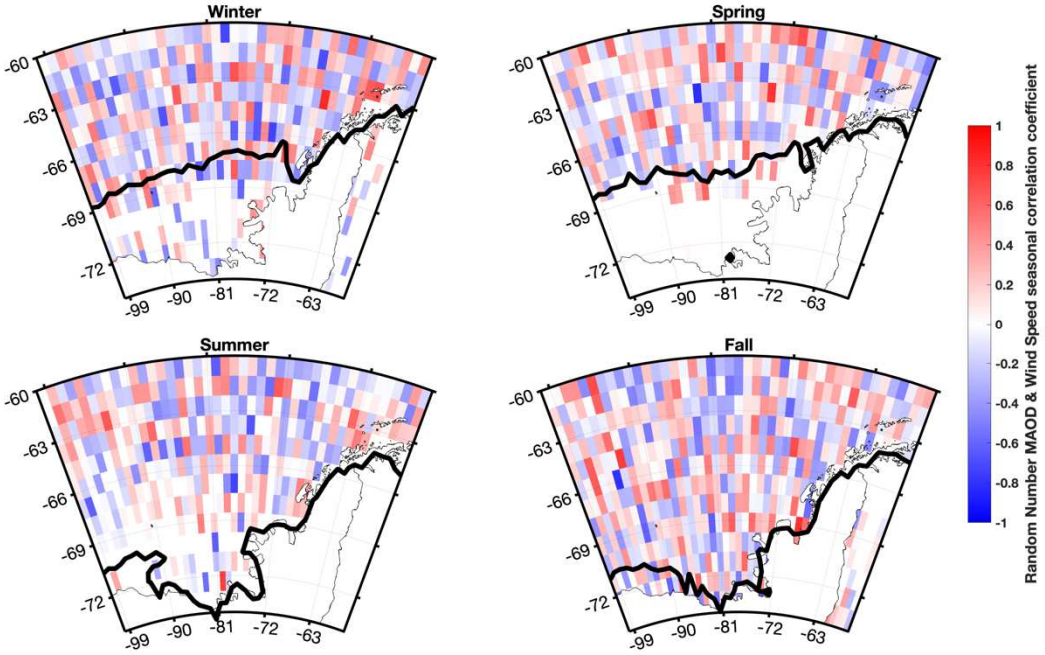

Figure S1.12. Seasonal correlation coefficients plotted given null model of randomly generated numbers for MAOD & wind speed.

Table S1.1
Pairwise comparison results from a multiple comparison test using Kruskal-Wallis.

Groups being compared	**Groups being compared**	**p-value**
Random MAOD & ice	MAOD & ice	4.8858e-06
Random ice & chl-a	ice & chl-a	6.3552e-08
Random MAOD & chl-a	MAOD & chl-a	0.9999
Random MAOD & wind speed	MAOD & wind speed	0.0027

Note. Using the Kruskal-Wallis test, all *p*-values are significant ($p < 0.05$) with the exception of the random model and MOD & chl-*a*.

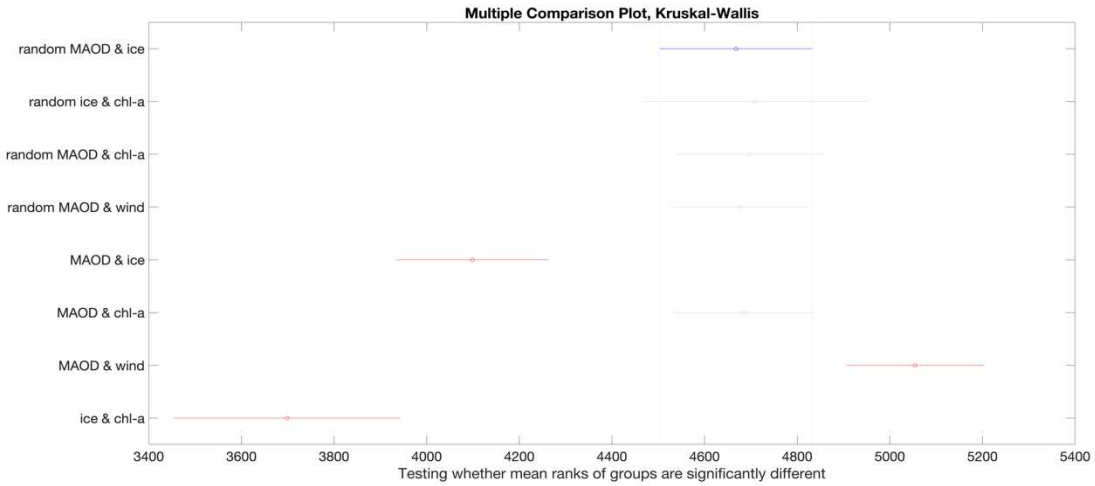

Figure S1.13. Multiple comparison plot using Kruskal-Wallis testing the null hypothesis that the spatial variable correlations come from the same population as the spatial correlations from the null model. With the exception of the random model against MOD & chl-*a*, all medians are

Chapter 2 Supporting Information

Introduction

This document further depicts Regions A, B, & C (Figure S2.1) and provides information on the calculation of marine aerosol optical depth (MAOD), coarse-mode aerosol optical depth (AOD_C), total-column aerosol optical depth (AOD_T), the fine-mode fraction of aerosol optical depth (AOD_f), chlorophyll-*a* concentration (chl-*a*), sea surface temperature (SST) wind speed, and sea ice (Appendix Chapter 2 Section S1). We include extended correlation analyses (Figures S2.2, S2.4 to S2.8, S10, and S11) and also include a discussion of spatiotemporal correlations across all regions on seasonal and annual scales (Appendix Chapter 2 Section S2, Figures S2.7 and S2.8). Daily means and standard deviations of all variables across all seasons across Regions A to C are reported in Tables S2.1 to S2.3, with statistical summaries of all analyses conducted presented in Tables S2.4 to S2.6.

S1 Methods for retrieving all satellite variables

Marine Aerosol Optical Depth (MAOD)

We calculated MAOD using methodology developed in Dasarathy et al. (2021). MAOD is derived from tropospheric clean marine aerosol retrievals from CALIOP onboard CALIPSO. Specifically, clean marine extinction coefficients at 532 nm were obtained from Level 2 5 km Aerosol Profile Products, version 4.20. These extinction coefficients were all derived from layers initially classified as clean marine tropospheric aerosol (Kim et al., 2018), with additional quality assurance screening applied (Tackett et al., 2018). Using these methods, only quality assured clean marine tropospheric aerosol extinction coefficient retrievals were used in calculating MAOD profiles. These extinction coefficients were integrated using trapezoidal integration across pre-specified altitude range bins from roughly sea level to 2 km to capture the bulk of the marine aerosol signal (Dasarathy et al., 2021). Due to the 60 m vertical sampling interval of CALIOP level 2 products, this corresponds to range bins of 0.0378 km to 2.0137 km. When sea ice presence is suspected, as determined by the lidar depolarization ratio, the lower altitude is moved upward by one range bin to 0.0977 km to avoid potential contamination of the atmospheric signal by ice protruding above the ocean surface. MAOD is therefore computed as:

$$\text{MAOD} = \int_{\mathbf{r_{surface}}}^{\mathbf{r_{top}}} \boldsymbol{\sigma_{cm}(r)dr} \quad (1)$$

Where $r_{surface}$ = 0.0378 km OR 0.0977 km, r_{top} = 2.0137 km, and $\sigma_{cm}(r)$ is the vertically resolved clean marine aerosol extinction coefficient. This altitude range was chosen as it most often captured the clean marine aerosol signal. Beginning the integration at 2.0137 km encompasses the marine boundary layer in all seasons. We further only examined nighttime and cloud-free MAOD profiles as in Dasarathy et al. (2021) and thereby avoid noise from solar background light (Toth et al., 2013).

The CALIOP backscatter signal alone is insufficient for discerning constituent components of detected aerosol layers; as such, MAOD is not a direct assessment of the biogenic aerosol species contributing to optical depth. Our derivation of MAOD from quality-screened and subtyped extinction coefficient profiles allows us to directly evaluate the vertical variability of aerosol in the marine boundary layer, which is especially relevant over the ocean where the aerosol source is the ocean itself. Furthermore, based on Mie scattering computations using representative size distributions for marine aerosols, measures of MAOD exhibit a substantial contribution by aerosols having radii less than 1 micron (Tackett, 2009). These contributions

decrease sharply for particles with radii below ~100 nm. As prior studies indicate bimodal distributions of biogenic aerosol species from 50 nm to 1 micron, which includes species such as NSS sulphate aerosol, nitrate, water-soluble organic carbon, and MSA derived from DMS (Brechtel et al., 1998; Cavalli, 2004; Rathke et al., 2002), MAOD is relevant for the analysis of biogenic aerosol distribution. Studies have also found seasonal cycles of sea spray production associated with the enrichment of primary organic aerosol (O'Dowd et al., 2004; Rinaldi et al., 2013). Our observations of trends in MAOD do not contradict these studies, as these primary organic aerosol particles are typically smaller in diameter than those which CALIOP is most sensitive to, having maximum diameters of about 200 nm (O'Dowd et al., 2004).

Coarse-mode Aerosol Optical Depth (AOD_C), total Aerosol Optical Depth (AOD_T), and fine-mode Aerosol Optical Depth (AOD_f)

Using similar methodology to Dror et al. (2018), AOD was derived from MODIS Aqua with a spatial resolution of 1 ° latitude x 1 ° longitude. These data have been extensively validated and are standard for MODIS over ocean products (Levy et al., 2013; Remer et al., 2005). The data set consisted of daily Level 3 total AOD (AOD_T) (retrieved at 550 nm) from the Collection 6.1 algorithm of MODIS aerosol products (MODIS Atmosphere Science Team, 2017) alongside standard deviations of AOD_T and pixel counts across spatial grid cells.
To calculate coarse-mode AOD (AOD_C), we retrieved the fine mode fraction (f_f), defined as the ratio between AOD contributed by small mode particles (radii <1 μm) and the total AOD (AOD_f/AOD_T), and therefore reflect the contribution of fine mode particles to the total aerosol extinction (Remer et al., 2005). Using methods from Dror et al. (2018), f_f was used to calculate AOD_C using $AOD_C = (1 - ff) \cdot AODT$. We thus obtained values of AOD_C and AOD_f (further validated by ascertaining that $AOD_C + AOD_f = AOD_T$).

As a balance between reducing noisy measurements while still maximizing available data in this high latitude region, we only retrieved AOD_C, AOD_T, and AOD_f values in any particular grid cell if the number of available AOD pixels (or retrievals) was > 2 (accomplished through the use of logical indexing with the reported Level 3 pixel counts). NaNs were omitted in the calculation of means of AOD_C, AOD_T, and AOD_f across seasons and across regions (Tables S2.1 to S2.3). NaNs were also omitted in the calculation of standard deviations of AOD_C and AOD_f. In contrast, standard deviations of AOD_T were calculated through averaging the provided Level 3 AOD_T standard deviations. We calculated the standard deviation means across regions and across seasons (Tables S2.1 to S2.3). Note that the standard deviations of AOD_T across seasons and regions is far lower in magnitude than the standard deviations of AOD_C and AOD_f. As AOD_C and AOD_f are calculated from AOD_T, this indicates the overall accuracy of AOD data used in this study.

As discussed in section 1, AOD_C has also been shown to be related to sea spray aerosol (SSA). SSA dominates the mass concentration of marine aerosol in remote oceanic regions, with the coarse mode (particles with radii > 1 μm) of aerosol composed mainly of SSA. Our rationale for use of both MAOD and AOD_C are that these data accomplish distinct, complementary tasks: a distinct advantage of MAOD is the retrieval of lower altitude marine aerosol particles with radii > ~100 nm. This high sensitivity to submicron aerosol, alongside the ability to examine a specified tropospheric altitude range (see Equation 1) and thereby limiting optical depth retrieval to the marine boundary layer, provides a distinct advantage for using MAOD and examining trends when the aerosol source is the ocean itself. Nevertheless, use of MAOD is not without its limitations: MAOD is a newly developed parameter with fewer comparisons available to support

its validation – used thus far solely in Dasarathy et al. (2021) – and is limited through examining solely nighttime profiles for reduction of noise; a distinct disadvantage in high-latitude polar regions in which seasonal summertime corresponds to total daylight. In contrast, AOD_C is limited in the ability to retrieve aerosol particles with radii > 1 μm, thereby restricting observations of trends of marine aerosol in remote regions as in the Bellingshausen Sea to only SSA, thereby possibly obscuring the observation of trends of NSS sulphate aerosol, nitrate, water-soluble organic carbon, and MSA with submicron diameters (Brechtel et al., 1998; Cavalli, 2004; Rathke et al., 2002). Nevertheless, as a passive sensor measurement, AOD_C corresponds to daytime retrievals, and in high-latitude regions such as the Bellingshausen Sea, use of AOD_C provides exceptional coverage of trends in seasonal summertime. Alongside this advantage is the easier accessibility and calculation of AOD_C through Level-1 and Atmosphere Archive & Distribution System (LAADS) Distributed Active Archive Center (DAAC), providing greater accessibility for users to examine trends in aerosol in any region of interest. Note the lack of direct correlations and significance in the relationship between MAOD & AOD_C present in Figure S2.2 across regions, further supporting differences in retrievals of marine aerosol between MAOD & AOD_C. To further visualize differences in the retrieval frequency and location we constructed the spatial plot (Figure S2.12) representing an average of 1 month of data (April 2012). Herein, AOD is visualized at the obtained Level 3 mapped spatial resolution of 1 ° latitude x 1 ° longitude. These daily data were averaged across 1 month in construction of this figure. MAOD is also averaged across the month of April 2012 and mapped by averaging these data across latitude longitude bins corresponding to 0.5 ° latitude x 0.5 ° longitude. The swaths of CALIPSO are thus visualized as the satellite transects the Bellingshausen Sea, distinct from the AOD Level 3 mapped product.

To further support our findings of trends in AOD_C across the Bellingshausen Sea, we also consider AOD_T and AOD_f across daily, seasonal, and annual scales to determine dependence on wind speed across regions (Figures S2.5 to S2.9, Tables S2.1 to S2.5). AOD_T is a more widely used metric and may be less uncertain than AOD_C, whereas AOD_f can consist of some submicron SSA but is more often dominated by other materials (Lewis & Schwartz, 2004). We thus performed concurrent analyses of AOD_T and AOD_f (Figures S5 to S9). When considering the daily variability of AOD_T and AOD_f in relation to daytime wind speed, we observed very weak ($R < 0.2$) positive correlations across all regions with significance ($p < 0.05$) in the coastal Region B (Figure S2.5, Table S2.4). In contrast, AOD_C had very weak ($R < 0.2$) significant ($p < 0.05$) correlations across all Regions (Figure 2.3, Table S2.4).

We also assessed the correlation between AOD_T and AOD_f to daytime winds in austral winter versus austral summer in Region A and found some seasonal differences (Figure S2.6, Table S2.4). For AOD_T, some seasonal differences emerged with summer exhibiting very weak ($R < 0.2$) significant ($p < 0.05$) correlations in contrast to winter. In Region B, due to the lack of wintertime data, we instead compared correlations between daytime winds in austral summer to austral spring and fall (Figure S2.6). AOD_T exhibited weak ($R = 0.2$-0.39) significant ($p < 0.05$) correlations in spring and fall and very weak ($R < 0.2$) significant ($p < 0.05$) correlations in the summer (Table S2.4). For AOD_f, there were no seasonal differences in the correlation to daytime wind speed in winter or summer in Region A. In Region B, some seasonal differences emerged with Fall exhibiting very weak ($R < 0.2$) significant ($p < 0.05$) correlations in contrast to spring and summer.

In addition to the daily correlations discussed above, we also investigated longer-term trends in AOD_T and AOD_f to daytime winds across seasonal and annual time scales (Figure S2.7

and S2.8, Table S2.5). While trends in the fit of the correlation emerged across all Regions, the correlations between AOD_T, AOD_f, and daytime wind speed was not significant for seasonal and annual time scales. Most notably, across all analyses of AOD_T and AOD_f, there exists no contradiction of findings of AOD_C. For statistical summaries of all AOD metrics, see Tables S2.1 to S2.6.

Chlorophyll-*a* Concentration (chl-a) & Sea Surface Temperature (SST)

Chl-*a* & SST concentrations were obtained from Level 3 (4 x 4 km^2) daily mapped data products across the spatiotemporal range specified. These mapped values were averaged for temporal analysis. As MODIS Aqua is a passive sensor that relies on ambient solar radiation from daytime conditions, we obtained averages apart from annual missing data. Computation of mean values across this region can be a potential source of error due to missing data caused by ice presence and cloud cover, as well as sun glint contamination which may affect the quality of retrievals (Feng & Hu, 2016). In calculation of the mean, missing values were excluded, thereby indicating the calculated mean values could be different than reality. Nevertheless, chl-*a* retrievals from MODIS Aqua may often underestimate true values in the Southern Ocean by a factor of 2 to 3, particularly when chl-*a* is greater than 0.3 mg m^{-3} (Jena, 2017).

Depolarization Ratio (sea ice)

Sea ice is examined using the CALIOP surface depolarization ratio as in Dasarathy et al. (2021) and Lu et al. (2017), with values consistent with passive microwave-based retrievals of sea ice (Lu et al., 2017). In brief, when the CALIPSO orbit transects surfaces covered by ice, whether land or ocean, digitizer saturation often occurs in both perpendicular and parallel 532 nm channels at the Earth's surface and altitudes immediately below (Lu et al., 2017). When the signals from these channels are ratioed, termed surface integrated depolarization ratio (δ), the resulting values are in the range of 0.65 to 1.1. Conversely, when CALIPSO transects surfaces covered by water, the signal intensity is substantially reduced, most especially in the perpendicular channel, and the resulting depolarization values are between 0.0 to 0.15. Sea ice was thus identified using the CALIOP surface depolarization ratio. Depolarization ratios were quality screened such that values ≤ -0.2 and > 1.2 were rejected from these analyses. Using thresholds from Lu et al. (2017), values less than 0.15 were taken to indicate open water, 0.15 to 0.65 indicated a mix between open water and sea ice (i.e., the marginal ice zone), and values greater than 0.65 indicated ice presence. To reduce uncertainty in MAOD and AOD that may arise from sea ice/snow cover, in all correlation analyses conducted, regions covered by sea ice and snow are excluded by masking corresponding values of MAOD and AOD as NaN across time steps. When the depolarization ratio was > 0.15, indicating a mix of water and ice presence, corresponding MAOD or AOD values are masked, thereby only using open ocean values of MAOD and AOD in all scatterplots.

Wind Speed

Wind speed (AMSR-E and AMSR-2) data are produced by Remote Sensing Systems and are available for download at https://www.remss.com/msissions/amsr/. These are the AMSR orbital data mapped to a 0.25° grid for day and night. Wind speed obtained at 10-m height above sea level was estimated from measurements taken by the Advanced Microwave Scanning Radiometer (AMSR). Medium-frequency products were used to determine wind speed at 10 m above the Earth's surface (units: m s^{-1}). Only physically plausible wind retrievals were used in

this analysis by filtering out wind speed ≤ 0 m s^{-1} and > 50 m s^{-1}, indicating data outside of valid ranges (Wentz et al., 2003). Daytime wind speeds were used in all correlation analyses with AOD (as AOD is a daytime measurement) and nighttime wind speeds were used in all correlation analyses with MAOD (as MAOD is a nighttime measurement).

Statistical Analysis

Pearson's correlation coefficient was used for regression analysis between AOD_C & wind speed and MAOD & wind speed across daily, seasonal, and annual time steps across all regions and seasons. To further examine only the dependence of MAOD and AOD_C on wind speed in open ocean conditions, only pixels of MAOD and AOD_C corresponding to open ocean values and sea ice conditions were masked. Slope values and p-values were further calculated. When constructing a histogram to examine whether groups of MAOD and AOD_C values under different wind speed regimes are significantly different in Region A, as all variables violated the Anderson-Darling test of normality, the nonparametric Wilcoxon rank sum test was used to test the null hypothesis that MAOD and AOD_C for the low wind speed group comes from the same continuous distribution with equal medians as MAOD and AOD_C for the high wind speed group (Figure S2.3 & S2.4).

S2 Seasonal & Annual Trends in MAOD, AOD_C, & Wind Speed

In addition to the daily correlations discussed in the main paper, we also investigated longer-term trends in MAOD and AOD_C with wind speed. Across seasonal timescales (Figure S2.7), MAOD and wind speed is positively correlated, indicating that SSA may be a constituent of MAOD observations across seasons. However, these relationships are not significant with the exception of Region B. In contrast, AOD_C and wind speed is anticorrelated on the seasonal timescale across Regions A & B, and with near significance (p-value = 0.085 in Region A, 0.11 in Region B, and 0.18 in Region C) (Figure S2.9). The anticorrelation is also prevalent in trends between AOD_T and wind speed on the seasonal time scale, albeit with lack of significance (Figure S2.7), likely due to the contribution of the AOD_f signal towards AOD_T magnitudes. As the anticorrelation is present with near-significance in AOD_C, this suggests that on the seasonal timescale there may exist a suppression of SSA and a contribution of other environmental factors on AOD_C instead of SSA, as observed for tropical regions (Gabric et al., 2005). However, the limited range of seasonal average wind speeds for this study does not provide sufficient dynamic range for clear evidence of such suppression.

The lack of a significant seasonal correlation of MAOD to wind speed across Regions may be caused by the limited seasonal differences in wind speed, making SSA a relatively invariant constituent of MAOD magnitudes, as found previously for AOD in polar environments (Dror et al., 2018). Specifically mean wind speed is relatively high year-round in the Southern Ocean, dampening seasonal aerosol trends in the wind-driven SSA (Dror et al., 2018). Significant seasonal relationships between the summertime maxima in MAOD and associated sea ice melt and phytoplankton production have indicated that seasonal trends instead reflect the production of biogenic aerosol (Dasarathy et al., 2021). As AOD_C and wind speed is anticorrelated, with p-values of 0.08 and 0.11 in Regions A and B, there may be a biogenic component towards marine aerosol magnitudes in this high-latitude environment.
Across annual timescales (Figure S2.8), MAOD depicts no correlation with wind speed in Regions A and C and a very strong (R=0.9) significant relationship with wind speed in Region B. Similarly, AOD_C is positively correlated with wind speed across Regions A and C, albeit with

a similar lack of significance, and depicts a strong positive correlation (R = 0.52) with near significance (p = 0.08) in Region B. As these trends emerge out of large spatiotemporal averages consisting of a small number of data points (n = 12), we thus predict that, while wind driven-SSA is unlikely to be the only component of magnitudes of MAOD and AOD, SSA is still an important component of overall magnitudes of MAOD and AOD (Figures S8). In the South Pacific gyre, interannual variability in AOD_C was directly correlated with wind speed across 8 years of analysis from 2003 to 2010 (Dror et al., 2018). As such, those authors attributed, at the first order, that wind speed is the main driver of trends in AOD_C and theorize that this link may be prevalent across the oceanic environment. While our observations do not depict the same degree of correlation of MAOD and AOD to wind speed, there nevertheless is a strong wind-driven signature across regions, particularly pronounced in Region B. These annual observations underscore differences in drivers of marine aerosol across ocean regions.

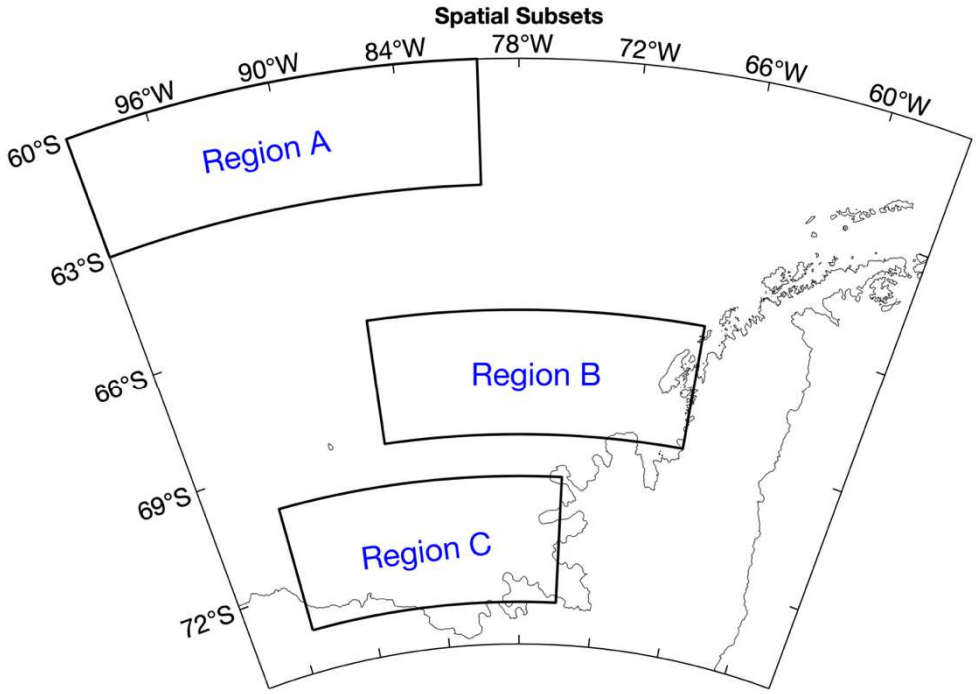

Figure S2.1. Three distinct Regions, specified as Region A, Region B, and Region C, were identified within the Bellingshausen Sea as forming a North-to-South gradient from more wind-driven to more subject to varying light availability, seasonal cycles of blooms of phytoplankton, & the melt and refreeze of sea ice.

Table S2.1. Region A: Daily means (M) & standard deviations (SD) of all variables across all seasons

	Region A							
	Winter		**Spring**		**Summer**		**Fall**	
Variables	*M*	*SD*	*M*	*SD*	*M*	*SD*	*M*	*SD*
Chl-*a* (mg m^{-3})	NaN	NaN	0.1739	0.0961	0.1820	0.1312	0.0995	0.0238
Sea Ice (δ)	0.0416	0.0626	0.0542	0.0920	0.0493	0.0953	0.0395	0.0654
Day Winds (m s^{-1})	10.5156	3.6730	10.7779	3.4941	8.7982	3.1159	9.8909	3.6090
Night Winds (m s^{-1})	10.5640	3.8241	10.6625	3.6169	8.9854	3.3501	10.0913	3.4974
SST	1.6063	1.0723	1.7607	1.0494	3.6259	1.4832	3.0470	1.4563
AOD_C	0.0553	0.0384	0.0947	0.0593	0.1017	0.0726	0.0681	0.0509
AOD_T	0.0578	0.0172	0.1030	0.0245	0.1145	0.0276	0.0740	0.0214
AOD_f	0.0034	0.1221	0.0114	0.2256	0.0179	0.3218	0.0112	0.3189
MAOD	0.0962	0.0878	0.1023	0.0964	0.0889	0.0741	0.0984	0.0818

Note: NaNs are omitted in calculation of M & SD

Table S2.2. Region B: Daily means (M) & standard deviations (SD) of all variables across all seasons

	Region B							
	Winter		**Spring**		**Summer**		**Fall**	
Variables	*M*	*SD*	*M*	*SD*	*M*	*SD*	*M*	*SD*
Chl-*a* (mg m^{-3})	NaN	NaN	0.4343	1.1698	0.6919	1.7075	0.7130	1.5529
Sea Ice (δ)	0.6365	0.2275	0.6145	0.2632	0.2145	0.2566	0.1326	0.1715
Day Winds (m s^{-1})	8.1496	3.7358	8.0387	3.4568	6.3491	2.5104	7.9706	3.3985
Night Winds (m s^{-1})	8.0989	3.5311	7.7185	3.7411	6.4648	3.0237	8.0750	3.4955
SST (°C)	0.5609	0.1586	-1.2509	0.4744	0.3754	1.0883	0.3616	0.9095
AOD_C	0.0534	0.0466	0.0836	0.0563	0.0745	0.0611	0.0512	0.0464
AOD_T	0.0548	0.0148	0.0960	0.0271	0.0869	0.0263	0.0591	0.0199
AOD_f	0.0014	0.0074	0.0236	0.4223	0.0256	0.5293	0.0188	0.4889
MAOD	0.0694	0.0520	0.0853	0.0559	0.0614	0.0596	0.0820	0.0887

Note: NaNs are omitted in calculation of M & SD

Table S2.3. Region C: Daily means (M) & standard deviations (SD) of all variables across all seasons

	Region C							
	Winter		**Spring**		**Summer**		**Fall**	
Variables	*M*	*SD*	*M*	*SD*	*M*	*SD*	*M*	*SD*
Chl-*a* (mg m^{-3})	NaN	NaN	0.1372	0.1234	2.3523	3.8708	1.7546	2.7409
Sea Ice (δ)	0.7818	0.0606	0.7963	0.0926	0.5499	0.2780	0.5555	0.2498
Day Winds (m s^{-1})	7.3321	3.7482	7.4036	3.5445	5.8426	2.5825	7.4008	3.4510
Night Winds (m s^{-1})	7.3395	3.2526	7.1714	3.7502	6.6281	3.1906	7.5450	3.3405
SST (°C)	NaN	NaN	-0.8580	0.6665	0.0932	1.0256	-0.6956	0.6511
AOD_C	0.0494	0.0322	0.0886	0.0546	0.0902	0.0629	0.0647	0.0504
AOD_T	0.0515	0.0168	0.0999	0.0252	0.1022	0.0273	0.0739	0.0208
AOD_f	0.0023	0.0491	0.0206	0.4236	0.0210	0.4391	0.0227	0.5158
MAOD	NaN	NaN	NaN	NaN	0.0543	0.0495	0.0451	0.0683

Note: NaNs are omitted in calculation of M & SD

Table S2.4. Summarizing correlation and significance of daily trends and seasonal comparisons (Figures 3, 4, S2.5, & S2.6)

	Region A		**Region B**		**Region C**	
Variables	*Daily*	*Seasonal Comparison*	*Daily*	*Seasonal Comparison*	*Daily*	*Seasonal Comparison*
MAOD	**weak; significant**	no seasonal differences: **Winter is weak; significant** **Summer is weak; significant**	**weak; significant**	some seasonal differences: Winter is weak; not significant **Summer is weak; significant**	very weak; not significant	seasonal not available

AOD_C	**very weak; significant**	some seasonal differences: Winter is very weak; not significant **Summer is very weak; significant**	**very weak; significant**	some seasonal differences: **Springtime is weak; significant.** **Fall is weak significant.** **Summertime is very weak, significant.**	**very weak; significant**	seasonal not available
AOD_T	very weak; not significant	Some seasonal differences: Winter is very weak; not significant **Summer is very weak; significant**	**very weak; significant**	some seasonal differences: **Spring is weak; significant** **Fall is weak significant.** **Summer is very weak, significant**	very weak; not significant	seasonal not available
AOD_f	very weak; not significant	no seasonal differences: Winter is very weak; not significant Summer is very weak; not significant	**very weak; significant**	some seasonal differences: Spring is very weak; not significant**.** **Fall is very weak significant.** Summer is very weak, not significant	very weak; not significant	seasonal not available

Note: for absolute values of R, 0-0.19 is regarded as very weak and 0.2-0.39 as weak (Correlation and Regression: The BMJ., 2020). $p < 0.05$ is used to define significance.

Table S2.5. Summarizing correlation and significance from Figures S2.7 (seasonal trends in MAOD and AOD) and Figure S2.8 (annual trends in MAOD and AOD)

	Region A		**Region B**		**Region C**	
Variables	*Seasonal*	*Annual*	*Seasonal*	*Annual*	*Seasonal*	*Annual*
MAOD	very weak; not significant	weak; not significant	**weak; significant**	**very strong; significant**	very weak; not significant	weak; not significant
AOD_C	weak; near significance (p = 0.08)	weak; not significant	weak; not significant	moderate; near significance (p = 0.08)	weak; not significant	weak; not significant
AOD_T	very weak; not significant	moderate; near significance (p = 0.08)	very weak; not significant	very weak; not significant	very weak; not significant	very weak; not significant
AOD_f	weak; not significant	weak; not significant	weak; not significant	weak; not significant	weak; not significant	very weak; not significant

Note: for absolute values of R, 0-0.19 is regarded as very weak, 0.2-0.39 as weak, 0.40-0.59 as moderate, 0.6-0.79 as strong, and 0.8-1 as very strong (Correlation and Regression: The BMJ., 2020). $p < 0.05$ is used to define significance.

Table S2.6. Summarizing correlation and significance from Figure S2.10 (daily trends in MAOD and AOD_C versus chlorophyll-*a* concentration) and Figure S2.11 (daily trends in MAOD and AOD_C versus sea surface temperature)

	Region A		**Region B**		**Region C**	
Variables	Chl-*a*	*SST*	Chl-*a*	*SST*	Chl-*a*	*SST*
MAOD	very weak, not significant	very weak; not significant	**weak; significant**	very weak; not significant	very weak; not significant	NaN
AOD_C	**very weak; significant**	**weak; significant**	very weak; not significant	very weak; not significant	very weak; not significant	moderate; not significant

Note: for absolute values of R, 0-0.19 is regarded as very weak, 0.2-0.39 as weak, 0.40-0.59 as moderate, 0.6-0.79 as strong, and 0.8-1 as very strong (Correlation and Regression: The BMJ., 2020). $p < 0.05$ is used to define significance.

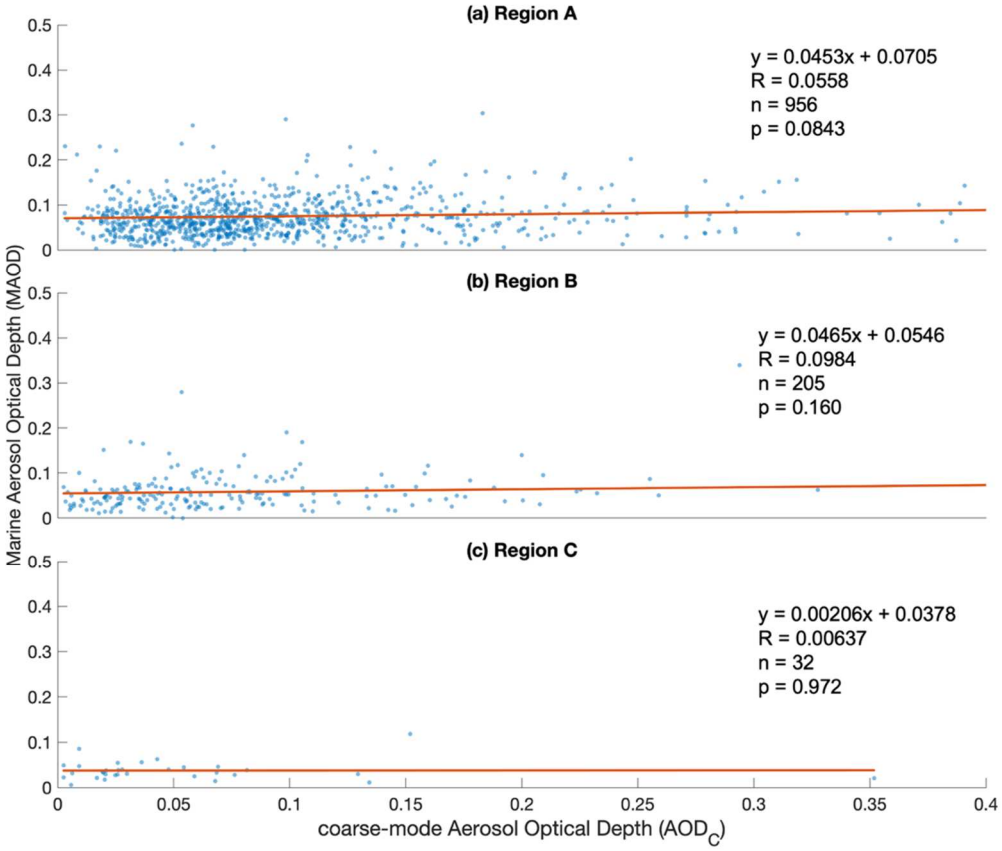

Figure S2.2.A, S2.2.B, & S2.2.C. Daily observations of Marine Aerosol Optical Depth (MAOD) vs. coarse-mode Aerosol Optical Depth (AOD_C) across all Regions.

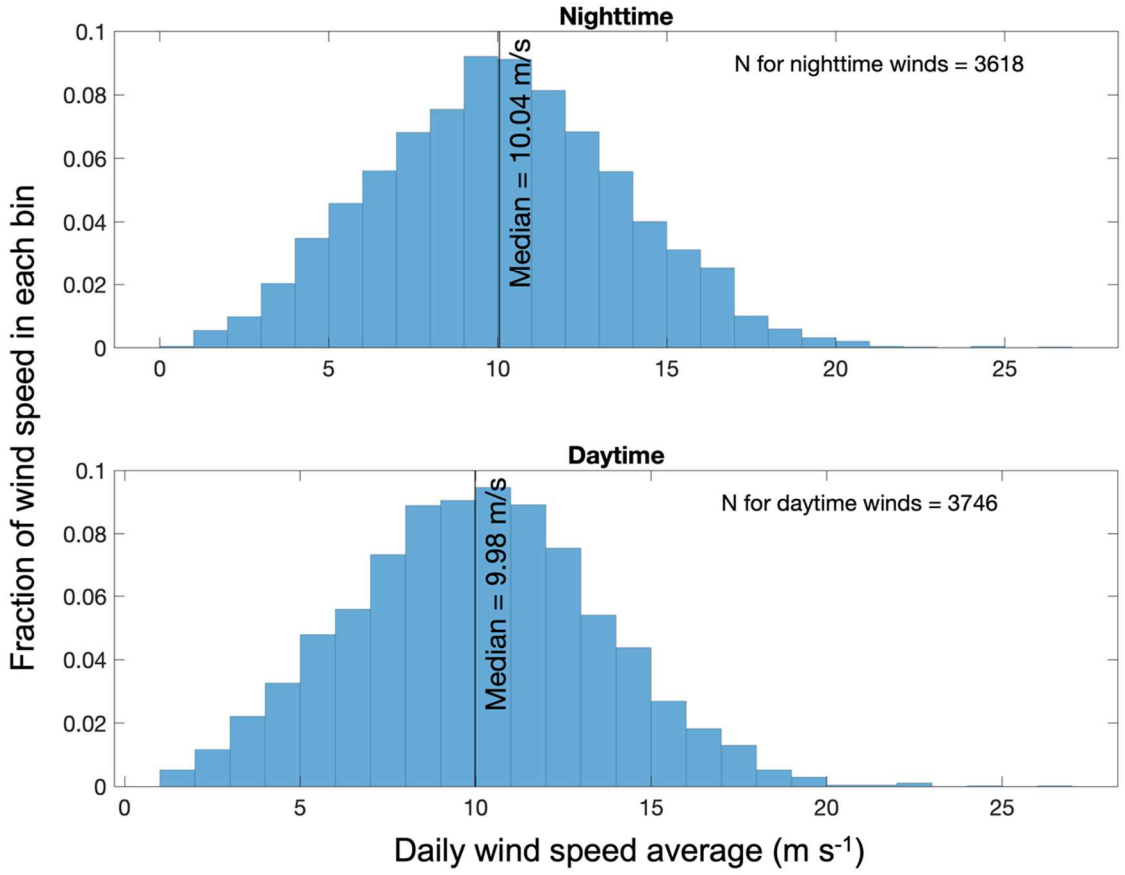

Figure S2.3. Daily wind distribution in Region A. Median Wind Speed is used to signify the cut off for high wind speed vs low wind speed conditions in Figure S4.

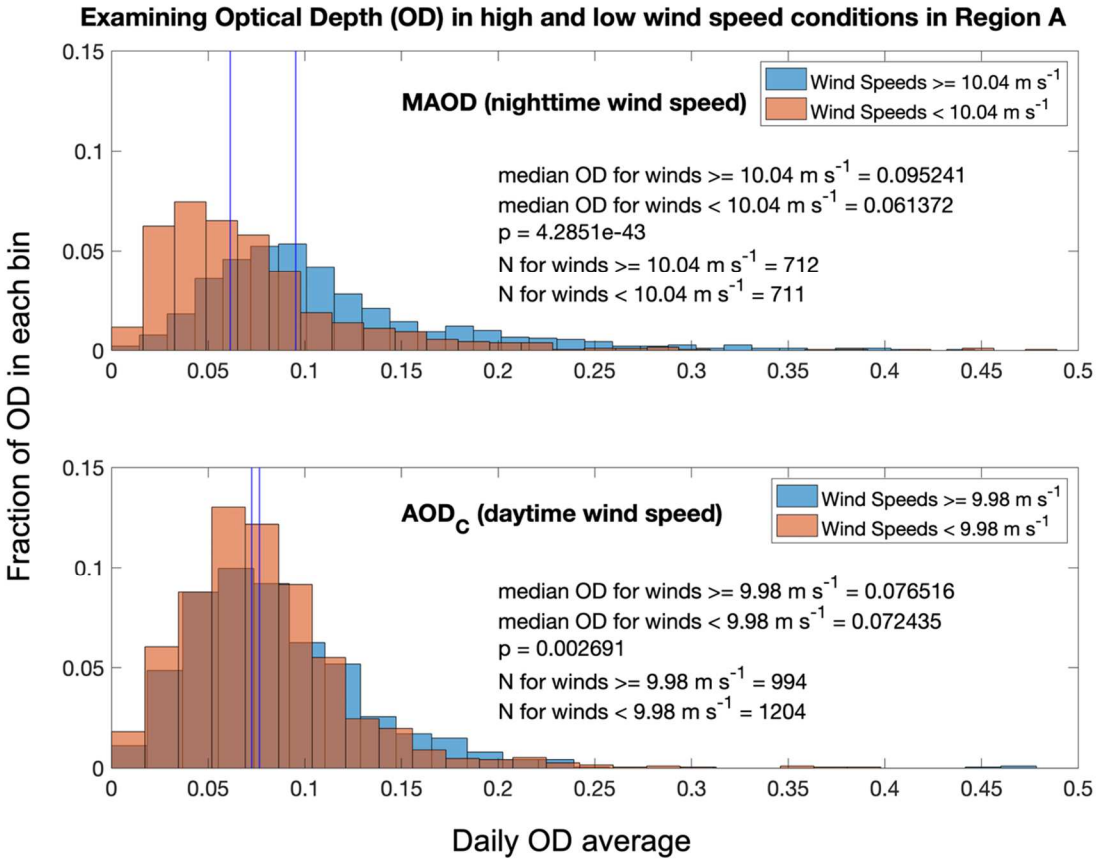

Figure S2.4. Examining optical depth (OD) in high wind speed versus low wind speed conditions. Wind speed cut off ascertained from the median wind speed in Region A (10.04 m s^{-1} for nighttime winds, 9.98 m s^{-1} for daytime winds) (Figure S3). Blue lines signify the median OD for both high and low wind speed conditions. Wind speed has a significant impact on increasing OD, indicating that SSA is a likely constituent of OD driven by wind action over the surface ocean. This is observed across all seasons, and the effect of wind speed driving sea spray aerosol presence is present across the entire year during high wind speed conditions in Region A. Significant differences between wind speed groups occur across both MAOD and AOD_C with median values differing by 0.034 and 0.005 MAOD and AOD_C, respectively.

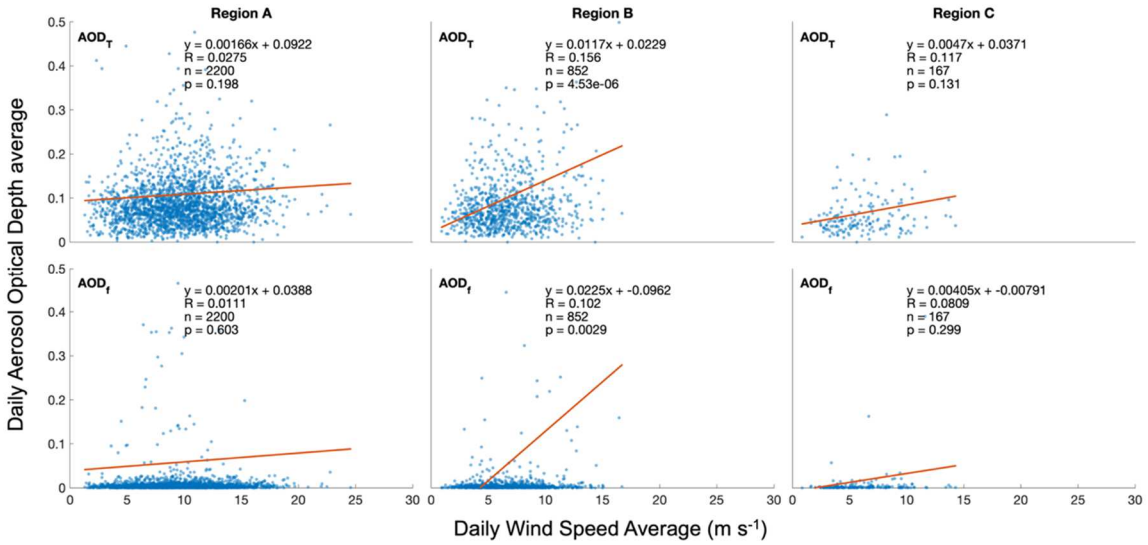

Figure S2.5.A, S2.5.B, S2.5.C. Scatterplots of daily averages of total AOD (AOD_T) and fine-mode AOD (AOD_f) vs daily averages of daytime wind speed across all regions in open ocean (no sea ice) conditions.

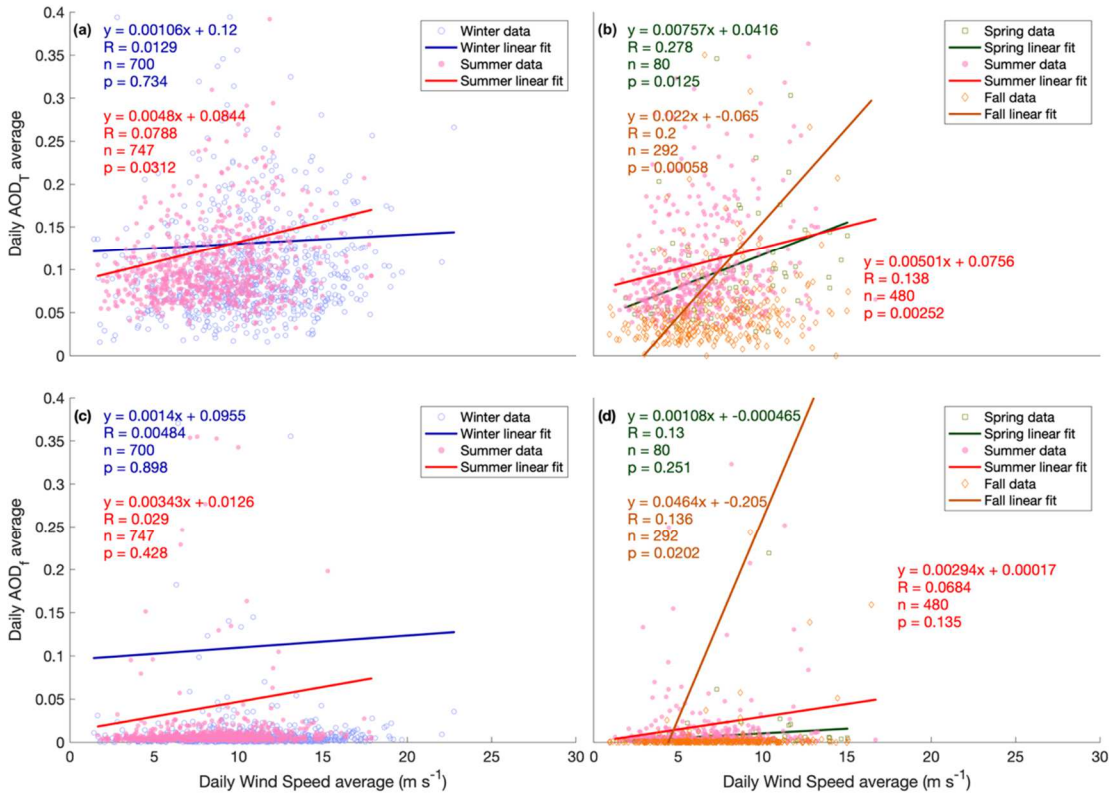

Figure S2.6.a & 2.6.b. Seasonal scatterplots of daily averages of total Aerosol Optical Depth (AOD_T) vs. daily averages of daytime wind speed in Regions A & B. **Figures S2.6.c & S2.6.d.** Seasonal scatterplots of daily averages of fine-mode Aerosol Optical Depth (AOD_f) vs. daily averages of daytime wind speed in Regions A & B (See Figure S2.1). Region C is not included due to insufficient data across seasons. In **Figures 2.6.b & 2.6.d**, spring and fall are compared to summer due to lack of wintertime data in Region B. Southern hemisphere seasons are defined as winter: June 1–September 1, spring: September 1–December 1, summer: December 1–March 1, fall: March 1–June 1. d

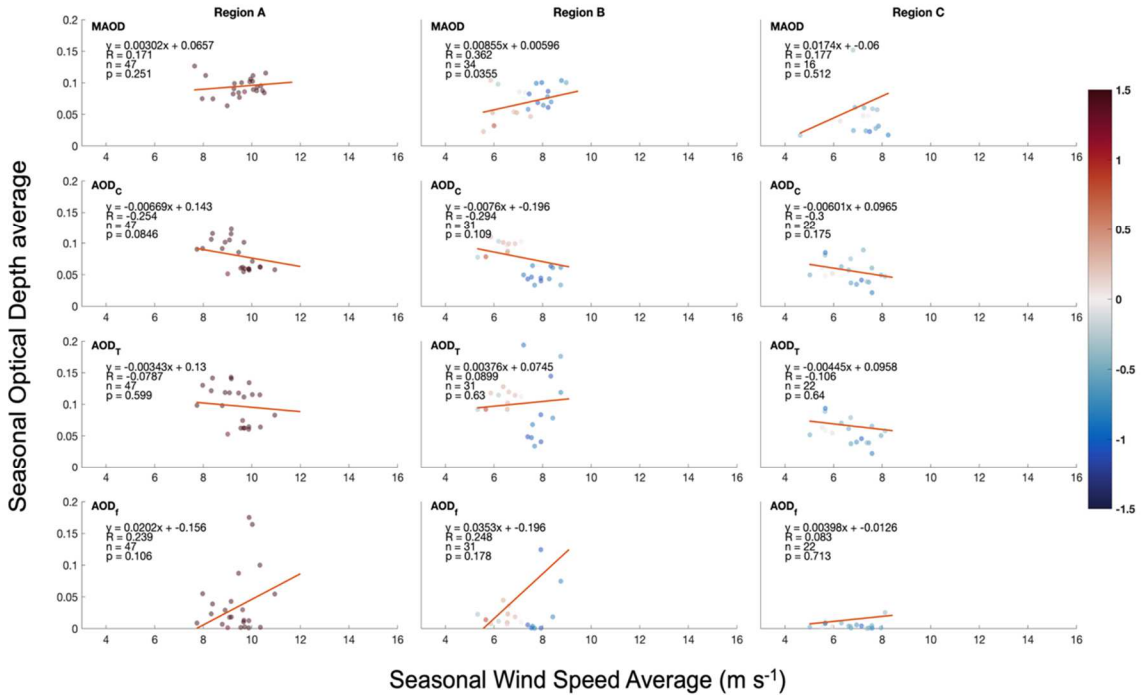

Figure S2.7.A, S2.7.B, & S2.7.C. Seasonal scatterplot assessing Marine Aerosol Optical Depth (MAOD), coarse-mode Aerosol Optical Depth (AOD_C), total Aerosol Optical Depth (AOD_T), and fine-mode Aerosol Optical Depth (AOD_f) vs. nighttime (for MAOD) and daytime (for AOD) Wind Speed across all Regions in open ocean (no sea ice) conditions.

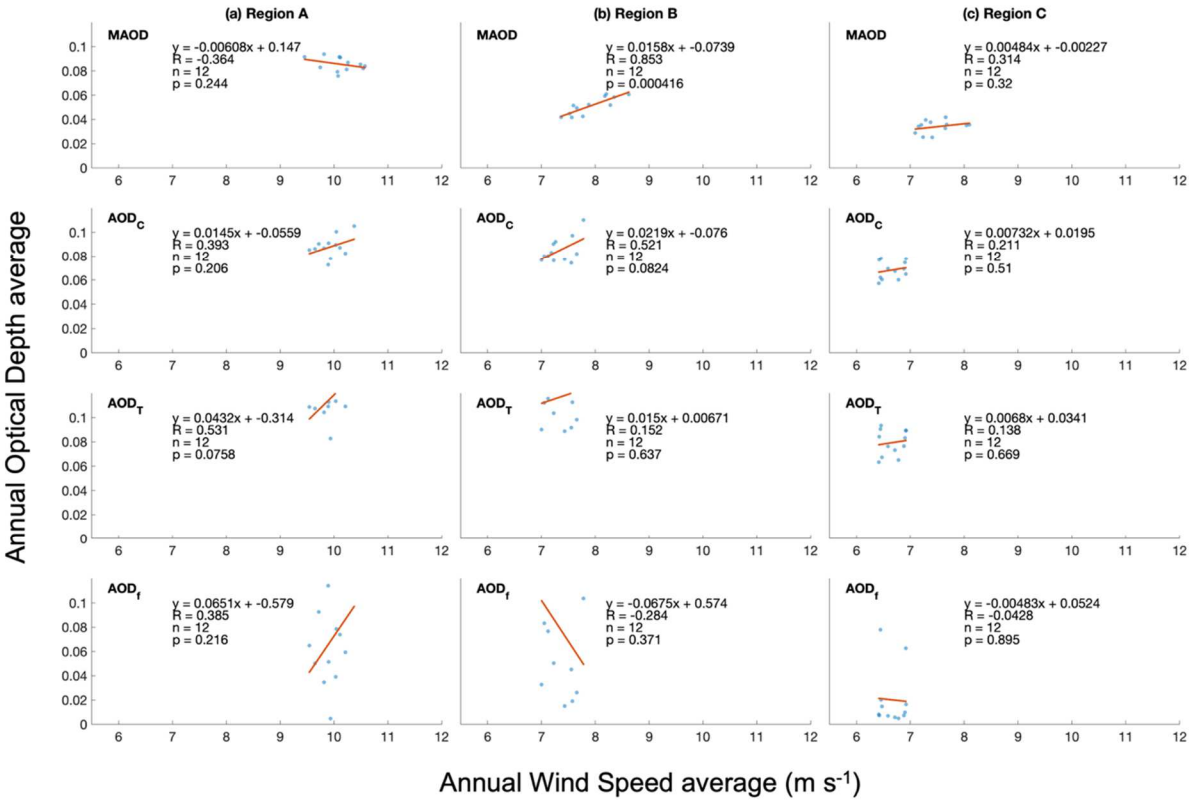

Figure S2.8.A, S2.8.B, & S2.8.C. Annual scatterplot assessing Marine Aerosol Optical Depth (MAOD), coarse-mode Aerosol Optical Depth (AOD_C), total Aerosol Optical Depth (AOD_T), and fine-mode Aerosol Optical Depth (AOD_f) vs. nighttime (for MAOD) and daytime (for AOD) Wind Speed across all Regions in open ocean (no sea ice) conditions.

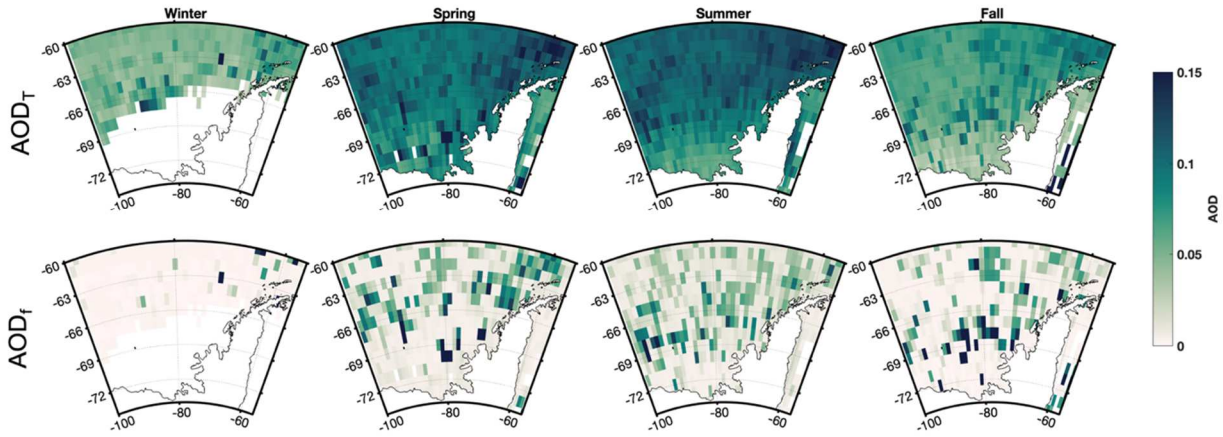

Figure S2.9. Seasonal climatologies of total Aerosol Optical Depth (AOD_T) and the fine-mode fraction of AOD (AOD_f). These data were obtained from January 2007 to December 2018 across the spatial grid between 100°W–54°W and 60°S–75°S. Missing data is present in winter due to solar nighttime conditions. Southern hemisphere seasons are defined as winter: June 1–September 1, spring: September 1–December 1, summer: December 1–March 1, fall: March 1–June 1.

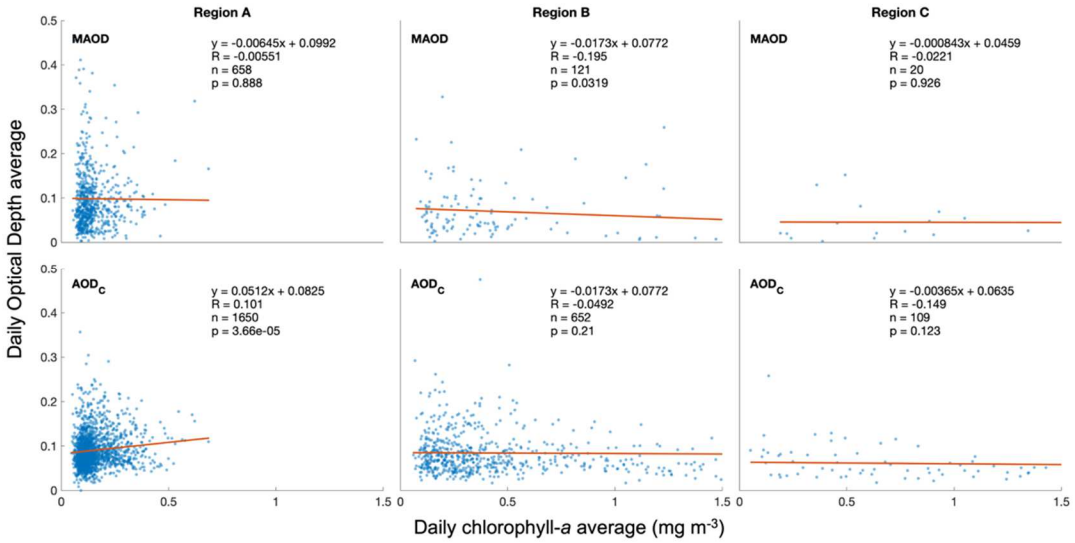

Figure S2.10.A, S2.10.B, & S2.10.C. Scatterplot assessing daily averages of Marine Aerosol Optical Depth (MAOD) and coarse-mode Aerosol Optical Depth (AOD_C) vs. daily averages of chlorophyll-*a* across all Regions in open ocean (no sea ice) conditions.

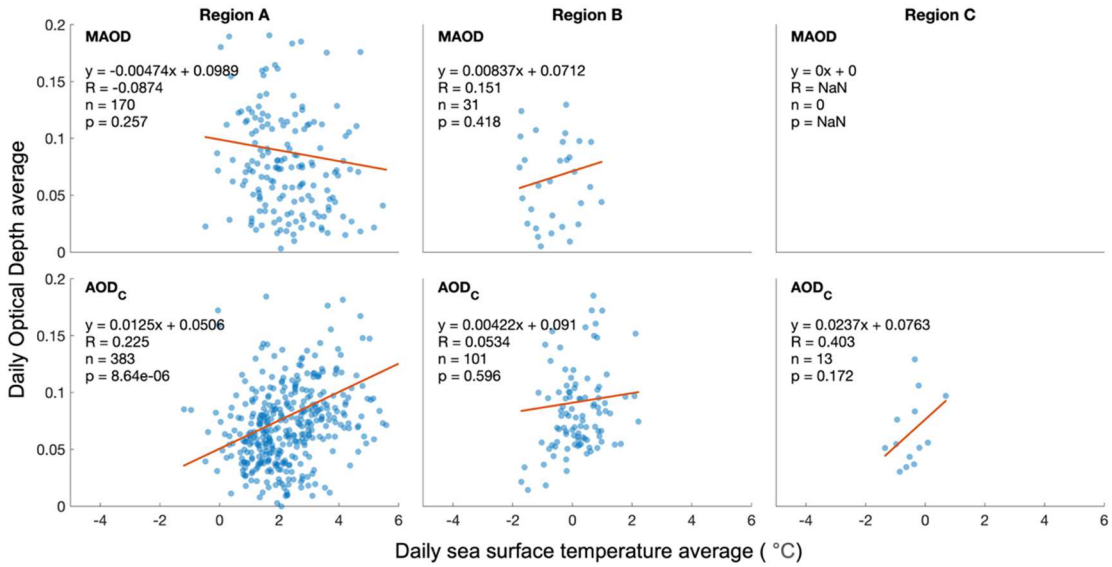

Figure S2.11.A, S2.11.B, & S2.11.C. Scatterplot assessing daily averages of Marine Aerosol Optical Depth (MAOD) and coarse-mode Aerosol Optical Depth (AOD_C) vs. daily averages of sea surface temperature (SST) across all Regions in open ocean (no sea ice) conditions.

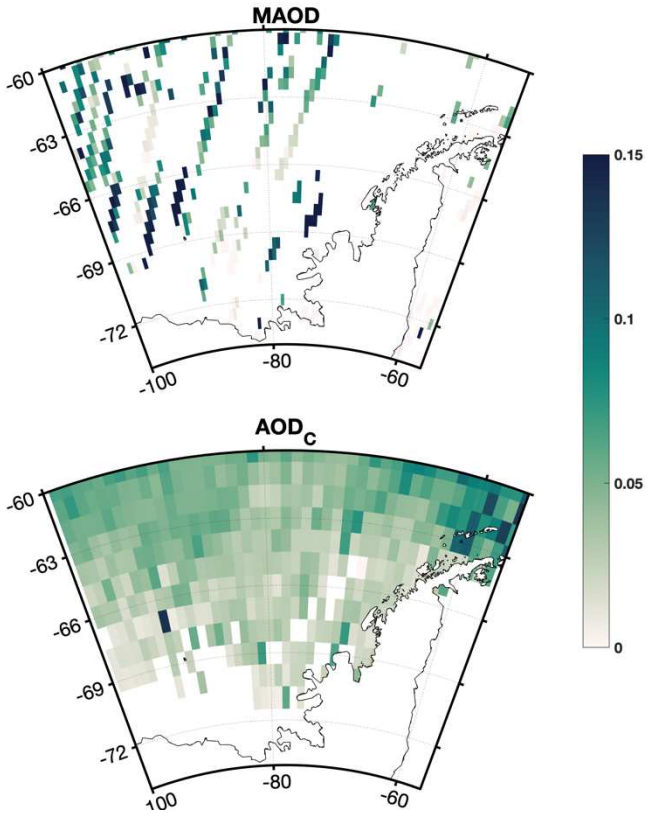

Figure S2.12. Spatial plot representing an average of 1 month of data (April 2012). Marine Aerosol Optical Depth (MAOD) is averaged across the month of April 2012 and mapped at a spatial resolution of 0.5 ° latitude x 0.5 ° longitude thereby visualizing the swaths of CALIPSO as the satellite transects the Bellingshausen Sea. Coarse-mode Aerosol Optical Depth (AOD_C) is visualized at the Level 3 mapped spatial resolution of 1 ° latitude x 1 ° longitude.

Chapter 3 Supporting Information

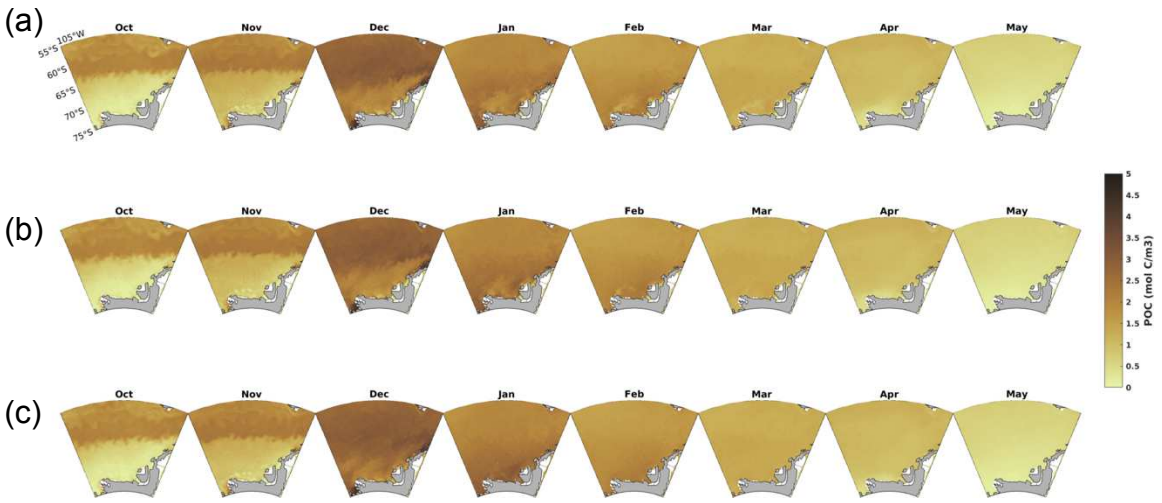

Figures S3.1. Spatial distribution of particulate organic carbon (POC) across October 2013 to May 2014 in the Bellingshausen Sea. Pixels represent the integral from the surface ocean to a depth of 80 meters. **Row a** represents the perturbation of increase in sea ice albedo to the Biogeochemical Southern Ocean State Estimate. **Row b** represents the control scenario without perturbation to sea ice albedo. **Row c** represents the perturbation of decrease in sea ice albedo.

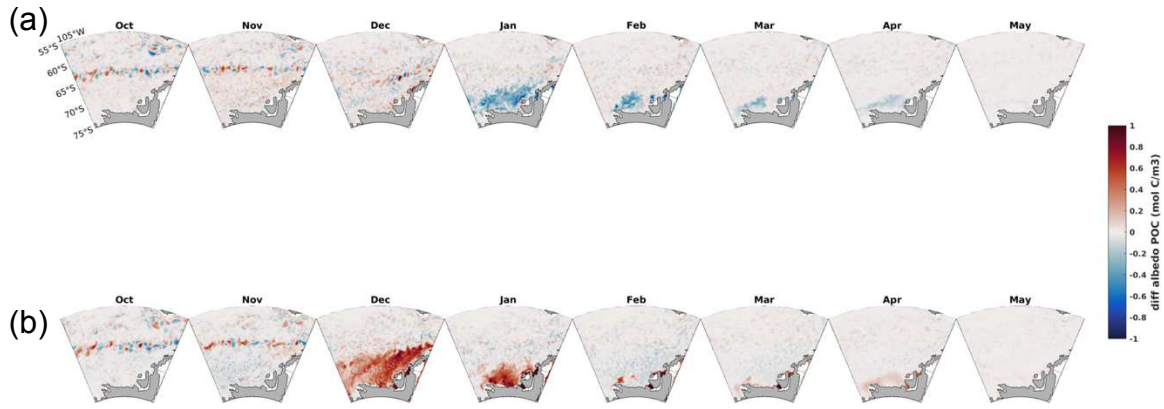

Figures S3.2. Particulate organic carbon (POC) spatial difference plots across October 2013 to May 2014 in the Bellingshausen Sea. **Row a** represents the high albedo perturbation minus the control albedo perturbation. **Row b** represents the low albedo perturbation minus the control albedo perturbation.

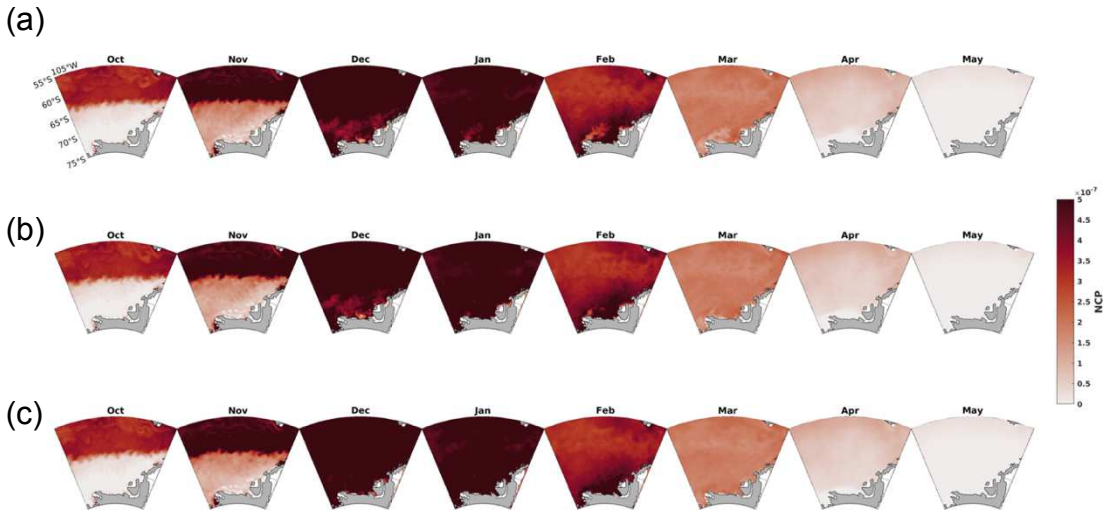

Figures S3.3. Spatial distribution of net community production (NCP) across October 2013 to May 2014 in the Bellingshausen Sea. Pixels represent the integral from the surface ocean to a depth of 80 meters. **Row a** represents the perturbation of increase in sea ice albedo to the Biogeochemical Southern Ocean State Estimate. **Row b** represents the control scenario without perturbation to sea ice albedo. **Row c** represents the perturbation of decrease in sea ice albedo.

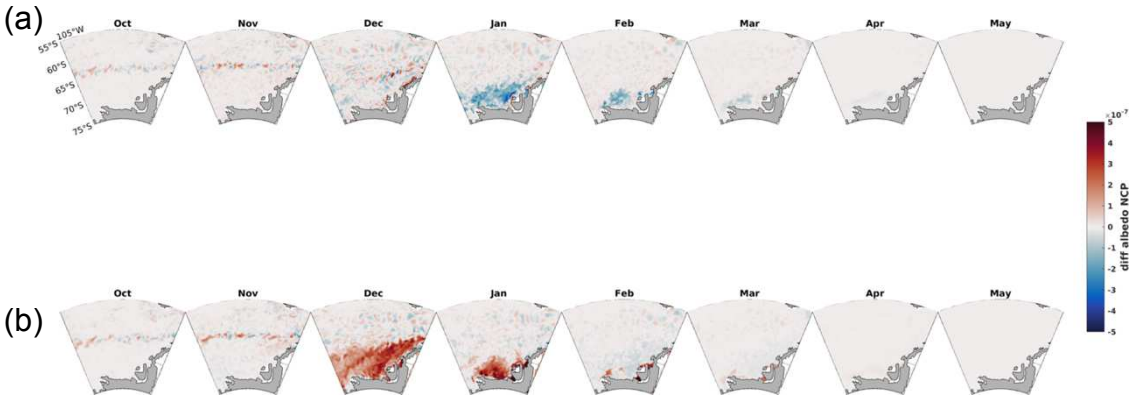

Figures S3.4. Net community production (NCP) spatial difference plots across October 2013 to May 2014 in the Bellingshausen Sea. **Row a** represents the high albedo perturbation minus the control albedo perturbation. **Row b** represents the low albedo perturbation minus the control albedo perturbation.

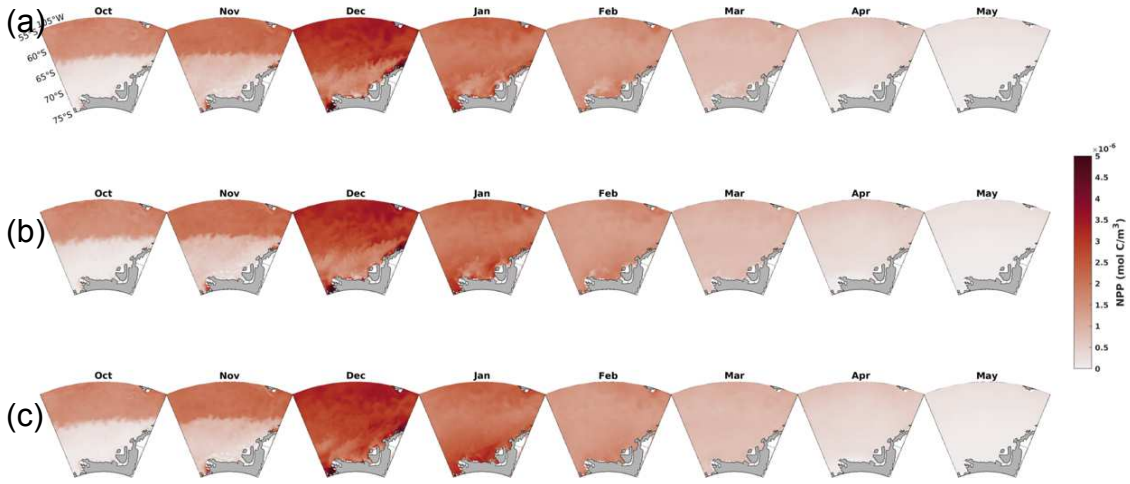

Figures S3.5. Spatial distribution of net primary production across October 2013 to May 2014 in the Bellingshausen Sea. Pixels represent the integral from the surface ocean to a depth of 80 meters. **Row a** represents the perturbation of increase in sea ice albedo to the Biogeochemical Southern Ocean State Estimate. **Row b** represents the control scenario without perturbation to sea ice albedo. **Row c** represents the perturbation of decrease in sea ice albedo.

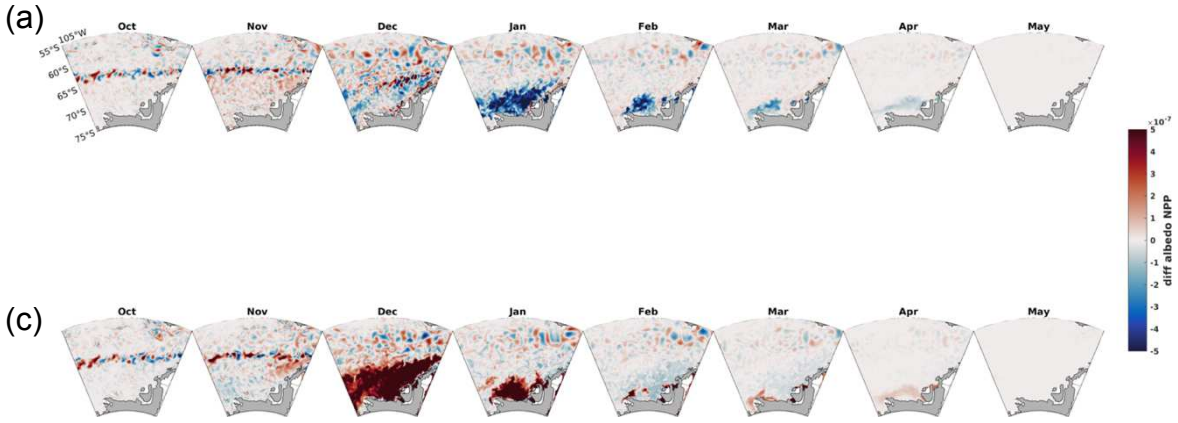

Figures S3.6. Net primary production (NPP) spatial difference plots across October 2013 to May 2014 in the Bellingshausen Sea. **Row a** represents the high albedo perturbation minus the control albedo perturbation. **Row b** represents the low albedo perturbation minus the control albedo perturbation.

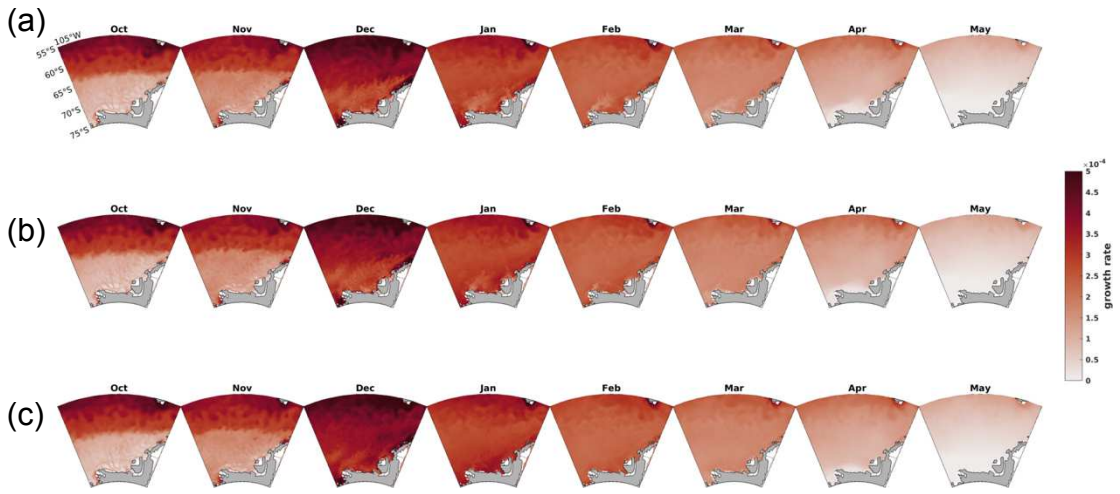

Figures S3.7. Spatial distribution of phytoplankton growth rate across October 2013 to May 2014 in the Bellingshausen Sea. Pixels represent the integral from the surface ocean to a depth of 80 meters. **Row a** represents the perturbation of increase in sea ice albedo to the Biogeochemical Southern Ocean State Estimate. **Row b** represents the control scenario without perturbation to sea ice albedo. **Row c** represents the perturbation of decrease in sea ice albedo.

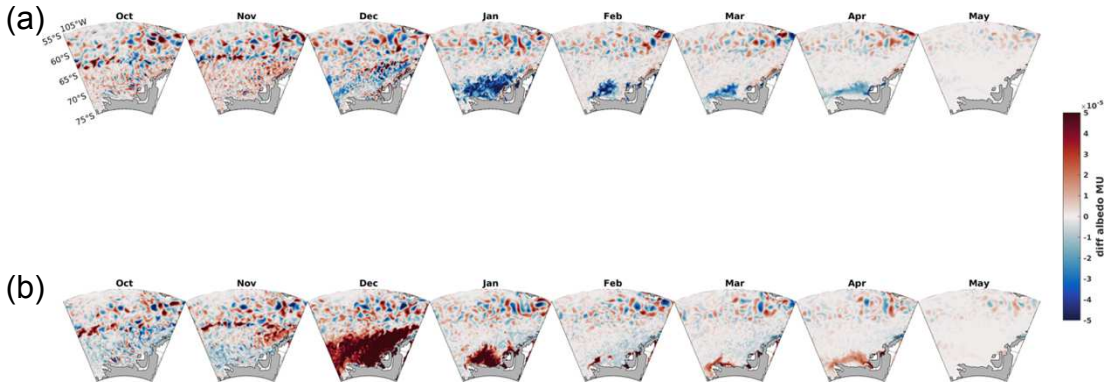

Figures S3.8. Phytoplankton growth rate difference plots across October 2013 to May 2014 in the Bellingshausen Sea. **Row a** represents the high albedo perturbation minus the control albedo perturbation. **Row b** represents the low albedo perturbation minus the control albedo perturbation.

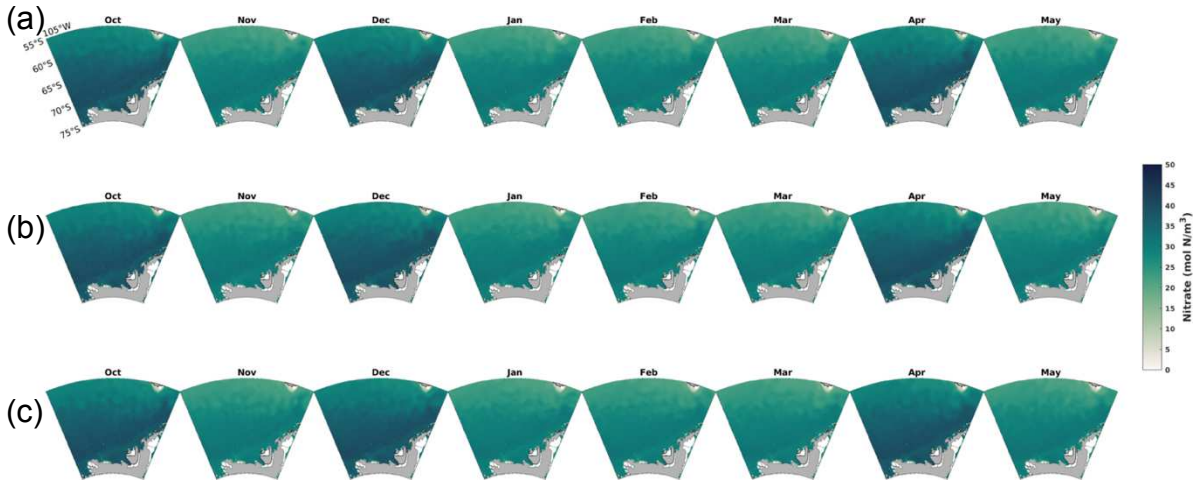

Figures S3.9. Spatial distribution of nitrate concentration across October 2013 to May 2014 in the Bellingshausen Sea. Pixels represent the integral from the surface ocean to a depth of 250 meters. **Row a** represents the perturbation of increase in sea ice albedo to the Biogeochemical Southern Ocean State Estimate. **Row b** represents the control scenario without perturbation to sea ice albedo. **Row c** represents the perturbation of decrease in sea ice albedo.

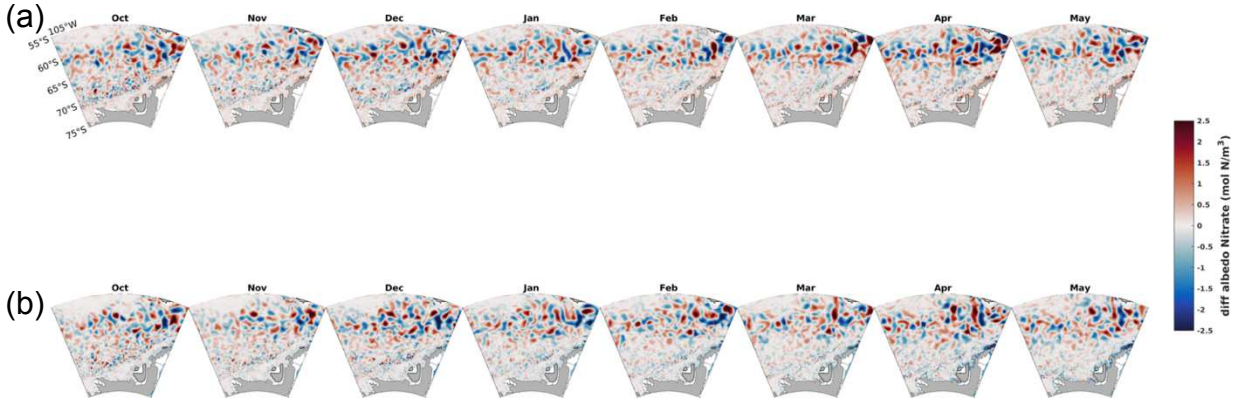

Figures S3.10. Nitrate concentration difference plots across October 2013 to May 2014 in the Bellingshausen Sea. **Row a** represents the high albedo perturbation minus the control albedo perturbation. **Row b** represents the low albedo perturbation minus the control albedo perturbation.

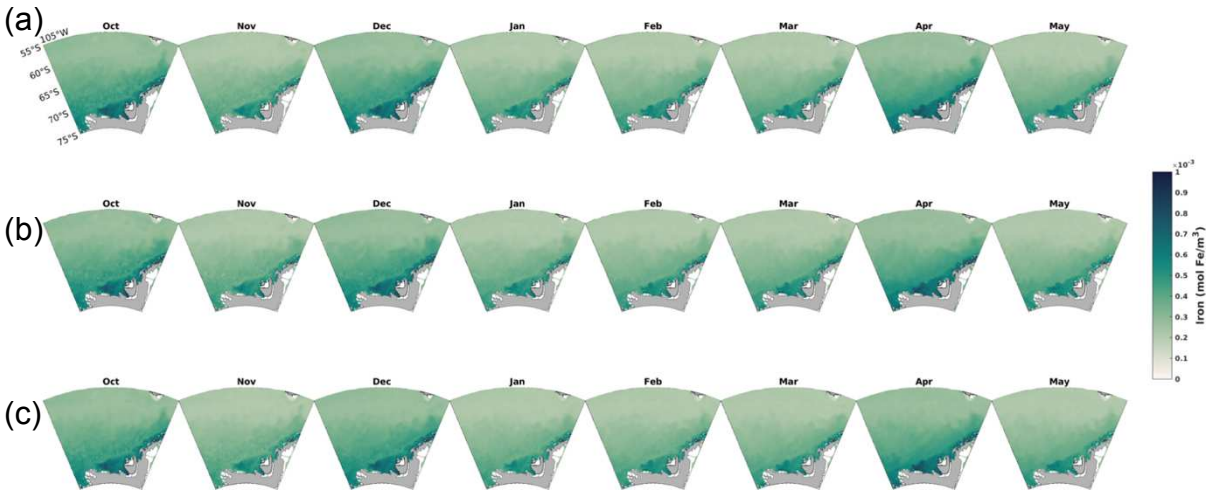

Figures S3.11. Spatial distribution of iron concentration across October 2013 to May 2014 in the Bellingshausen Sea. Pixels represent the integral from the surface ocean to a depth of 250 meters. **Row a** represents the perturbation of increase in sea ice albedo to the Biogeochemical Southern Ocean State Estimate. **Row b** represents the control scenario without perturbation to sea ice albedo. **Row c** represents the perturbation of decrease in sea ice albedo.

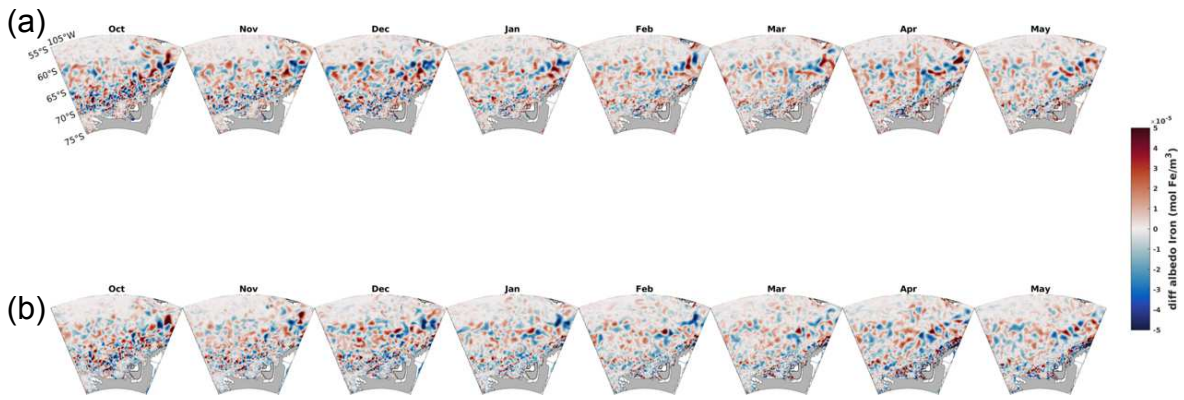

Figures S3.12. Iron concentration difference plots across October 2013 to May 2014 in the Bellingshausen Sea. **Row a** represents the high albedo perturbation minus the control albedo perturbation. **Row b** represents the low albedo perturbation minus the control albedo perturbation.